UNITED STATES DEPARTMENT OF ENERGY (DOE)
Announcement of Scientific and Technical Information (STI)
(For Use By Financial Assistance Recipients and Non-M&O/M&I Contractors)

OMB CONTROL NO.
1910-1400

PART I: STI PRODUCT DESCRIPTION
(To be completed by Recipient/Contractor)

A. STI Product Identifiers

1. REPORT/PRODUCT NUMBER(s)
None

2. DOE AWARD/CONTRACT NUMBER(s)
DE-FG36-07GO17041

3. OTHER IDENTIFYING NUMBER(s)
None

B. Recipient/Contractor

Purdue University – Calumet, Dept. of Mechnaical Engineering, Hammond, IN 46321

C. STI Product Title

Minimization of Blast Furnace Fuel Rate by Optimizing Burden and Gas Distribution

D. Author(s)

Dr. Chenn Zhou

E-mail Address(es):
czhou@purduecal.edu

E. STI Product Issue Date/Date of Publication

08 15 2012
MM DD YYYY

F. STI Product Type (*Select only one*)

☒ 1. TECHNICAL REPORT
☒ *Final* ☐ *Other (specify)* _____

☐ 2. CONFERENCE PAPER/PROCEEDINGS

Conference Information (title, location, dates)

☐ 3. JOURNAL ARTICLE
a. TYPE: ☐ *Announcement Citation Only* ☐ *Preprint* ☐ *Postprint*
b. JOURNAL NAME
c. VOLUME _____ *d. ISSUE* _____
e. SERIAL IDENTIFIER (e.g. ISSN or CODEN)

☐ 4. OTHER, SPECIFY

G. STI Product Reporting Period

08 15 2007 Thru 06 30 2012
MM DD YYYY MM DD YYYY

H. Sponsoring DOE Program Office

Office of Industrial Technologies (OIT)(EE20)

I. Subject Categories *(list primary one first)*

32 Energy Conservation, Consumption and Utilization

Keywords: Fuel Rate, Burden Distribution, Blast Furnace, CFD

J. Description/Abstract

The goal of the research is to improve the competitive edge of steel mills by using the advanced CFD technology to optimize the gas and burden distributions inside a blast furnace for achieving the best gas utilization. A state-of-the-art 3-D CFD model has been developed for simulating the gas distribution inside a blast furnace at given burden conditions, burden distribution and blast parameters. The comprehensive 3-D CFD model has been validated by plant measurement data from an actual blast furnace. Validation of the sub-models is also achieved. The user friendly software package named Blast Furnace Shaft Simulator (BFSS) has been developed to simulate the blast furnace shaft process. The research has significant benefits to the steel industry with high productivity, low energy consumption, and improved environment.

K. Intellectual Property/Distribution Limitations

(must select at least one; if uncertain contact your Contracting Officer (CO))

☒ 1. UNLIMITED ANNOUNCEMENT *(available to U.S. and non-U.S. public; the Government assumes no liability for disclosure of such data)*

☐ 2. COPYRIGHTED MATERIAL: *Are there any restrictions based on copyright?* ☐ *Yes* ☐ *No.*
If yes, list the restrictions as contained in your award document

☐ 3. PATENTABLE MATERIAL: THERE IS PATENTABLE MATERIAL IN THE DOCUMENT.
INENTION DISCLOSURE SUBMITTED TO DOE:
DOE Docket Number: S-
(Sections are marked as restricted distribution pursuant to 35 USC 205)

☐ 4. PROTECTED DATA: ☐ CRADA ☐ *Other, specify*
Release date (required) no more than 5 years from date listed in Part I.E. above MM DD YYYY

☐ 5. SMALL BUSINESS INNOVATION RESEARCH (SBIR) DATA
Release date (required) no more than 4 years from date listed in Part I.E. above MM DD YYYY

☐ 6. SMALL BUSINESS TECHNOLOGY TRANSFER RESEARCH (STTR) DATA
Release date (required) no more than 4 years from date listed in Part I.E. above MM DD YYYY

☐ 7. OFFICE OF NUCLEAR ENERGY APPLICED TECHNOLOGY

L. Recipient/Contract Point of Contact *Contact for additional information (contact or organization name To be included in published citations and who would Receive any external questions about the content of the STI Product or the research contained herein)*

Dr. Chenn Zhou
Name and/or Position
gzhou@calumet.purdue.edu (219)989-2665
E-mail *Phone*
Dept. of Mechanical Engineering, Purdue University - Calumet, Hammond, IN 46321

UNITED STATES DEPARTMENT OF ENERGY (DOE)
Announcement of Scientific and Technical Information (STI)
(For Use By Financial Assistance Recipients and Non-M&O/M&I Contractors)

OMB CONTROL NO.
1910-1400

PART II: STI PRODUCT MEDIA/FORMAT and LOCATION/TRANSMISSION

(To be completed by Recipient/Contractor)

A. Media/Format Information:

1. MEDIUM OF STI PRODUCT IS:
   ☒ Electronic Document ☐ Computer Medium
   ☐ Audiovisual Material ☐ Paper ☐ No Full-text
2. SIZE OF STI PRODUCT 8,728 KB
3. SPECIFY FILE FORMAT OF ELECTRONIC DOCUMENT BEING TRANSMITTED, INDICATE:
   ☐ SGML ☐ HTML ☐ XML ☒ PDF Normal
   ☐ PDF Image ☐ TIFFG4
   ☐ WP-indicate Version (*5.0 or greater)* _____
   Platform/operation system _____
   ☐ MS-indicate Version (*5.0 or greater)* _____
   Platform/operation system _____
   ☐ Postscript _____
4. IF COMPUTER MEDIUM OR AUDIOVISUAL MATERIAL:
   a. Quantity/type (*specify)* _____
   b. Machine compatibility (*specify)* _____
   c. Other information about product format a user needs to know:
   _____

B. Transmission Information:

1. STI PRODUCT IS BEING TRANSMITTED:
   ☒ a. Electronically via E-Link
   b. Via mail or shipment to address indicated in award document (*Paper product, CD-ROM, diskettes, video cassettes, etc.)*
   _____
2. INFORMATION PRODUCT FILE NAME
   ☒ *(of transmitted electronic format)*
   GO17041NonPropFinalReport

PART III: STI PRODUCT REVIEW/RELEASE INFORMATION

(To be completed by DOE)

A. STI Product Reporting Requirements Review.

☐ 1. THIS DELIVERABLE COMPLETES ALL REQUIRED DELIVERABLES FOR THIS AWARD
☐ 2. THIS DELIVERABLE FULFILLS A TECHNICAL INFORMATION REPORTING REQUIREMENT, BUT SHOULD NOT BE DISSEMINATED BEYOND DOE.

B. Award Office Is the Source of STI Product Availability

☐ THE STI PRODUCT IS NOT AVAILABLE IN AN ELECTRONIC MEDIUM. THE AWARDING OFFICE WILL SERVE AS THE INTERIM SOURCE OF AVAILABILITY.

C. DOE Releasing Official

☐ 1. I VERIFY THAT ALL NECESSARY REVIEWS HAVE BEEN COMPLETED AS DESCRIBED IN DOE G 241.1-1A, PART II, SECTION 3.0 AND THAT THE STI PRODUCT SHOULD BE RELEASED IN ACCORDANCE WITH THE INTELLECTUAL PROPERTY/DISTRIBUTION LIMITATION ABOVE.

Release by (*name)* _____

Date ___ ___ ____
MM DD YYYY

E-Mail _____

Phone _____

REPORT DOCUMENTATION PAGE

Title and Subtitle:

AISI/DOE Final Technical Report: Project No. DE-FG36-07GO17041 Minimization of Blast Furnace Fuel Rate by Optimizing Burden and Gas Distribution

Authors:

Dr Chenn Q Zhou,
Department of Mechanical Engineering
Purdue University Calumet
Hammond, Indiana 46323, USA

Performing Organizations:

Purdue University Calumet, 2200 169th Street, Hammond, IN 46323
ArcelorMittal Steel USA R&D Center, Mittal Steel Company, East Chicago, IN 46312
ArcelorMittal-Dofasco, 1330 Burlington Street East, Hamilton, Ontario L8N 3J5
Union Gas Limited, Chatham, Ontario, Canada, N7M 5M1
US Steel Canada, Hamilton, Ontario, Canada, L8L 8K5
US Steel, Research and Technology Center, Munhall, PA, 15120
Severstal N.A. 3001 Miller Rd. Dearborn, Mi 48121

Abstract:

The goal of the research is to improve the competitive edge of steel mills by using the advanced CFD technology to optimize the gas and burden distributions inside a blast furnace for achieving the best gas utilization. A state-of-the-art 3-D CFD model has been developed for simulating the gas distribution inside a blast furnace at given burden conditions, burden distribution and blast parameters.

The comprehensive 3-D CFD model has been validated by plant measurement data from an actual blast furnace. Validation of the sub-models is also achieved. The user friendly software package named Blast Furnace Shaft Simulator (BFSS) has been developed to simulate the blast furnace shaft process. The BFSS software package has been used for the optimization of burden and gas distributions to maximize gas utilization with proper furnace permeability for given burden materials, productivities, and blast furnaces; and also to optimize the burden and gas distributions for high fuel injection rate and low coke rate. The research has significant benefits to the steel industry with high productivity, low energy consumption, and improved environment.

DOCUMENT AVAILABILITY

Reports are available free via the U.S. Department of Energy (DOE) Information Bridge:

Website: http://www.osti.gov/bridge

Reports are available to DOE employees, DOE contractors, Energy Technology Data Exchange (ETDE) representatives, and Informational Nuclear Information System (INIS) representatives from the following source:

Office of Scientific and Technical Information
P.O. Box 62
Oak Ridge, TN 37831
Tel: (865) 576-8401
Fax: (865) 576-5728
E-mail: reports@osti.gov
Website: http://www.osti.gov/contract.html

Acknowledgement: "This report is based upon work supported by the U.S. Department of Energy under Cooperative Agreement No. DE-FG36-07GO17041.

Final Technical Report

MINIMIZATION OF BLAST FURNACE FUEL RATE BY OPTIMIZING BURDEN AND GAS DISTRIBUTIONS

By

Dr. Chenn Q Zhou

August 15, 2012

Work performed under Cooperative Agreement
No. DE-FG36-07GO17041

Prepared for
U.S. Department of Energy

Submitted by
American Iron and Steel Institute
680 Anderson Drive
Pittsburgh, PA 15220

Acknowledgment: This report is based upon work supported by the U.S. Department of Energy under Award No. DE-FG36-07GO17041.

TABLE OF CONTENTS

LIST OF ACRONYMS

3-D	Three Dimensional
BF	Blast Furnace
BFSS	Blast Furnace Shaft Simulator
CFD	Computational Fluid Dynamics
CIVS	Center for Innovation through Visualization and Simulation
CZ	Cohesive Zone
GUI	Graphic User Interface
PCI	Pulverized Coal Injection
PUC	Purdue University Calumet
RAFT	Raceway Adiabatic Flame Temperature
TRZ	Thermal Reserve Zone
VBF	Virtual Blast Furnace
VR	Virtual Reality

LIST OF FIGURES

LIST OF TABLES

EXECUTIVE SUMMARY

The blast furnace process converts iron ore into molten iron and is an important component in iron-steel making. An improvement of the blast furnace fuel efficiency contributes to the reduction of energy consumption in the steel industry because this process represents about 70% of the total energy input to the integrated sector of the industry. The U.S. Department of Energy-Energy Efficiency & Renewable Energy and the American Iron and Steel Institute have been driving forces for technological improvements in iron making processes and have supported Purdue University Calumet's Center for Innovation through Visualization and Simulation (CIVS) to improve the knowledge of gas and burden distributions which are essential to the overall improvement to the optimization of the blast furnace.

The goal of the research is to improve the competitive edge of integrated steel mills by using the advanced CFD technology to optimize the gas and burden distributions inside a blast furnace for achieving the best gas utilization. A state-of-the-art 3-D CFD model has been developed for simulating the gas distributions inside a blast furnace at given burden conditions, burden distributions and blast parameters.

The comprehensive 3-D CFD model has been validated by plant measurement data from an actual blast furnace. Validation of the sub-models were also achieved. The user friendly software package named Blast Furnace Shaft Simulator (BFSS) has been developed to simulate the blast furnace shaft process. The BFSS software package may be used for the optimization of burden and gas distributions to maximize gas utilization with proper furnace permeability for given burden materials, productivities, and blast furnaces; and also to optimize the burden and gas distributions for high fuel injection rate and low coke rate. The research has significant potential benefits for the steel industry to improve productivity, lower energy consumption, and reduce environmental emissions.

The Virtual Blast Furnace (VBF) was developed by combining the virtual reality technologies with advanced CFD simulation. Visualization of the high pressure, high-temperature blast furnace operations is available. Using the BFSS and the "virtual blast furnace" software, it is possible to design, optimize, and trouble shoot blast furnace operations. If the technology is fully implemented in the U.S., the potential energy saving is 1.75 GJ/MTHM for blast furnace ironmaking, which is 80% of the calculated maximum potential energy saving of 2.19 GJ/MTHM. A reduction in the fuel consumption rate will also reduce the generation of pollutant emissions from blast furnaces.

The project team includes Purdue University Calumet (PUC), ArcelorMittal, Severstal N.A, Union Gas Limited and U. S. Steel. The research benefited education at Purdue University Calumet, which is located at Northwest Indiana, near the center of the U.S. Steel industry. Furthermore, through the technology transfer process, the BFSS software will be made available to the entire steel industry.

1 INTRODUCTION

1.1 Descriptions of the Technology

A state-of-the-art 3-D CFD model has been developed for simulating the gas distribution inside a blast furnace at given burden conditions, charging conditions and tuyere operations. The CFD model includes the major physical and chemical processes in the blast furnace such as gas-solid reductions, gas-liquid/solid heat exchange that includes the effects of reaction heat and phase changes, cohesive zone, and furnace permeability.

The BFSS is used for prediction of the gas distribution, coke rate under given burden materials, productivities, and tuyere conditions. The technological advantages of the model include:

(1) The Graphic User Interface (GUI) of the pre-processor and post-processor is integrated with the CFD solver and burden simulator. The user can set up the case, run the simulation, and analyze the results in an integrated user friendly environment.
(2) The 3-D distribution of velocity, pressure, chemical reaction, species, gas and burden temperature, reduction degree, and cohesive zone shape are available. The results can be easily analyzed by the post-processing module.
(3) Burden distribution model includes the falling curve, the stock line profile, the burden descending and the mix layer. The burden structure and charging process can be visually displayed for inspection and new charging process can be designed using this tool to maximize the gas distribution.
(4) The layer structure of the burden is explicitly considered and thus the cohesive zone is treated as individual coke and melting layer. The cohesive zone boundary is defined by an isothermal line and can be customized as a function of local burden composition.
(5) The package is able to predict coke rate, carbon rate, gas utilization. It can be used to increase the furnace fuel efficiency and reduce the CO_2 emission
(6) Virtual reality (VR) visualization module can convert the 3-D CFD results into the immersive VR environment and enable the user to “walk” inside the blast furnace and examine the simulation results.

1.2 Focus of the Technology

The BFSS and VBF can be used to investigate the impact of key operation and design parameters and to develop strategies to maximize gas utilization and fuel efficiency and to minimize blast furnace emissions.

1.3 Applications and Benefits of the Technology

The BFSS software package and VBF has significant benefits to the steel industry with high productivity, low energy consumption, and improved environment emissions. If the technology is adopted by all the U.S. blast furnaces, and a high PCI rate is achieved by optimization of burden and gas distribution, the energy consumption of blast furnaces could be reduced significantly. The target is to reduce 1.75 GJ/MTHM of energy consumption of the blast furnace, which is 80% of the total potential energy saving and corresponds to 13.9% energy savings in comparison to the actual "good practice" blast furnace energy consumption in the United States; based on the calculations using the AISI Steel Energy Tool with assumptions of 2% of the market impacted, 2.5% annual growth rate in blast furnace ironmaking, a 2 year introduction, and 10 year market saturation. Consequently, productivity of the blast furnaces will be increased and the emissions will be reduced significantly.

1.4 Commercialization of the Technology

The BFSS software package and VBF developed has been applied to various BF systems. The Technology Transfer Workshop meeting has been held, the BFSS software package has been made available to the Industry Participants for BF and other applications. Marketing of this technology for commercial usage is in progress. The Center for Innovation through Visualization and Simulation will support the CFD software and develop long-term R&D programs. The Center will focus on continuing research on advanced technologies for the steel industry for energy savings and environmental reductions. The new technology will be disseminated by AISI through its committees, publication, advertisements, and conference seminars. The center will also facilitate training programs for Blast Furnace operators, engineers, and designers, on a subscriber basis from different steel mills, who are interested in using the software.

2 BACKGROUND

2.1 Blast Furnace

Ironmaking is a capital and energy intensive process. The Blast furnace represents the predominant ironmaking process in the U.S. More than 95% of the pig iron produced from iron ore comes from the blast furnaces and since the blast furnace process can mass produce high-grade iron units efficiently, this process is likely to continue to coexist with next-generation ironmaking processes in the years ahead. The blast furnace process is a counter current moving bed chemical reactor to reduce iron oxides to iron, which involves complex transport phenomena and chemical reactions. As shown in Figure 1, in the blast furnace process, iron-bearing materials and coke with flux are charged in alternate layers into the top of the furnace. Preheated air and fuel (gas, oil or pulverized coal) is blown into the lower part of the furnace through tuyeres, forming a cavity called the raceway in which the injected fuel and some of the coke descending from the top of the furnace are combusted and gasified. The hot air burns the pulverized coal and coke and raises the temperature to more than 2,000°C, which creates carbon monoxide (CO) gas to reduce the iron ore to molten iron. The raw material is heated to 1,000°–2,000°C in the blast furnace and melts at about 1,500°C. It then separates into hot metal (molten pig iron) and slag and accumulates at the bottom of the furnace.

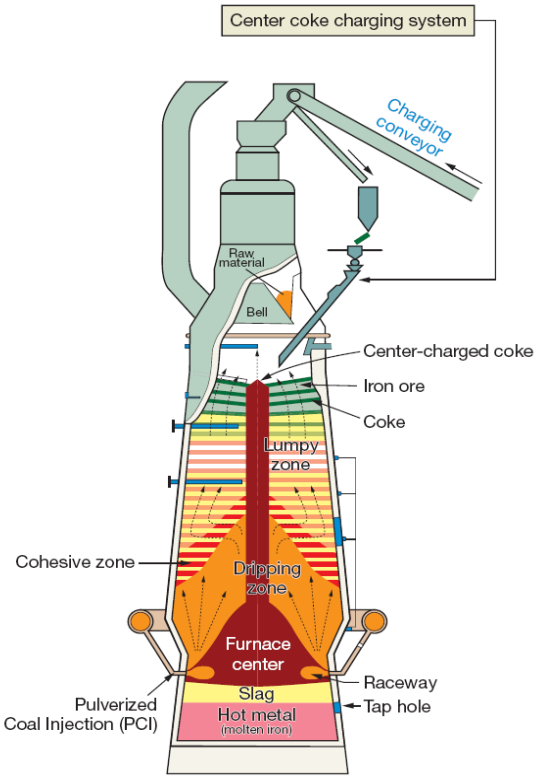

Figure 1 Schematic of a Blast Furnace (Source: Kobe Steel 2008)

The solid phase, comprised of the alternating coke and ore layers, descends slowly through the shaft of the furnace as the coke is gasified and the ore is melted lower down in the furnace. The

primary reducing agent, carbon monoxide, present in the ascending gas, is mainly formed in the raceway, which is located at the lower part of the furnace just above the hearth. The area where the ore starts to soften and finally melts is called the cohesive zone. In the cohesive zone the ore layers become virtually impermeable thus forcing the ascending gas to pass through the coke slits present between the ore-layers. The shape and location of the cohesive zone are controlled by the distribution of the burden and gas flow and impacted by the softening and melting properties of the burden materials. The cohesive zone, in turn, has a great effect on the gas distribution [Dong et al. 2003]. The fuel economy of the blast furnace process is directly coupled to the gas and burden distributions. The gas distribution strongly influences both the thermal and chemical phenomena in the lumpy zone of the furnace. The gas distribution, which also affects the pressure loss as well as productivity and smoothness of operation, is controlled mainly by manipulating the distribution of the burden and tuyere operation. The reductions of fuel consumption rate will also save energy and produce less emissions from blast furnaces.

The development of Pulverized Coal Injection (PCI) has led to substitution of coke by coal in order to meet changing economic and environmental conditions. This technology has been widely implemented. However, PCI into the blast furnace leads to low permeability in the shaft zone and the CZ. For instance, as the PCI rate increases and the amount of coke decreases, the thickness of coke layers decreases, resulting in a higher resistance for the gas in the upper shaft of the furnace. Furthermore, the experience gained so far shows that the increase of PCI rate induces important changes of gas distribution in the blast furnace which influence the whole process, the performance and the service life. Gas flow monitoring is therefore regarded as one of the keys to high PCI rates. Therefore, it is important to estimate the characteristics of the gas flow in a blast furnace.

The knowledge of gas distributions and its influential factors in a blast furnace is essential for the process optimization. However, the temperature inside blast furnace can reach as high as 2,500°C and the reduction agent carbon monoxide is highly toxic. Due to the inhospitable environment, the direct measurement of the blast furnace process is limited. One solution is to utilize the high fidelity CFD numerical simulations to understand the essence of the gas and burden distributions in the blast furnace. Recent rapid advancements in computer technology have made the development of high fidelity CFD simulations possible. Such simulations are a powerful tool that can provide detailed information on aerodynamics, heat transfer, and chemical kinetics in complex flows, and can be used to conduct extensive computer experiments for parametric and optimization studies of flow systems. Specifically, simulations can be used to (1) investigate the impact of key operation and design parameters and (2) develop strategies to maximize gas utilization and fuel efficiency and to minimize environmental emissions.

2.2 Literature Review

The importance of blast furnace burden and gas distributions has led to a number of experimental and analytical researches. In the experimental work, small-scale experiments [Poyeromo and Hlinka, 1982, Omori, 1987], or full-scale experiments [Narita et al. 1979] were carried out. Usually, experiments have been conducted without paying attention to the effect of the gas flow, but this can lead to serious misinterpretation of the burden distribution [Omori, 1987, Narita et al. 1987]. Furthermore, new experiments are required if the conditions change in the real process [Kajiwara et al, 1990]. Some efforts have been made for on-site measurements. For example, the gas distribution was measured quantitatively with differential pressure sensors, turbine meters, etc. However, due to the severe conditions in a blast furnace, it is difficult to get reliable measurements for longer periods of time [Nikus, 2001]. Use of IR-cameras for burden temperature measurement has been reported in the literature [Poos et al., 1981]. In order to get quantitative values of the gas and burden distributions from these signals, the measurements must be interpreted by some intelligent techniques.

Attempts have been made to develop analytical or numerical models based on empirical data, mass and energy balances, or CFD. Certain types of burden distribution models have been developed and used at various blast furnaces [Kajiwara et al., 1983, Hockings et al. 1988, McCarthy et al., 1993]. A 2-D CFD based model (SONDE) has been developed and applied to process guidance and gas distribution control [Burke and Burgess, 1989, Tanzil et al., 1990]. Several mathematical models of the blast furnace, which can reproduce multi-dimensional distributions of the process variables within the furnace, have been proposed [Sugiyama and M. Sugata, 1987, Austin et al. 1997 and 1998, Castro et al. 2000]. Most of these models are in 2-D frame and do not consider three-dimensional variable distributions. However, a detailed investigation demands a three-dimensional analysis and detailed inter-phase interactions. In the blast furnace process, the tuyere, which supplies hot blast and auxiliary fuels, is settled on the lower furnace wall equally spaced in the circumferential direction, representing points of three-dimensional steep variable distributions. Ohno et al. [1986] carried out 3-D analysis of gas flow taking into account the layer-by-layer structure of packed bed, and showed strong influence of ore/coke distribution and off-center charge. However no further development of this model was published. Takatani et al.[1999] presented three-dimensional model and showed several three-dimensional features in the blast furnace. Their model, however, employs some simplistic assumptions such as vertical liquid flow, constant reaction rates in the raceway and so on. It is incapable of simulating detailed three-dimensional phenomena around the combustion zone of the blast furnace.

Recently, a 3-D mathematical model of the blast furnace has been developed by de Castro et al. [2002]. The model comprehends the full circumferential blast furnace and is based on the multi-fluid theory. Special attention was devoted to analyze the lower part of the blast furnace where

the three-dimensional behavior is more evident. This model has successfully predicted the actual blast furnace operation and comparisons of predicted and measured blast furnace parameters showed good agreement. However, the focus of this study was in the lower part of the furnace.

Lowering the fuel rate of the BF process is economically and environmentally beneficial. Numerical simulation of the BF is a useful tool for predicting the situation inside the BF as well providing guidelines for optimization. Mathematical modeling of the blast furnace has been studied for the past few decades [Dong et. al 2007]. The fuel rate and gas utilization of a BF is directly related to burden and gas distribution inside the furnace. Coke and iron ore are charged alternately into the BF top. The previous studies simplified the layer structure burden as homogenous mixed layer of coke and ore [Austin et. al 1996, Austin et. al 1997]. The treatment of the CZ in the perspective of modeling could be categorized into layered and non-layered [Dong et. al 2010].

Within a blast furnace, the burden distribution plays an important role because it influences the formation, shape and location of the cohesive zone, which are essential for the gas flow distribution and gas utilization efficiency. Therefore, the suitable control of the burden distribution is required for smooth blast furnace operation. In order to predict the burden distribution, both the charging and descending processes need to be considered since burden distribution is a continuous process. Nowadays, Bell-less charging equipment was installed in most of the commercial blast furnace due to the excellent controllability.

Technically, the formation of the burden structure consists of three main steps by sequence. In the bell-less blast furnace, the first step involves the descent of the material from the discharge hopper, movement along the chute, detachment and falling of the raw material from the rotating chute. To investigate the trajectory of the raw material and the impact points at the stock line, the falling trajectory has been studied theoretically and experimentally. Nag and Koranne [2009] reported the measurements taken from the plant during the filling of a commercial blast furnace. The scaled experiment model has been reported by Liang et al. [2009]. The single particle model is developed and extensively used to compare with experimental data and to investigate effects of the chute parameters (Yu et al. [2009], Wang [2003, 2006], Liu [2005],). The detailed force and velocity analysis along the chute was carried out by Nag and Koranne [2009] and Kondoh [1977].

Secondly, with the information of the trajectory from the first step, the shape of the ring formed on previous stock profiles can be defined, thus the new stock profile is available by adding the successive rings of the entire charging. Jiménez et al. [2000] reported a semicircle 1/10 scale shaft cold experimental model and use camera to capture the ring shape of each dump. Mathematical models are also developed by Jiménez et al. [2004] to simulate the ring profile by a pair of second degree polynomials. Matsuzaki [2003] proposed that the normal distribution function could be used to describe the heap up ring profile.

Finally, the charged burden redistributes as it moves downward to form the entire burden structure. Many studies have been conducted on the descending behavior of burden. In terms of experiments, the burden structure is measured in an experiment carried out by Ichida et al. [1991]. The burden descent velocity field is characterized by a plug flow in the upper part of the shaft and a funnel flow in the lower part which is validated through the experimental work by Wright et al. [2011]. The experiment reveals that the relative size of the different solid flow zones (i.e. plug flow zone, funnel flow zone, quasi-stagnant zone, and stagnant zone) in a 2-D and 3-D scaled blast furnace differs considerably. Therefore, 3-D modeling for the burden flow velocity is necessary. In terms of mathematical modeling of the burden descending, Nishio et al. [1982] originally proposed a burden descent model for the bell-type charging furnace. In addition, Ichida et al. [1991] measured the radial distribution of burden descent velocity and further proposed a non-uniform descent model to qualitatively describe the burden descending process. In this paper, a 3-D potential flow is utilized and the corresponding burden distribution profile is obtained.

The previously mentioned research work focused only on individual steps instead of the whole process. Within the effort to combine all the models, remarkable progress has been reported by Kumar and Ram [2006], and Kajiwara et al. [1988]. However, the operating condition of the blast furnace strongly influences the burden redistribution due to the local solid consumption (Zhang et al. [1999], [2002]), i.e. ore reduction and coke gasification. Generally the burden layer thickness decreases as descending and finally the ore layers are softened and melted to form the cohesive zone.

Currently, there is no comprehensive blast furnace CFD model for guiding both the gas distribution and burden distribution to achieve optimized fuel efficiency and with the best furnace permeability. This research developed a comprehensive blast furnace CFD model and it is one of the first endeavors in the U.S.

This project is a natural extension of existing research projects in developing the state-of-the art CFD models for the evaluation of the fluid flow, heat transfer and erosion patterns in a BF hearth [Yan et al. 2005] as well as for the analysis of coal devoltilization and combustion in the BF PCI process [Zhou et al. 2006, Gu at al. 2006]. Both projects have laid a solid foundation to develop a comprehensive whole blast furnace model and to establish a long-term R&D steel program.

2.3 Objectives

There were four objectives in this research:

1) To develop a state-of-the-art 3-D CFD model for simulating the gas distribution inside a blast furnace (BF) at given burden conditions, burden distributions and blast parameters

2) To conduct measurements of top temperature and gas composition distributions as well as validations of the CFD model

3) To optimize the burden and gas distribution for maximizing gas utilization with proper furnace permeability for given burden materials, productivities, and furnaces

4) To optimize the burden and gas distributions for high fuel injection rate and low coke rate with the best fuel efficiency for given burden materials, productivities, and furnaces

3 RESULTS AND DISCUSSIONS

3.1 Burden Distribution Model

3.1.1 Falling Curve Model

The falling curve of the material during charging from rotating chute is shown schematically in Figure 2 (a) & (b). This model is based on force balance of the single charging particles and it has been widely utilized to describe the trajectory of the burden [Wang 2003, Wang 2006, Huang 2009, Liu 2005]. The movement of the raw material includes discharge hopper, sliding along the rotating chute and free falling from the chute tip.

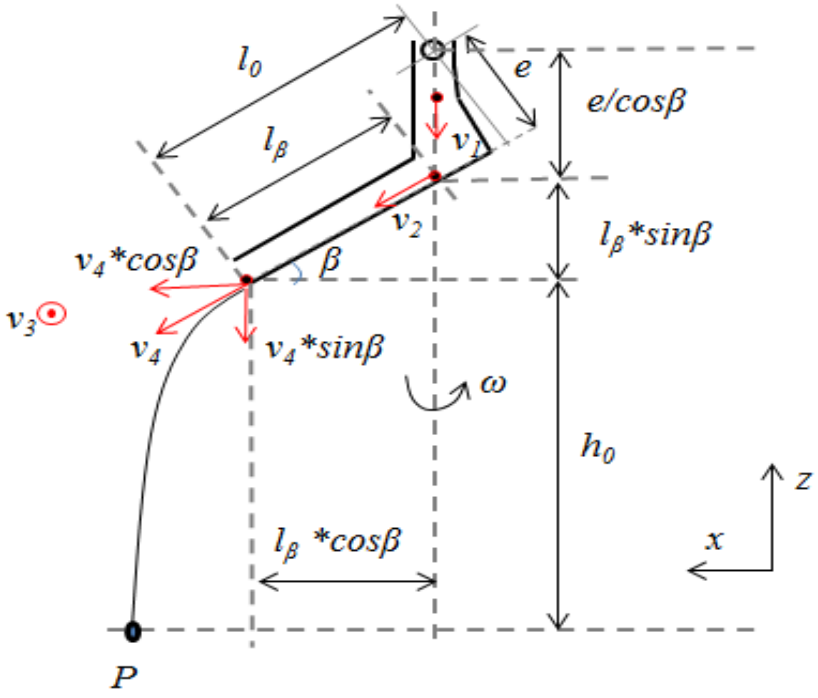

Figure 2 (a) Schematic of the falling curve model (Side view)

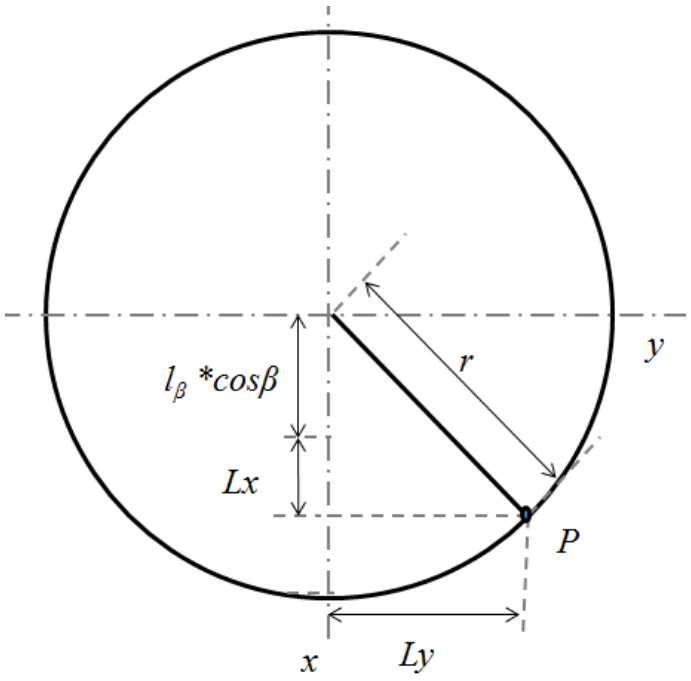

Figure 2 (b) Schematic of the falling curve model (Top view)

The initial velocity of a particle as it is leaving the material spout is given as Eq. 1. It relates initial velocity v_1 with the receiving pipe diameter D and the particle diameterd_p. Under typical blast furnace operation, the value of v_1 is about 1.0 m/s. After impacting on the chute, the velocity decreases to 0.2-0.6 m/s [Liu 2005]. Therefore, an energy dissipation coefficient Ω has been used in Eq. 2.

The velocity of a particle as it is leaving the end of feed spout is v_1 and it is assumed to have a uniform distribution at the mouth of the discharge hopper.

$$v_1 = \lambda\sqrt{3.2g(D - d_p)/4} \qquad \text{Eq. 1}$$

$$v_2 = \Omega v_1 \qquad \text{Eq. 2}$$

As the particle travels along the rotating chute, the velocity increases. The velocity components v_3 (v_3 is perpendicular pointing outward of the side view in Figure 2 (a)) and v_4 of the particle at the chute tip can be calculated as Eq. 3 and Eq. 4 by taking the frictional force, centrifugal force and gravitational force into consideration.

$$v_3 = 2\pi\omega l_\beta \cos\beta \qquad \text{Eq. 3}$$

$$v_4 = \sqrt{2g(\sin\beta - \mu\cos\beta)l_\beta + 4\pi^2\omega^2\cos\beta(\cos\beta + \mu\sin\beta){l_\beta}^2 + {v_2}^2} \qquad \text{Eq. 4}$$

where the effective chute length l_β is calculated as Eq. 5.

$$l_\beta = l_0 - e \times tan\beta \quad \text{Eq. 5}$$

The velocity at chute tip in xyz coordinate system can be expressed as Eq. 6, Eq. 7 and Eq. 8.

$$l_\beta = v_x = v_4 cos\beta \quad \text{Eq. 6}$$

$$v_y = v_3 = 2\pi\omega l_\beta \, cos\beta \quad \text{Eq. 7}$$

$$v_z = v_4 sin\beta \quad \text{Eq. 8}$$

Once the particle velocity at chute tip is available, the motion of the particle in the free space can be calculated. Under normal operation, the drag force of the particle caused by the gas is negligible for ore diameters greater than 3mm and coke diameters greater than 5mm under normal operating conditions (Wang 2006). Mass fraction of such small ore and coke is very small thus the drag force is not considered in the falling curve model. From Eq. 9, the vertical distance h_0 can be related to solve the dropping time in Eq. 10.

$$h_0 = v_z t + 0.5 g t^2 \quad \text{Eq. 9}$$

$$t = \frac{-v_z + \sqrt{{v_z}^2 + 4 \times 0.5 g h_0}}{2 \times 0.5 g} \quad \text{Eq. 10}$$

The time will be further used to compute the radial distance from Eq. 11 and Eq. 12.

$$Lx = v_x t \quad \text{Eq. 11}$$

$$Ly = v_y t \quad \text{Eq. 12}$$

$$r = \sqrt{(Lx + l_\beta \, cos\beta)^2 + Ly^2} \quad \text{Eq. 13}$$

As shown in Figure 2(b), the horizontal path of a particle, as r in Eq. 13 is the distance from the original point in xy plane to point of impact 'P'.

3.1.2 Stock Line Profile Formation Model

The stock profile is determined in the following steps shown in Figure 3. In Figure 3(a), with each revolution of the chute, the raw material falls on the stock line to form a ring shaped heap. The cross-section of the heap has been assumed to be a triangular shape where the apex of the triangle is assumed to be in the trajectory of falling path. Based on the material angle of repose, the shape of the triangle can be determined. In Figure 3(b), the volume formed by $f_1(r)$ and $f_2(r)$ equals to the charging volume. The latest stock profile is obtained by the combination of the charged ring shaped heaps over the charging sequence as shown in Figure 3(c) and (d).

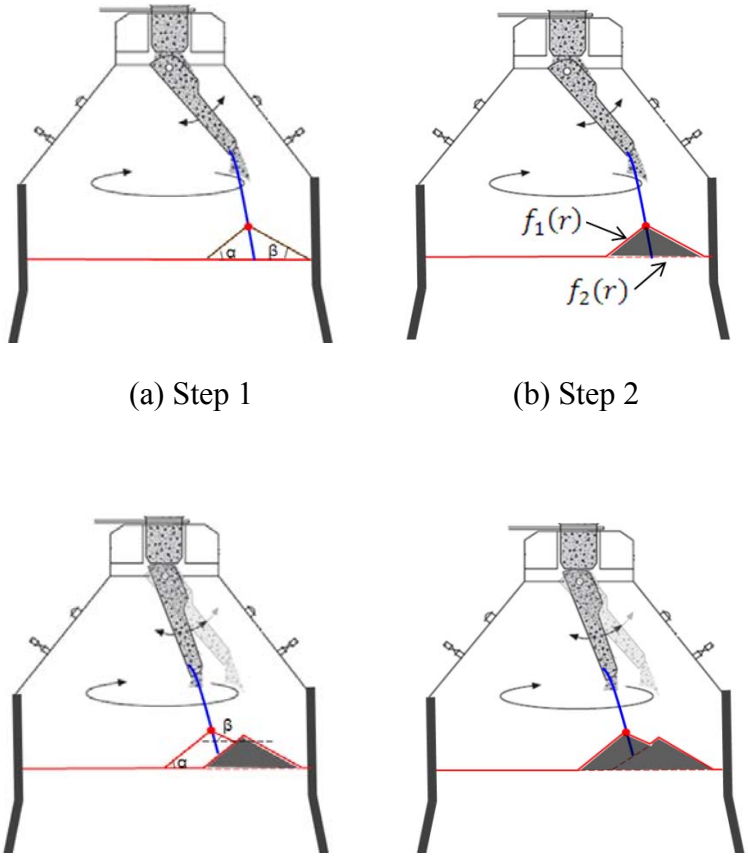

(a) Step 1 (b) Step 2

(c) Step3 (d) Step 4

Figure 3 Formation of the stock profile

The interior angles of the triangle on the impact side β are calculated by the raw material angle of repose α in Eq. 14.

$$\beta = \alpha - k \times chute\ inclination\ angle \qquad \text{Eq. 14}$$

Once the two bottom interior angles are computed, the apex of the triangle is determined iteratively until the volume formed by $f_1(r)$ and $f_2(r)$ satisfies Eq. 15.

$$Vol = \int_0^R 2\pi r[f_1(r) - f_2(r)]\,dr \qquad \text{Eq. 15}$$

3.1.3 Burden Descent Model

The bed structure in the blast furnace was determined using the burden descent model. According to some model experimental results, the burden descent velocity at the free surface corresponding to the measured values obtained by a profile meter is large at the peripheral area and small at the central area. Therefore, a burden descent model is proposed by some other researchers (Ichida et al. 1996 and Omori 1987). The burden descends in a vertical direction (blue arrow) in the throat region, as showed in Figure 4 (a). In the upper shaft region, the burden descends along the lines radiating from the cone apex 'O' located above the tapered wall, as shown in Figure 4 (a) (red arrow). The basic assumption of the model is the burden possesses the same vertical descent velocities, which results in the relative burden descent velocity at the peripheral area are larger than that at the inner burden.

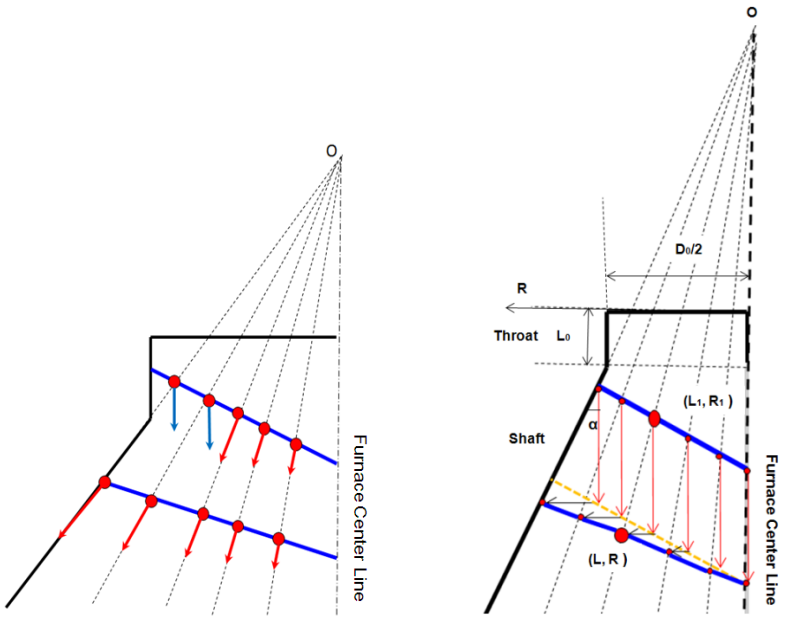

(a) Burden velocity profile (b) Burden descent in shaft

Figure 4 Schematic of burden descent model

As illustrated in Figure 4(b), in a blast furnace of throat diameterD_0, height $L_0$and a shaft angle from the vertical of α, any particle in a charge with the volume V_{charge} moves from the point (L_1, R_1) to the point (L, R) along a line. This movement of the particle is formulated as follows. When the particle is located in the throat region ($L_1 < L_0$), the vertical length after one charging will be determined by the load volume V_{charge} over the cross-section area of throat as shown in Eq. 16. Since the assumption of vertical descent within the throat, the radius length is expressed as Eq. 17.

$$L = \frac{4 \times V_{charge}}{\pi {D_0}^2} + L_1 \quad \text{Eq. 16}$$

$$R = R_1 \quad \text{Eq. 17}$$

When the particle is located in the shaft region ($L_1 > L_0$), the vertical length after one load will be calculated by Eq. 18. Both Eq. 16 and Eq. 18 are based on the volume conservation which suggests the descent volume is equal to the charging volume. The radius length is derived by the principle of similar triangles as expressed in Eq. 19.

$$L = \left[\left(\frac{D_0}{2\tan\alpha} - L_0 + L_1\right)^3 + \frac{3V_{charge}}{\pi(\tan\alpha)^2}\right]^{\frac{1}{3}} - \frac{D_0}{2\tan\alpha} + L_0 \quad \text{Eq. 18}$$

$$R = R_1 \frac{\frac{D_0}{2\tan\alpha} - L_0 + L}{\frac{D_0}{2\tan\alpha} - L_0 + L_1} \quad \text{Eq. 19}$$

For the belly part, the descent pattern is assumed the same as the shaft due to the geometry similarity as shown in Figure 5. As for the bosh part, it is analogous to the shaft part by employing Eq. 20 and Eq. 21.

$$L = -\left(\left(\frac{D_{belly}}{2\tan\beta} - (L_1 - L_3)\right)^3 - \frac{3V_{charge}}{\pi(\tan\beta)^2}\right)^{\frac{1}{3}} + \frac{D_{belly}}{2\tan\beta} + L_3 \quad \text{Eq. 20}$$

$$R = R_1 \frac{\frac{D_{belly}}{2\tan\beta} - (L - L_3)}{\frac{D_{belly}}{2\tan\beta} - (L_1 - L_3)} \quad \text{Eq. 21}$$

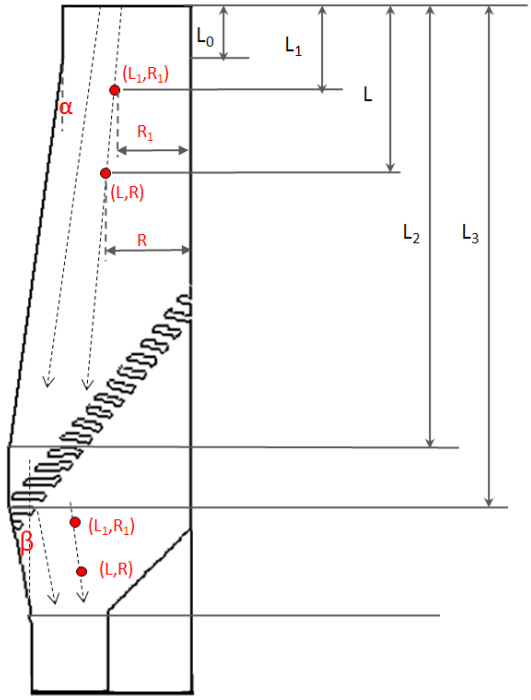

Figure 5 Geometry profile of burden descent model

3.2 Mathematical Formulation of the CFD Model

3.2.1 Gas Phase Governing Equations

In the 3-D mathematical model, the ascending gas is described as the gas phase. The generalized governing conservation equations for gas phases are expressed as the following:

Gas continuity equation

$$\frac{\partial}{\partial x}\left(\rho_g u_g\right)+\frac{\partial}{\partial y}\left(\rho_g v_g\right)+\frac{\partial}{\partial z}\left(\rho_g w_g\right)=\mathrm{S}_g \qquad \text{Eq. 22}$$

Gas x-momentum equation

$$\begin{aligned}\frac{\partial}{\partial x}\left(\rho_g u_g u_g\right)+\frac{\partial}{\partial y}\left(\rho_g v_g u_g\right)+\frac{\partial}{\partial z}\left(\rho_g w_g u_g\right)&\\ =\frac{\partial}{\partial x}\left(\mu_{eff}\frac{\partial u_g}{\partial x}\right)+\frac{\partial}{\partial y}\left(\mu_{eff}\frac{\partial u_g}{\partial y}\right)+\frac{\partial}{\partial z}\left(\mu_{eff}\frac{\partial u_g}{\partial z}\right)-\frac{\partial p}{\partial x}+\frac{\partial}{\partial x}\left(\mu_{eff}\frac{\partial u_g}{\partial x}\right)&\\ +\frac{\partial}{\partial y}\left(\mu_{eff}\frac{\partial v_g}{\partial x}\right)+\frac{\partial}{\partial z}\left(\mu_{eff}\frac{\partial w_g}{\partial x}\right)+S_{Mx}&\end{aligned} \qquad \text{Eq. 23}$$

Gas y-momentum equation

$$\frac{\partial}{\partial x}(\rho_g u_g v_g) + \frac{\partial}{\partial y}(\rho_g v_g v_g) + \frac{\partial}{\partial z}(\rho_g w_g v_g) = \frac{\partial}{\partial x}\left(\mu_{eff}\frac{\partial v_g}{\partial x}\right) + \frac{\partial}{\partial y}\left(\mu_{eff}\frac{\partial v_g}{\partial y}\right) + \frac{\partial}{\partial z}\left(\mu_{eff}\frac{\partial v_g}{\partial z}\right) - \frac{\partial p}{\partial y} + \frac{\partial}{\partial x}\left(\mu_{eff}\frac{\partial u_g}{\partial y}\right) + \frac{\partial}{\partial y}\left(\mu_{eff}\frac{\partial v_g}{\partial y}\right) + \frac{\partial}{\partial z}\left(\mu_{eff}\frac{\partial w_g}{\partial y}\right) + S_{My} \quad \text{Eq. 24}$$

Gas z-momentum equation

$$\frac{\partial}{\partial x}(\rho_g u_g w_g) + \frac{\partial}{\partial y}(\rho_g v_g w_g) + \frac{\partial}{\partial z}(\rho_g w_g w_g) = \frac{\partial}{\partial x}\left(\mu_{eff}\frac{\partial w_g}{\partial x}\right) + \frac{\partial}{\partial y}\left(\mu_{eff}\frac{\partial w_g}{\partial y}\right) + \frac{\partial}{\partial z}\left(\mu_{eff}\frac{\partial w_g}{\partial z}\right) - \frac{\partial p}{\partial z} + \frac{\partial}{\partial x}\left(\mu_{eff}\frac{\partial u_g}{\partial z}\right) + \frac{\partial}{\partial y}\left(\mu_{eff}\frac{\partial v_g}{\partial z}\right) + \frac{\partial}{\partial z}\left(\mu_{eff}\frac{\partial w_g}{\partial z}\right) + S_{Mz} \quad \text{Eq. 25}$$

Gas energy conservation equation

$$\frac{\partial}{\partial x}(\rho_g u_g h_g) + \frac{\partial}{\partial y}(\rho_g v_g h_g) + \frac{\partial}{\partial z}(\rho_g w_g h_g) = \frac{\partial}{\partial x}\left(\frac{k_{g,eff}}{C_{p,g}}\frac{\partial h_g}{\partial x}\right) + \frac{\partial}{\partial y}\left(\frac{k_{g,eff}}{C_{p,g}}\frac{\partial h_g}{\partial y}\right) + \frac{\partial}{\partial z}\left(\frac{k_{g,eff}}{C_{p,g}}\frac{\partial h_g}{\partial z}\right) + S_{g,h} \quad \text{Eq. 26}$$

Gas species conservation equation

$$\frac{\partial}{\partial x}(u_g C_{g,i}) + \frac{\partial}{\partial y}(v_g C_{g,i}) + \frac{\partial}{\partial z}(w_g C_{g,i}) = \frac{\partial}{\partial x}\left(D_{i,eff}\frac{\partial C_{g,i}}{\partial x}\right) + \frac{\partial}{\partial y}\left(D_{i,eff}\frac{\partial C_{g,i}}{\partial y}\right) + \frac{\partial}{\partial z}\left(D_{i,eff}\frac{\partial C_{g,i}}{\partial z}\right) + S_{g,c} \quad \text{Eq. 27}$$

For compressible gas, the ideal gas law is employed to calculate the gas density.

$$\rho_g = \frac{PM_{mix}}{RT} \qquad \text{Eq. 28}$$

The standard k-ε model was used to model turbulence. This model was chosen due to its excellent performance with relatively simple modeling. It is also one of the simplest and also complete turbulence models, known for its robustness and economy. The k-ε model is a semi-empirical model which is based on the transport equations for the turbulence energy (k) and its dissipation rate (ε) expressed as Eq. 29 and Eq. 30 respectively.

$$\frac{\partial}{\partial x}(\rho_g u_g k) + \frac{\partial}{\partial y}(\rho_g v_g k) + \frac{\partial}{\partial z}(\rho_g w_g k) = \frac{\partial}{\partial x}\left(\frac{\mu_{eff}}{\sigma_k}\frac{\partial k}{\partial x}\right) + \frac{\partial}{\partial y}\left(\frac{\mu_{eff}}{\sigma_k}\frac{\partial k}{\partial y}\right) + \frac{\partial}{\partial z}\left(\frac{\mu_{eff}}{\sigma_k}\frac{\partial k}{\partial z}\right) + G - \rho_g \varepsilon \qquad \text{Eq. 29}$$

$$\frac{\partial}{\partial x}(\rho_g u_g \varepsilon) + \frac{\partial}{\partial y}(\rho_g v_g \varepsilon) + \frac{\partial}{\partial z}(\rho_g w_g \varepsilon) = \frac{\partial}{\partial x}\left(\frac{\mu_{eff}}{\sigma_\varepsilon}\frac{\partial \varepsilon}{\partial x}\right) + \frac{\partial}{\partial y}\left(\frac{\mu_{eff}}{\sigma_\varepsilon}\frac{\partial \varepsilon}{\partial y}\right) + \frac{\partial}{\partial z}\left(\frac{\mu_{eff}}{\sigma_\varepsilon}\frac{\partial \varepsilon}{\partial z}\right) + \frac{\varepsilon}{k}(C_1 G - C_2 \rho_g \varepsilon) \qquad \text{Eq. 30}$$

The production term is expressed as:

$$G = \mu_{eff}\left\{2\left[\left(\frac{\partial u_g}{\partial x}\right)^2 + \left(\frac{\partial v_g}{\partial y}\right)^2 + \left(\frac{\partial w_g}{\partial z}\right)^2\right] + \left(\frac{\partial u_g}{\partial y} + \frac{\partial v_g}{\partial x}\right)^2 + \left(\frac{\partial u_g}{\partial z} + \frac{\partial w_g}{\partial x}\right)^2 + \left(\frac{\partial v_g}{\partial z} + \frac{\partial w_g}{\partial y}\right)^2\right\} \qquad \text{Eq. 31}$$

The flow is assumed to be fully turbulent throughout the computational domain. The gas effective viscosity is expressed as:

$$\mu_{eff} = \mu + \frac{C_\mu \rho k^2}{\varepsilon} \qquad \text{Eq. 32}$$

where C_μ is a constant. The value of the k-ε model constants are determined by experimentations with air and water and have been found to be satisfactory for all flow paradigms. The values used are given in Table 1.

Table 1 k-ε model constants

C_μ	C_1	C_2	σ_k	σ_ε
0.09	1.44	1.92	1.0	1.3

The gas flow inside the porous medium is modeled by adding a momentum source term to the standard fluid flow equations. The source term contributes to the pressure gradient in the porous cell, creating a pressure drop that is proportional to the fluid velocity (or velocity squared) in the cell. It is composed of two parts: a viscous loss term and an inertial loss term. For simple homogeneous porous media, the source term can be written, using the Brinkman equation as:

$$S_{M_j} = \frac{\mu}{\alpha} U_j + C_2 \frac{\rho |U_j|}{2} U_j \qquad \text{Eq. 33}$$

where μ is the viscosity, α is the viscous loss coefficient, and C_2 is the inertial resistance factor. The following equations can be used to calculate α and C_2.

$$\alpha = 150 \frac{(\psi d_p)^2 e^3}{(1-e)^2} \qquad \text{Eq. 34}$$

$$C_2 = 3.5 \frac{(1-e)}{(\psi d_p) e^3} \qquad \text{Eq. 35}$$

where d_p is the mean particle diameter , ψ is the shape factor and e is the void fraction. The void fraction e is defined as the volume of voids divided by the volume of the packed bed region.

3.2.2 Burden Phase Governing Equations

The potential flow model has been utilized in blast furnace burden flow modeling [Saw et al. 1991, Danloy et al. 2001, Park et al. 2011]. Since the solid flow behavior with layers of different materials and a homogeneous mix of materials are similar [Wright et al. 2011], the burden density ρ_b is taken as the averaged density of the mixed layer. Below the cohesive zone, it is assumed that the solid coke and the coexisting liquid melt shares the same temperature [Omori 1987] and the same velocity. The condensed burden phase is defined as the gross bed, i.e. the combination of the solid and liquid [Yang et al. 2010, Burke et al. 1989].

The Burden continuity equation:

$$\frac{\partial}{\partial x}(\rho_b u_b) + \frac{\partial}{\partial y}(\rho_b v_b) + \frac{\partial}{\partial z}(\rho_b w_b) = S_b \qquad \text{Eq. 36}$$

With the introduction of the potential function

$$u_b = -\frac{\partial \phi_b}{\partial x} \qquad \text{Eq. 37}$$

$$v_b = -\frac{\partial \phi_b}{\partial y} \quad \text{Eq. 38}$$

$$w_s = -\frac{\partial \phi_b}{\partial z} \quad \text{Eq. 39}$$

The burden continuity equation becomes Eq. 40

$$\frac{\partial}{\partial x}\left(\rho_b \frac{\partial \phi_b}{\partial x}\right) + \frac{\partial}{\partial y}\left(\rho_b \frac{\partial \phi_b}{\partial y}\right) + \frac{\partial}{\partial z}\left(\rho_b \frac{\partial \phi_b}{\partial z}\right) = -S_b \quad \text{Eq. 40}$$

Burden energy conservation equation

$$\frac{\partial}{\partial x}(\rho_b u_b h_b) + \frac{\partial}{\partial y}(\rho_b v_b h_b) + \frac{\partial}{\partial z}(\rho_b w_g h_g) = S_{b,h} \quad \text{Eq. 41}$$

Burden composition (species) conservation equation

$$\frac{\partial}{\partial x}(u_b C_{b,i}) + \frac{\partial}{\partial y}(v_b C_{b,i}) + \frac{\partial}{\partial z}(w_g C_{b,i}) = S_{b,c} \quad \text{Eq. 42}$$

Both the gas phase and burden phase consists of different species (composition). The list of all species of each phase treated in the model is presented in Table 2.

Table 2 Species considered for each phase

Phase	Species		
Gas	CO, CO_2, H_2, H_2O, N_2		
Burden	Solid	Ore	Fe_2O_3, Fe_3O_4, FeO, Fe, SiO_2, Al_2O_3, CaO, MgO, MnO, K_2O+Na_2O, Ti_2O, H_2O
		Coke	C, SiO_2, Al_2O_3, CaO, MgO, H_2O
	Liquid	Slag	FeO, SiO_2, Al_2O_3, CaO, MgO
		Hot Metal	Fe, C

3.3 Phenomenological CFD Sub-models

3.3.1 Chemical Reactions Sub-model

The major chemical reactions in an ironmaking blast furnace are mainly gas-solid reactions. The following reactions, including nine gas-solid reactions and two phase transformations are considered in the model.

Indirect reduction of iron oxide by carbon monoxide:

$$3Fe_2O_3(s) + CO(g) \rightarrow 2Fe_3O_4(s) + CO_2\ (g) \quad (1)$$

$$Fe_3O_4(s) + CO(g) \rightarrow 3FeO(s) + CO_2\ (g) \quad (2)$$

$$FeO(s) + CO(g) \rightarrow Fe(s) + CO_2\ (g) \quad (3)$$

Indirect reduction of iron oxide by hydrogen:

$$3Fe_2O_3(s) + H_2(g) \rightarrow 2Fe_3O_4(s) + H_2O\ (g) \quad (4)$$

$$Fe_3O_4(s) + H_2(g) \rightarrow 3FeO(s) + H_2O\ (g) \quad (5)$$

$$FeO(s) + H_2\ (g) \rightarrow Fe(s) + H_2O\ (g) \quad (6)$$

Coke gasification:

$$C(s) + CO_2 \rightarrow 2CO\ (g) \quad (7)$$

$$C(s) + H_2O(g) \rightarrow CO + H_2\ (g) \quad (8)$$

Decomposition of Flux Stone ($MgCO_3$ is converted to equivalent mass of $CaCO_3$ and only $CaCO_3(s) \rightarrow CaO(s) + CO_2\ (g)$ is included in the present model):

$$MeCO_3(s) \rightarrow MeO(s) + CO_2(g)\ ,\ Me=Ca, Mg \quad (9)$$

Water evaporation:

$$H_2O(l) \rightarrow H_2O\ (g) \quad (10)$$

Melting of iron:

$$Fe(s) \rightarrow Fe\ (l) \quad (11)$$

3.3.1.1 Reduction of Iron oxides

Two models are included in the CFD code for the indirect reduction reactions (1-6). The first mode is the unreacted shrinking core (URC) model as the expression of single-pellet reaction kinetics [Xie et al. 1984, Strassburger 1996 , Omori 1987]. The reduction of iron ore proceeds via the successive steps $Fe_2O_3 \rightarrow Fe_3O_4 \rightarrow FeO \rightarrow Fe$. As shown in Figure 6, the URC model assumes that the reduction of an iron oxide sphere occurs at the surface with the formation of an

outer shell of metallic iron. The shell grows in the radial direction until the entire oxide is completely reduced to iron.

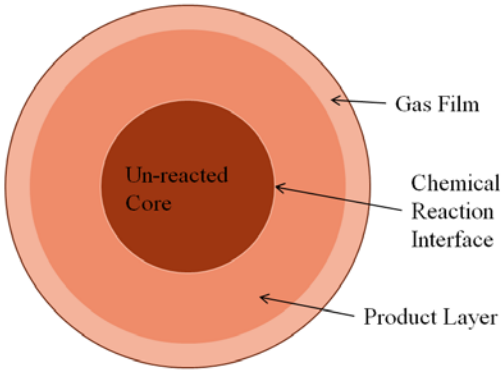

Figure 6 Schematic representation of un-reacted shrinking core model

The complex process of iron ore reduction has been simplified to three rate control processes, namely, gas film resistance, diffusion resistance through the reduced iron shell, and reaction resistance at the metal-oxide interface. The expression for the reaction rate is expressed as Eq. 43.

$$R_{(r-s)} = \frac{4\pi r_0^2\left(C_A - \frac{C_B}{K_{e(r-s)}}\right)}{\frac{1}{\beta_A} + \frac{r_0}{D_e}\left[\frac{1}{\left(1-f_{(r-s)}\right)^{1/3}} - 1\right] + \frac{K_{e(r-s)}}{k_{(r-s)}(1+K_{e(r-s)})} \cdot \frac{1}{\left(1-f_{(r-s)}\right)^{2/3}}} \qquad \text{Eq. 43}$$

where the fraction of reduction is defined as Eq. 44:

$$f_{(r-s)} = \frac{weight\ of\ oxygen\ removed\ from\ iron\ oxide}{weight\ of\ removable\ oxygen} \times 100\ \% \qquad \text{Eq. 44}$$

It is concluded that for blast furnace operation, gas film resistance, diffusion resistance through the reduced iron shell may be neglected [Xie et al. 1984] and chemical reaction resistance may be dominant. It is shown that while the kinetic controlled rate expression may not necessarily involve all the details of the reaction mechanism, it is still able to adequately represent the overall time course of the reduction.

The second model [Figure 7] is the grain model. The grain model assumes that the reaction is taking place within a zone rather that constrained in the interface. Gas diffusion into the pellet is included and the distribution of the oxides concentration along the radius needs to be modeled.

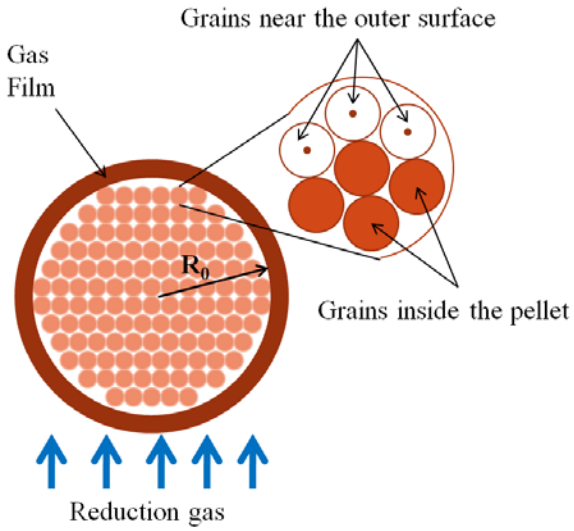

Figure 7 Schematic representation of grain model

Governing equations are summarized from literature as the following [Huang et al. 1996, Valipour 2007]:

$$\frac{1}{r}\frac{\partial}{\partial r}\left(D_{\mathrm{CO}}^{e}\frac{\partial(rc_{\mathrm{CO}})}{\partial r}\right)-v_0=0 \qquad \text{Eq. 45}$$

$$\frac{1}{r}\frac{\partial}{\partial r}\left(D_{\mathrm{CO_2}}^{e}\frac{\partial(rc_{\mathrm{CO_2}})}{\partial r}\right)+v_0=0 \qquad \text{Eq. 46}$$

$$\frac{\partial T_s}{\partial t}=\frac{1}{rC_p\rho(1-\varepsilon)}\frac{\partial}{\partial r}\left(\lambda\frac{\partial(rT_s)}{\partial r}\right)-\frac{v_0\Delta H_i}{C_p\rho(1-\varepsilon)} \qquad \text{Eq. 47}$$

For any unit volume inside the pellet, the reduction rate can be of different expressions and one expression is given as Eq. 53 [Huang et al. 1996].

$$v_0=\psi_{\mathrm{mg}}S_0X_0^{\alpha}k_i\frac{c_{\mathrm{CO}}-c_{\mathrm{CO_2}}/K_{\mathrm{pi}}}{\delta\frac{k_i}{D_e'}+1} \qquad \text{Eq. 48}$$

Where v_0 is the reduction rate of the concentrates, mol/ (cm^3.s); ψ_{mg} is the volumetric fraction of the iron concentrate inside the pellet; S_0 is the specific surface area, cm^2/cm^3;X_0 is the local un-reacted degree; α is the shape factor of the concentrate, D_e', effective diffusive coefficient of CO through the surface layer, cm^2/s; c_{CO}, $c_{\mathrm{CO_2}}$ are the concentrations of CO, CO_2 inside the pellet; K_{pi} is the reaction equilibrium; k_i is the reaction constant, cm/s. For any grain, the equivalent thickness of the reacted product layer or grain radius can be expressed as Eq. 49 [Huang et al. 1996].

$$\delta = r_0 \mathrm{e}^{\beta(1-\frac{1}{(1-X_0)^{\gamma}})} \quad \text{Eq. 49}$$

Where r_0 is the mean value of fine grain size (cm); β and γ are the micro-structure of the fine pellets and the fracture factor respectively.

3.3.1.2 Reaction of coke in shaft

Blast furnace coke undergoes three main reactions in the shaft. These are the Boudouard reaction (7), the water-gas reaction (8) and the direct reduction reaction (C + FeO → Fe+ CO) which is, kinetically, a combination of reaction (3) and reaction (7) or a combination of reaction (6) and reaction (8). The Boudouard reaction going to the right is also known as the endothermic gasification of carbon or the solution-loss reaction. The unreacted core model [Yuji et al. 1989] is utilized to model the coke reaction (7) and (8). Due to the high porosity of the coke particle, the diffusion resistance is neglected [Huang 2008].

3.3.1.3 Flux decomposition

The flux decomposition reaction (8) is greatly dependent on the decomposition pressure. The unreacted core model is also applied to the flux decomposition reaction (Huang 2008).

3.3.1.4 Other reactions

It is concluded that the water-gas shift reaction ($CO + H_2O(g) \rightarrow CO_2 + H_2$) and other reactions may be neglected in the blast furnace [Strassburger, 1969].

3.3.2 Heat and Mass Transfer Sub-model

3.3.2.1 Heat and Mass Transfer Coefficient

The empirical relation [Akiyama et al. 1993] was used for the convective heat transfer coefficient of a spherical porous pellet in the counter-current moving bed. The expressions for the Nusselt and Sherwood numbers [Valipour et al. 2007] are given below.

$$Sh_i = 2 + 0.39 Re_p^{1/2} Sc_i^{1/3} \quad \text{Eq. 50}$$

$$Nu = 2 + 0.39 Re_p^{1/2} Pr^{1/3} \quad \text{Eq. 51}$$

Heat transfer coefficient between solid and gas in the furnace with a scaling factor γ which is proposed by Hatano et al. [1982] is adopted in the model:

$$h = \gamma \cdot Nu \cdot K_g / d_p \quad \text{Eq. 52}$$

3.3.2.2 Gas Diffusivity

Molecular binary diffusivity is estimated by the use of the Fuller-Schettler-Giddings equation [Fuller et al. 1966]:

$$D_{ij} = \frac{1 \times 10^{-7} T^{1.75}}{P_t \left(\bar{v}_i^{1/3} + \bar{v}_j^{1/3}\right)^2} \left(\frac{1}{M_i} + \frac{1}{M_j}\right)^{0.5} \quad \text{Eq. 53}$$

The diffusion volume used is given in Table 3.

Table 3 Diffusion volume for gas species

Molecule	H_2	H_2O	CO	CO_2	N_2
$\bar{v}$	7.07	12.7	18.9	26.9	17.9

Molecular diffusivity of a certain species in the gaseous mixture is expressed as following [Anthony, 2001]:

$$D_i = \frac{1 - y_j}{\frac{y_j}{\sum_{i \neq j} D_{ij}}} \quad \text{Eq. 54}$$

Effective diffusivity inside pellet is given by Eq. 55

$$D_{eff.i} = \frac{\epsilon}{\tau} D_i \quad \text{Eq. 55}$$

Effective diffusivity in the packed bed is expressed by Yagi [1957] as Eq. 56.

$$D_{eff\_bed,i} = 0.179 Re \times Sc \times D_i \quad \text{Eq. 56}$$

3.3.2.3 Gas Thermal Conductivity

The thermal conductivity of the gas mixture is given by Rosner [1986]

$$K_g = \frac{\sum_j y_i K_{gj} M_j^{1/3}}{\sum_j y_i M_j^{1/3}} \quad \text{Eq. 57}$$

The thermal conductivity of each gas component is taken from the data fitting by Donskoi et al. [Donskoi et al. 2003]

$$K_{gi} = A \times 10^{-2} + B \times T^{-1} + C \times 10^{-5} T + C \times 10^{-8} T^2 \quad \left(\frac{W}{m \cdot K}\right) \quad \text{Eq. 58}$$

Effective thermal conductivity in the packed bed is expressed by Yagi [1957] as Eq. 59.

$$K_{eff\_bed,g} = 0.179Re \times Pr \times K_{gi} \quad \text{Eq. 59}$$

3.3.3 Cohesive Zone Sub-model

The cohesive zone upper boundary is set to a constant temperature, but the lower boundary is treated as the local liquidus temperature. The liquidus temperature has been set as function of slag composition. To obtain such function, the data reported by Osborn et al. [1954] was used to perform the regression analysis [Figure 8]. Polynomial regression was employed to calculate the liquidus temperature for the CaO-MgO-SiO_2-Al_2O_3 system. By selecting the range of BF slag in the range of CaO 25-55 wt.%, SiO_2 25-55 wt.%, MgO <25 wt.% and Al_2O_3 <25 wt.%. The liquidus temperature is calculated as Eq. 60.

$$\begin{aligned} T_{liquidus}(C) = s &+ a_1 \times (Al_2O_3\%) + b_1 \times (CaO\%) + c_1 \times (MgO\%) + d_1 \times (SiO_2\%) \\ &+ a_2 \times (Al_2O_3\%)^2 + b_2 \times (CaO\%)^2 + c_2 \times (MgO\%)^2 + d_2 \\ &\times (SiO_2\%)^2 + a_3 \times (Al_2O_3\%)^3 + b_3 \times (CaO\%)^3 + c_3 \times (MgO\%)^3 \\ &+ d_3 \times (SiO_2\%)^3 \end{aligned} \quad \text{Eq. 60}$$

The coefficients were determined by third order polynomial regression as listed in Table 4

Table 4 Coefficient for liquidus temperature calculation

S	19230.7	a_1	-203.96	a_2	-0.6061	a_3	0.02512
		b_1	-167.45	b_2	-1.4049	b_3	0.01752
		c_1	-220.31	c_2	1.83228	c_3	-0.0394
		d_1	0.0	d_2	-5.668	d_3	0.04935

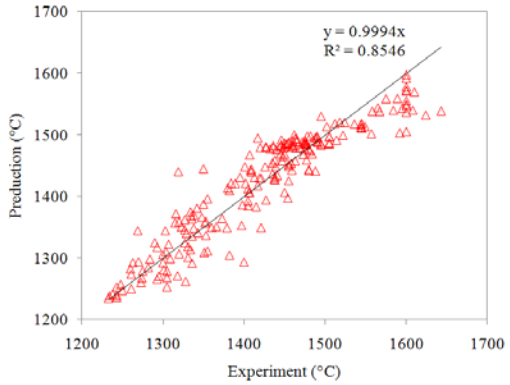

Figure 8 Comparison of the prediction results with the data reported by Osborn et al. [1954]

The impact of FeO on liquidus temperature is estimated by the correlation [Zhao 2004].

$$\Delta T_{liquidus}(C) = -8.0 \times FeO\% \quad \text{Eq. 61}$$

3.3.4 Coke Rate Sub-model

The coke rate of BF is measured and available from operational data. Nevertheless, the coke rate under steady state BF operation is determined by the demanding furnace chemical reactions. It can be computed once all the coke consumption in BF is summarized from CFD results. Practically, the computed coke rate and the reported coke rate should be within acceptable discrepancy. The coke rate sub-model is developed for two purposes: (1) verify the reported coke rate at given condition, and (2) predict the coke rate for different tuyere operations and burden distributions. The coke rate is subject to the fuel injection and hot metal productivity. As illustrated in Figure 9, the following assumptions are made for the BF process:

(1) The injected coal and gas takes place below the shaft-raceway interface, i.e., in the lower bosh region.
(2) The reduction of Si, Mn and P all takes place below the shaft-raceway interface. The amount of reduced Si, Mn, and P are from hot metal analysis.
(3) Since the carburization of the iron, i.e., carbon dissolved in hot metal $3Fe+C=Fe_3C$, is found to be active in the dripping zone [Jin et al. 2010], it is assumed to take place below the shaft-raceway interface.

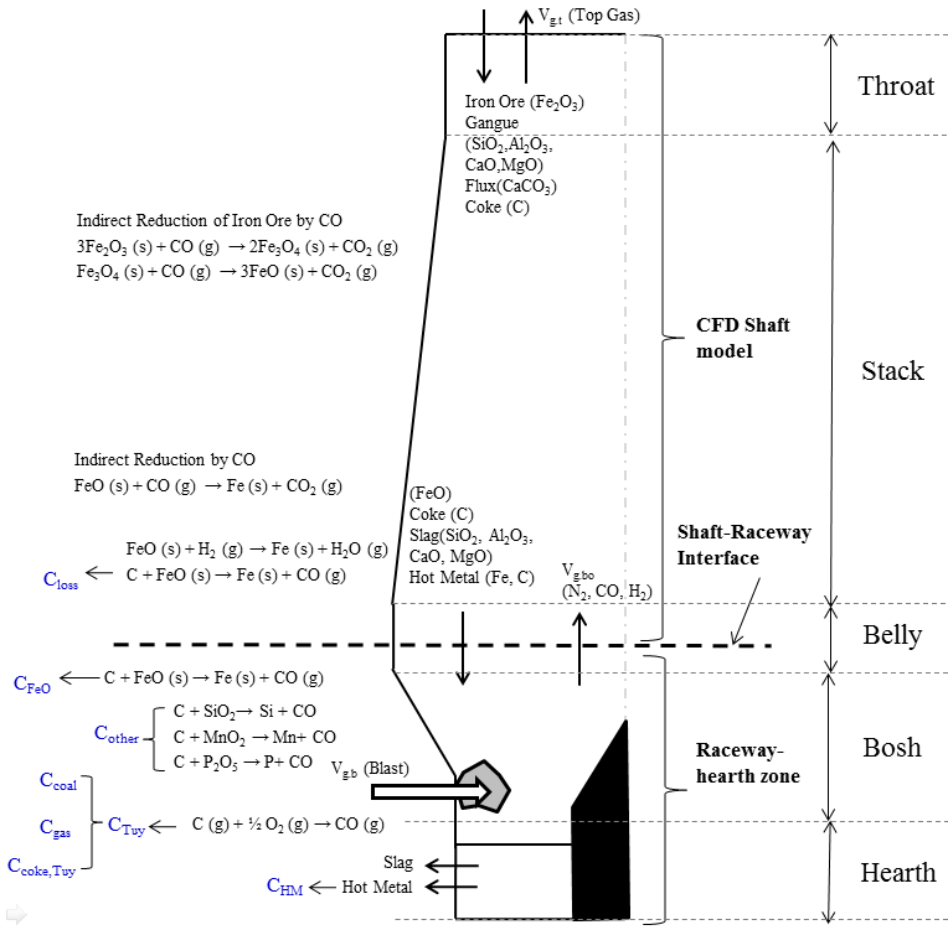

Figure 9 Schematic of carbon consumption in the BF

Figure 10 shows the flowchart of the iterative procedure to determine the coke rate. The total carbon rate below the shaft-raceway interface C_{bosh} is fixed for the specified tuyere condition and hot metal analysis. The coke rate is determined by the solution loss in the shaft region which is summarized from all the cells of the shaft CFD model. The updated coke rate is set as new boundary condition until the solution loss converges. The under relaxation technique is applied when updating the coke rate.

In the case of any un-reduced FeO existing at the shaft model outlet, the FeO is eventually converted into Fe by direct reduction below the interface. The effects of the un-reduced FeO on gas compositions and temperature at the interface are also considered. The detailed of the treatment of the un-reduced FeO is described in the next section.

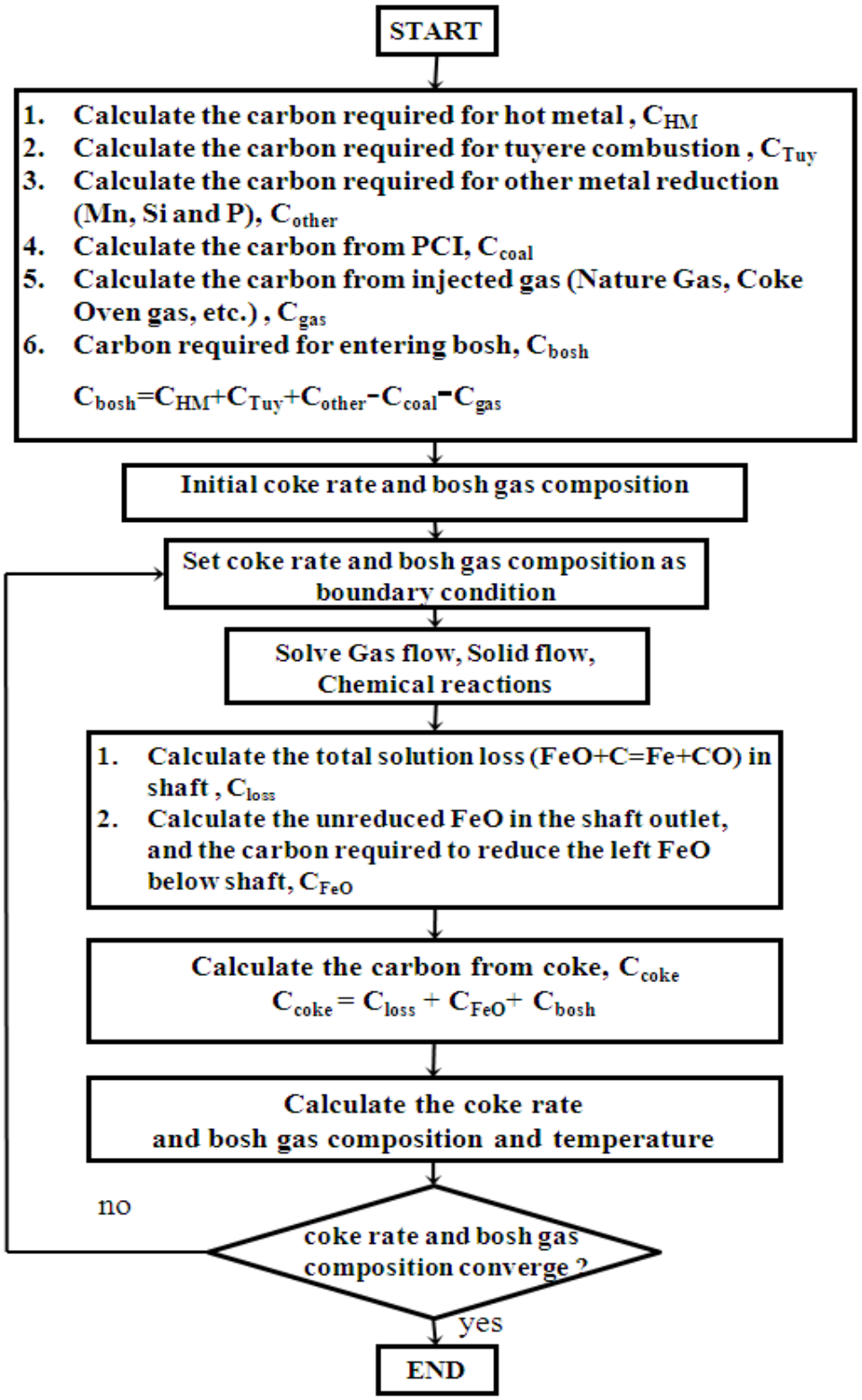

Figure 10 Flowchart of the iterative routine for coke rate

3.3.5 Sub-model for Interface Gas Temperature and Concentration Correction

The distribution of the gas compositions and temperature at the shaft-raceway interface is mapped from the kinetic CFD raceway model. However, in addition to raceway combustion, the bosh gas temperature and compositions are also affected by the following factors.

(1) The un-reduced FeO entering the interface
(2) The temperature of coke, slag and hot metal entering the interface
(3) The reduction of Mn, Si, and P

Therefore the distribution of the gas velocity species and temperature are still mapped from the CFD raceway model but multiplied by a correction factor to ensure the total mass and heat balance. The heat balance is determined by a thermodynamic model schematically shown in Figure 11 and expressed by Eq. 62.

$$Q_{Coke,in} + Q_{Slag,in} + Q_{HM,in} + Q_{Tuy,in} + Q_{Rxn,in} = Q_{loss} + Q_{Bosh,out} + Q_{Slag,out} + Q_{HM,out} \quad \text{Eq. 62}$$

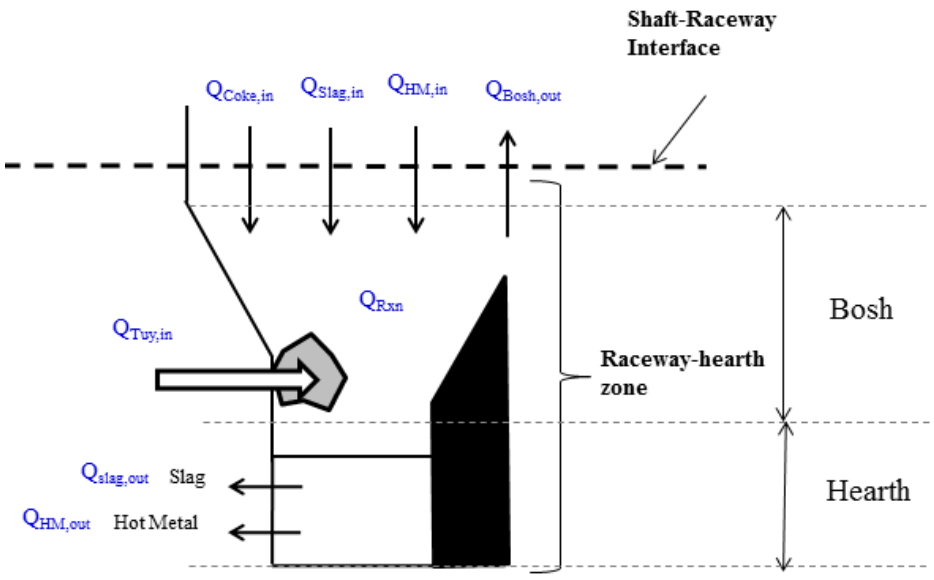

Figure 11 Heat balance below the shaft-raceway interface

The heat of the reaction below the interface consists primarily of the 8 reactions listed in Table 5, and the reaction heat is obtained from the corresponding references.

Table 5 Reaction considered in the thermodynamic model

No.	Reaction	Reaction Heat	Reference
1	$C+0.5O_2 \rightarrow CO$	ΔH= +3947 kJ/kg CO	Strassburger 1969
2	$H_2O \rightarrow H_2+0.5O_2$	ΔH= -120885 kJ/kg H_2	Strassburger
3	$CH_4 \rightarrow C+2H_2$	ΔH= -4677 kJ/kg CH_4	Strassburger
4	$2C+SiO_2 \rightarrow Si+2CO$	ΔH= -22426 kJ/kg Si	Nan 2005
5	$C+MnO \rightarrow Mn+CO$	ΔH= -5222 kJ/kg Mn	Nan
6	$5C+P_2O_5 \rightarrow 2P+5CO$	ΔH= -26255 kJ/kg P	Nan
7	$FeO+C \rightarrow Fe+CO$	ΔH= -2792 kJ/kg Fe	Strassburger
8	Coal Devolatilization	ΔH= -1045kJ/kg coal	Nan

3.3.6 Cohesive Zone Sub-model

The layered CZ is employed since it better describes the gas flow inside the CZ, i.e., the gas flow through the coke slits and the gas is blocked by the melting ore layer which is almost impermeable. The CZ upper boundary is set to the softening temperature, and the lower boundary is defined by the liquidus temperature. Updating the CZ with the iso-temperature line could result in a dramatic change of the gas flow due to porosity distribution difference. The iteration of the numerical solution is unstable and divergence frequently occurs. An under-relaxation procedure is adopted to obtain convergence. The concept is similar to a numerical under-relaxation. However, the CZ boundary is a surface in the 3-D domain. The coordinates of the new boundary is based on the previous "old" CZ boundary and the iso-temperature surface. The under-relaxation factor α is set to 0.5 for stable and converged CZ shape. The iterative procedures are listed in the following and illustrated in Figure 12.

(1) Assume a cohesive zone (CZ) to initialize the burden structure for CFD simulation, as shown in Figure 12(a) with blue profile of y_2(Upper Boundary) and y'_2 (Lower Boundary)
(2) Obtain the burden temperature distribution using the converged CFD results
(3) Determine the isothermal lines from CFD results with the softening temperature of iron ore (upper boundary) and the liquidus temperature (lower boundary), as shown in Figure 12(a) with dot red profile of y_1(Upper Boundary) and y'_1 (Lower Boundary)
(4) Update the CZ profile with the previous CZ shape and the isothermal line using the under-relaxation scheme. The updated CZ is shown in dashed white profile of y_3(Upper Boundary) and y'_3 (Lower Boundary)
(5) Repeat steps 2-4 until the shape of cohesive zone converges as shown in Figure 12(b) and (c)

The lower boundary of the CZ also defines the dripping zone where the melting hot metal and slag trickle through the packed coke bed. The degradation of coke in the dripping zone may become severe due to many factors, such as shattering and abrasion in the upper shaft, solution

loss reaction in the lower shaft, alkaline attack, high temperature attack and etc. Based on sampling results [Jin et al. 2010] of the coke diameter distribution in the bosh region, porosity 0.35 (0.65 solid volume fraction) is used in the dripping zone.

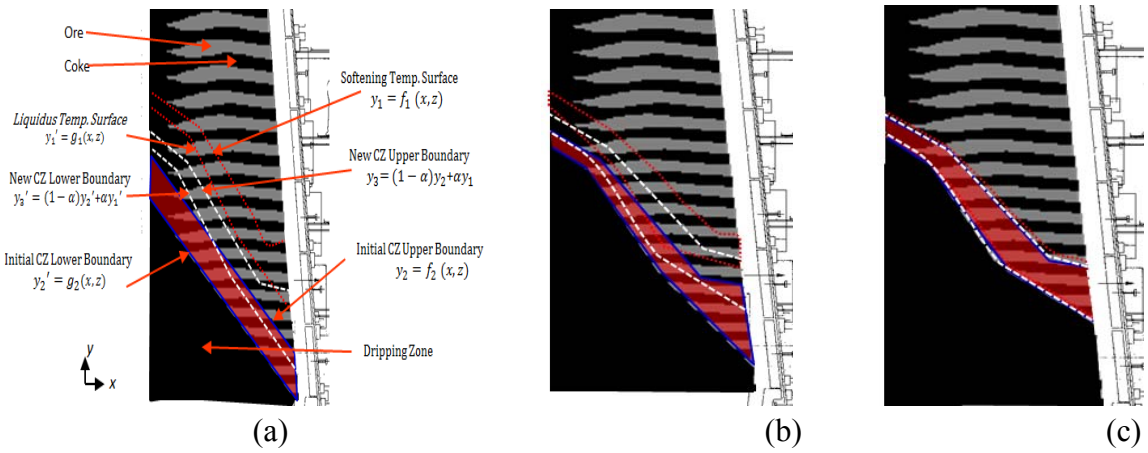

Figure 12 Under-relaxation scheme of the CZ shape

3.3.7 Mixed Layer Sub-model

When iron ore is charged above the coke layer, due to the size difference and density difference, the iron ore layer will mix with the coke layer thus the mixed layer forms and the permeability of the bed decreases. The mixed layer model proposed by Szekely and experimentally validated by Fu et al. [1981] is utilized. The mixed factor is defined as Eq. 63.

$$R = \frac{d_{upper\_layer}}{d_{lower\_layer}} \qquad \text{Eq. 63}$$

The additional pressure drop caused by the mixing effect can be calculated by Eq. 64 in the valid range of 1<R<6.

$$\Delta P_{surf} = 3.4R^{2.7}\rho v \qquad \text{Eq. 64}$$

3.4 Numerical Scheme

3.4.1 Computational Cells and Staggered Grids

The arrangement for a cross-section of the three-dimensional flow simulation is shown in Figure 13. The scalar variables are stored at the nodes (●) and the velocities are defined at the cell faces in between the nodes and are indicated by arrows. The u-velocities are stored at the cell faces e and w, and the v-velocities at the cell faces n and s. In a three-dimensional flow, the w-velocities

are evaluated at the cell faces t and b. The control volumes for the velocity components are different from the scalar control volumes.

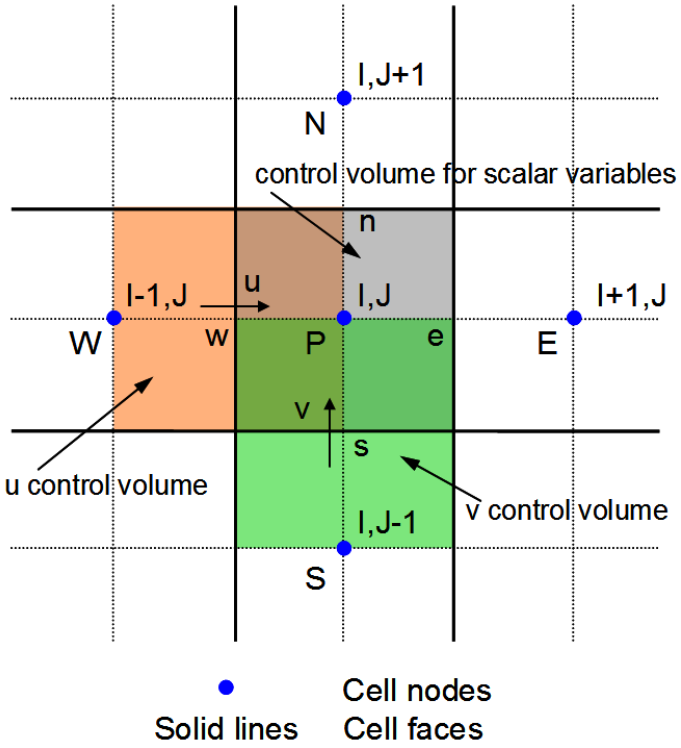

Figure 13 Staggered locations for u, v and scalar variables

The governing equations for the gas phase and the solid/liquid phase in a Eulerian frame of reference are integrated over the control volume in each computational cell to obtain the finite difference equations. A Tri-diagonal matrix algorithm (TDMA) with under-relaxation factors is applied to solve the finite difference equations. The convection-diffusion flux is evaluated using an upwind scheme, and the coupling of pressure and velocity of the gas phase is solved by the SIMPLEC algorithm [Versteeg and Malalasekera, 1995] with TDMA line-by-line sweeping. A similar procedure is used for the burden phase, but without pressure-velocity corrections. Iterations between the gas phase and the burden phase are adopted to achieve convergence of the two phases.

3.4.2 Discrete of Governing Equations

All of the conservation equations have been cast into a standard equation format. This allows for use of a single finite differencing structure and greatly simplifies the solution techniques and model computer programming. A finite volume approach is used to show the governing equations for the gas phase and the solid/liquid phase in the computational domain. The discrete governing equations can be written in the following general form as Eq. 65.

$$a_p \emptyset_p = a_E \emptyset_E + a_W \emptyset_W + a_N \emptyset_N + a_S \emptyset_S + a_B \emptyset_B + a_T \emptyset_T + b \quad \text{Eq. 65}$$

Detailed information regarding determination of the coefficients in the above equation can be found in Patankar [1980] or other books on computational fluid dynamics. All the scalar variables such as pressure, temperature and gas concentrations etc. are computed at the cell nodes, while a back-staggered grid is employed for the velocity components. Thus, the velocity components are stored at the cell faces.

3.5 Validations

3.5.1 Validation of Sub-Models

3.5.1.1 Validation of Falling Curve Model Sub-Model

In order to ensure the proposed model is able to represent the physical characteristics of the burden formation, the plant trial data from published literature [Nag et, al. 2009] is used for a partially validation of the simulated results for the same operation conditions. By the arrangement shown in Figure 14, the trajectory of the falling materials can be measured during the filling of the blast furnace. The trajectory location can be calculated using the images captured by the cameras.

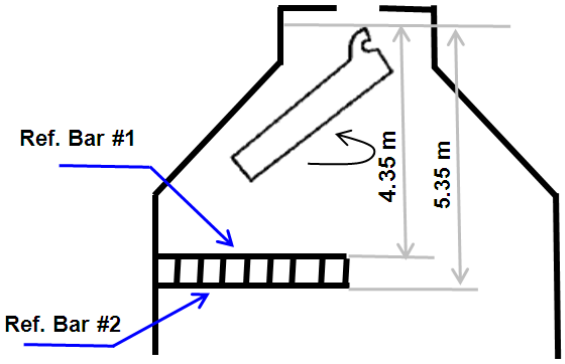

Figure 14 Schematic of experimental setup [Nag et, al. 2009]

Figure 15 compares the experimentally observed landing positions of coke with the simulated results as a function of chute inclination angle. Figure 16 presents the corresponding results for sinter. The two sets of data in either figure represent two different stock levels (5.35m and 4.35m below the hinge point of chute), from which it is discovered that the estimating accuracy of coke has been raised, compared to that of the sinter simulation. It is stated in the literature that the experimental results for sinter were not as reliable as that for coke due to significantly higher

dust generation during charging of sinter. In addition, it is of interest to notice that the deviation increases as the chute inclination angle decreases.

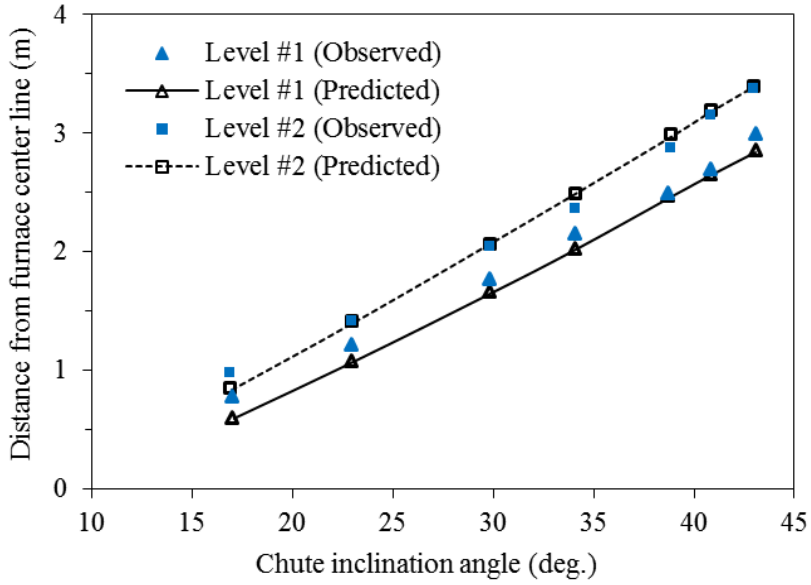

Figure 15 Comparison between simulation results and experimental data for coke

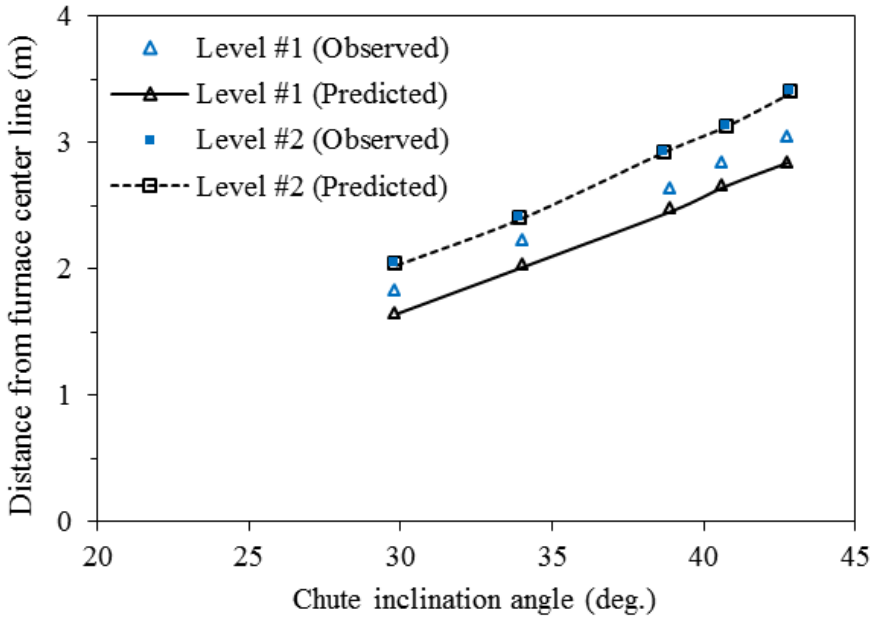

Figure 16 Comparison between simulation results and experimental data for sinter

Overall, the simulated results agree well with both sets of data. Comparisons indicate that the mathematical model can predict the influence of chute inclination angle on the radial landing position(s) of coke and sinter at a given stock level with acceptable accuracy.

3.5.1.2 Validation of Stock-line Profile Formation Sub-Model

A 1/10 scale model was built by Jiménez [2000] to investigate the charging layer formation on the top of the blast furnace. Coke and ore were charged ring by ring and pictures of the layer profile after each dump were taken with the CCD camera. A special algorithm was developed to obtain the boundary of each layer, i.e. the layer profile, from the pictures. Since the Froude number (Fr) is consistent in the model and the actual blast furnace, the scaled model results can be extended to a full scale furnace by scaling up factor of 10. Table 6 lists the charging pattern employed in the experiment and used in the simulation. The coefficient k used in Eq. 14 is determined as 0.7, and the angle of repose is set to 34° in the simulation. The chute dimension and furnace geometry are specified according to the experiment apparatus. The distance between the throat top and the chute joint is estimated to be 0.37 m.

Table 6 Charging pattern for coke [8]

Ring	1	2	3	4	5	6	7	8	9	10	11
Angle (°)	2	12	22	28	32	35	38	41	44	47	50
Weight (kg)	0	1.42	1.29	1.08	1.00	1.21	1.29	1.29	1.42	0	0

The stock-line profile is formed by successive charged rings. The initial profile specified prior to running the simulation is identical with the previous stock-line profile obtained by the experiment. Figure 17 (a) shows the intermediate profile after the first actual charged ring (No.2) is dumped. The development of the stock-line profile is shown in Figure 17 (b). It can be seen that as the ring number increases, the repose angle on the impact side is decreased due to the increment of the chute angle.

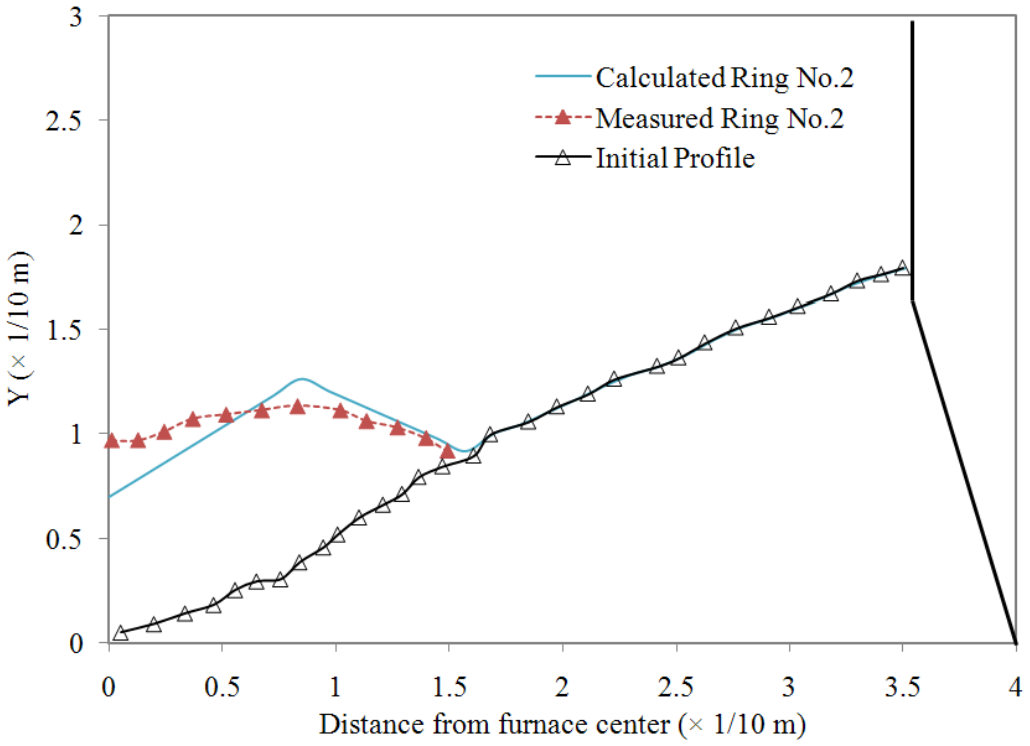

(a) First charging

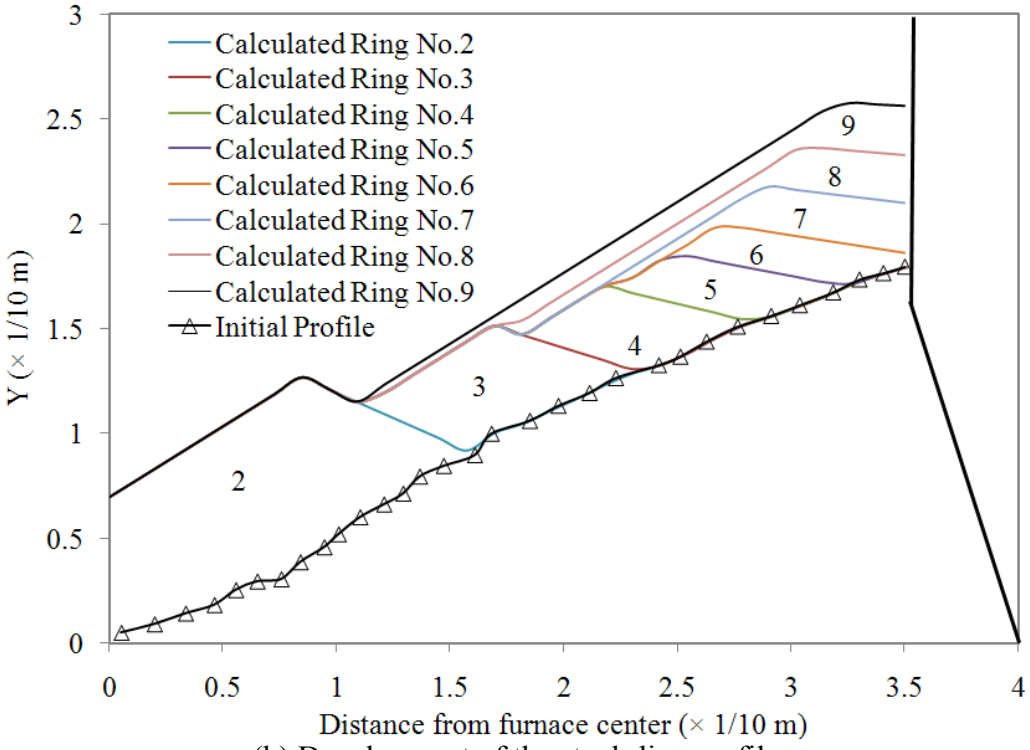

(b) Development of the stock-line profile

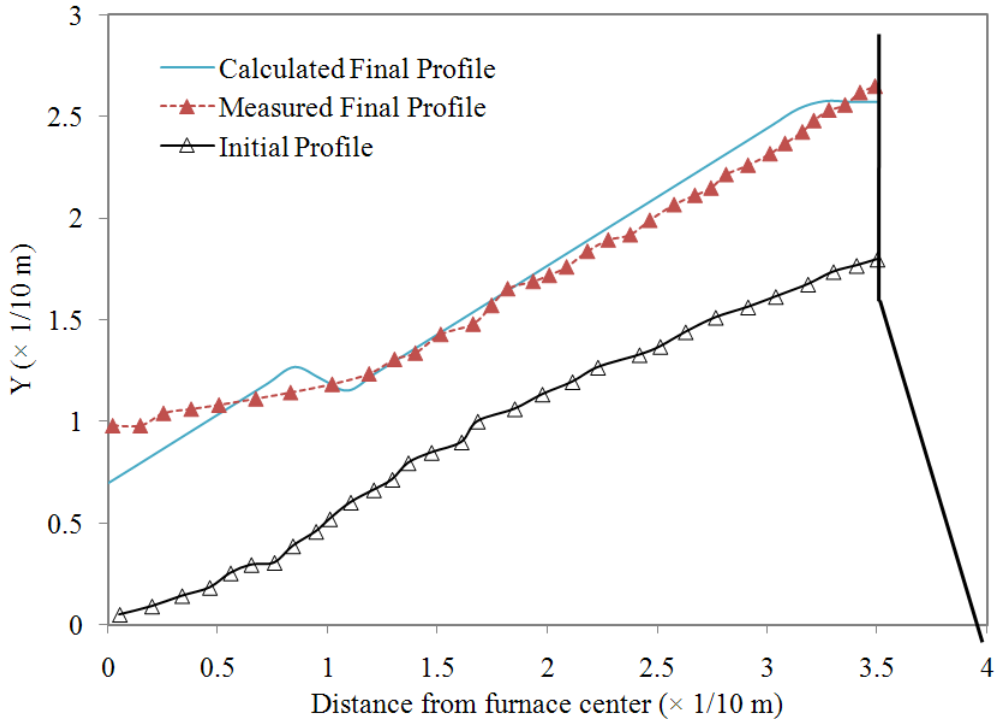

(c) Final stock-line profile

Figure 17 Comparison between calculated results and experimental data for stock-line profile

Figure 17 (c) demonstrates the comparison of the final stock-line profile when the entire set of the rings is charged into the furnace. Figure 17 (a) and (c) show good agreement between the experimental data and the predictions.

3.5.1.3 Validation of Burden Descent Sub-Model

Ichida et al. [1991] conducted experiment to study the descending behavior of the blast furnace burden by using a three-dimensional semicircular 1/20 scale physical model. The reported data has been used for validation of the burden descent model. As shown in Figure 18 and Figure 19, the initial top layer profile is specified according to the experimental results. The calculated results at different time lines are obtained by matching the center point of each layer with experimental results. The inclination angle of each layer reduces as the burden descends. Two cases with different initial profiles, i.e., A and B, are compared with experimental results.

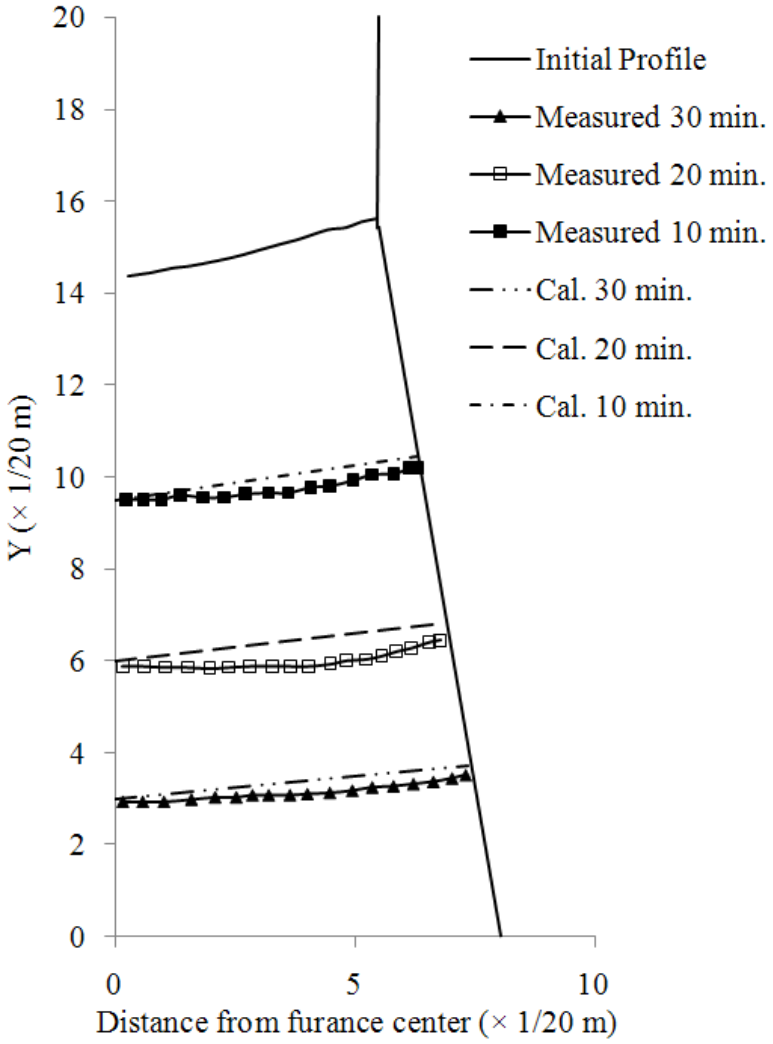

Figure 18 Comparison between calculated results and experimental data for burden descent

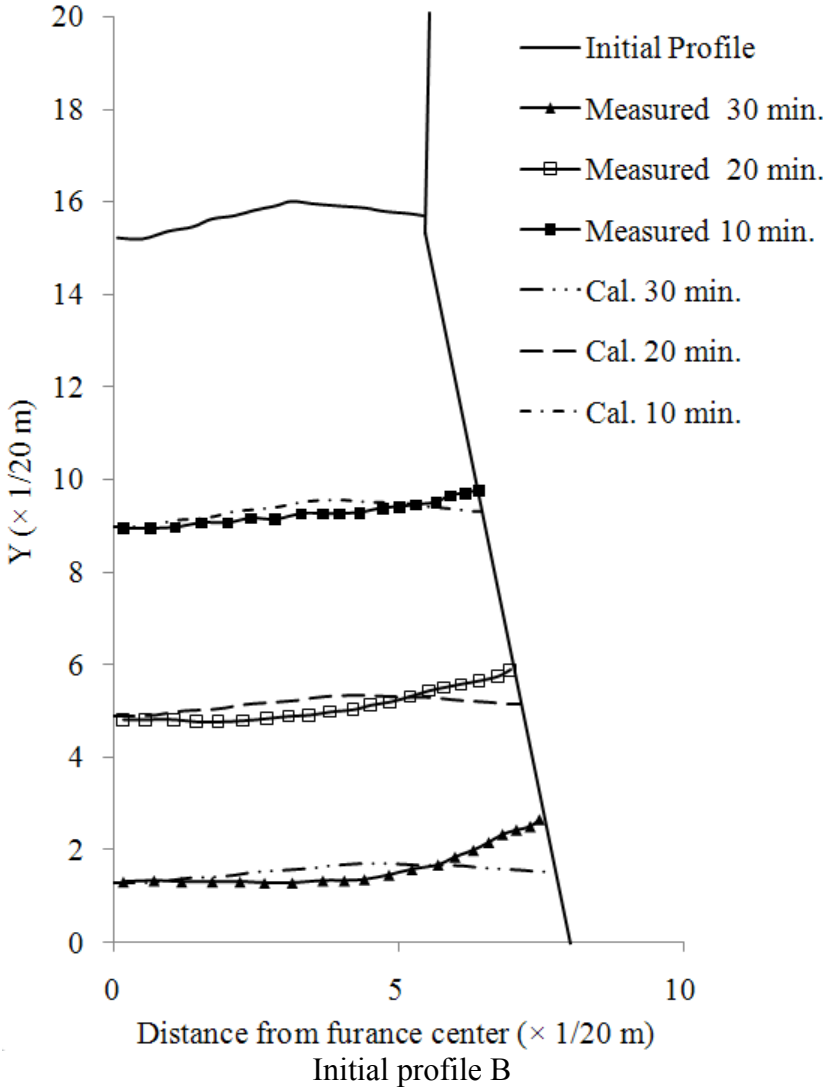

Figure 19 Comparison between calculated results and experimental data for burden descent

3.5.1.4 Validation of Gas Flow Sub-Model

In order to check if the CFD model is constructed properly, the cold experimental data from published literature [Chen et al. 1992] is used for a preliminary validation of the CFD model results based on the same conditions for experiments. The experimental apparatus for validation is schematically illustrated in Figure 20. A transparent acrylic pipe with 149 mm diameter and 700 mm height was used as a cylindrical column. The packed bed was charged in layer-by-layer structure with the inclination angle of 21.9º and a total layer number of 10. The height of the packed bed was 420 mm.

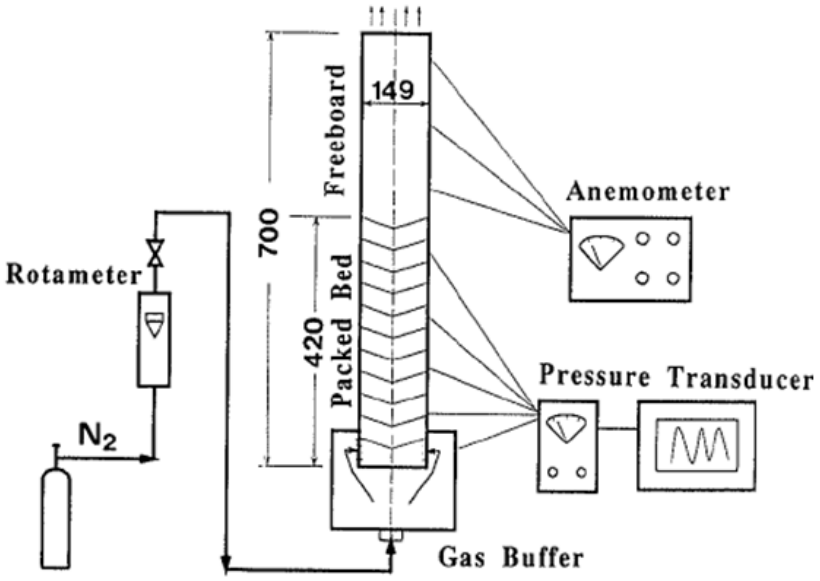

Figure 20 Schematic diagram of the experimental apparatus [Chen et al. 1992]

Nitrogen cylinders were used to provide the gas. Alumina balls and a binary mixture of glass beads were used as the packing materials to simulate the coke and ore layer in a blast furnace, respectively. The simulation parameters are shown in Table 7.

Table 7 Validation conditions

Superficial Velocity	0.195 m/s
Gas Density	1.15 kg/ m^3
Gas Viscosity	1.78×10^{-5} kg/m.s
Coke (Alumina Balls) Porosity	0.3902
Ore (Binary Mixture) Porosity	0.3070
Coke (Alumina Balls) Diameter	3 mm
Ore (Binary Mixture) Diameter	2.05 mm
Coke (Alumina Balls) Shape Factor	1.0
Ore (Binary Mixture) Shape Factor	0.9

The calculated iso-pressure line by CFD and measured pressure data are shown in Figure 21 and the parity plots are shown in Figure 22. The lateral gas is jetted from one side of the cylinder as indicated by the blue arrow. It can be seen that the pressure distributions agree well with the

experimental data. A maximum error of 9% is obtained when compared with the experimental results. Thus it is seen that the CFD model is accurate and is also able to predict actual physical trends accurately and within acceptable limits.

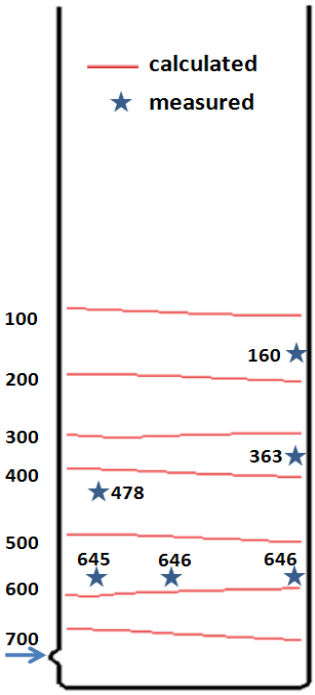

Figure 21 Comparison of experimental and CFD predictions, Unit: Pa

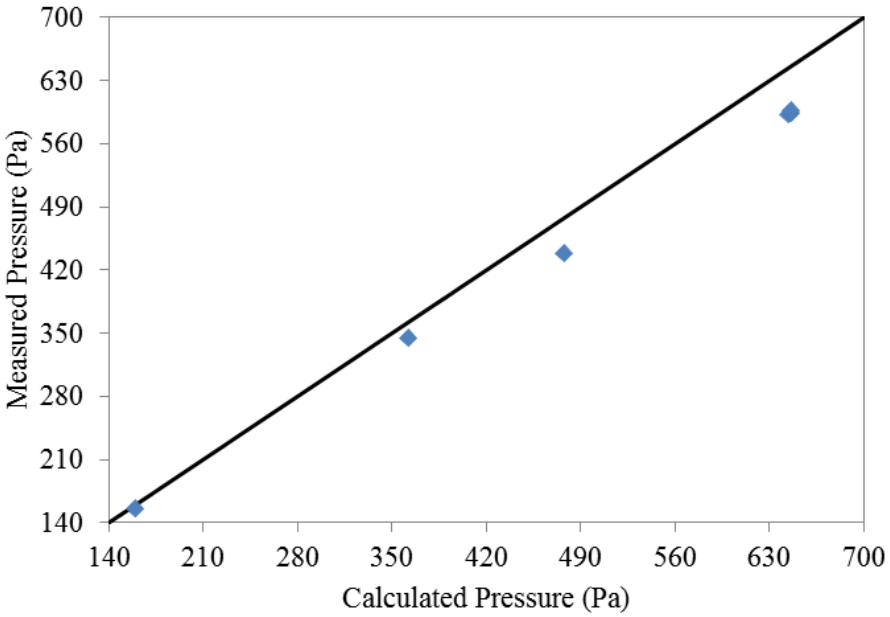

Figure 22 Parity plots for pressures at measured locations

3.5.1.5 Validation of Chemical Reaction Sub-Model

Figure 23 shows the method in which the calibration of the gas-solid reactions was conducted. The single pellet model was developed to simulate the behavior of an individual iron ore pellet. Then a bench model was developed to take the effects of packed bed into consideration. A series of reducibility experiments were conducted. The kinetics of reductions was studied by measuring the weight loss as a function of time. The experimental work was carried out under the ISO 4695 [ISO 2007] method by ArcelorMittal Global R&D, one of the industry partners. The calibrated reaction constants are then used in the full scale model.

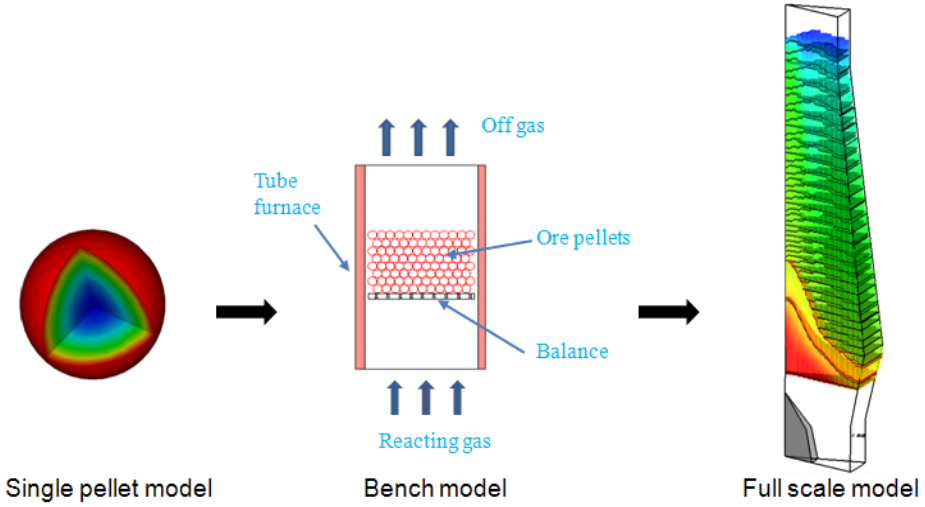

Figure 23 Calibration of the gas-solid reactions

3.5.2 Validation of Comprehensive CFD Model Using Plant Measurement

The top gas temperature distribution along the throat radius of the CFD results with the plant measurement is shown in Figure 24 for both days of operation. The temperature is measured from the center of the BF towards the northwest direction and southeast direction. The measured center temperature is significantly lower than the calculated value. One possible reason is that the furnace is not in a symmetric condition to the geometric center. The fluctuation of the temperature of the northwest side and the southeast side near the center may also indicate the asymmetry.

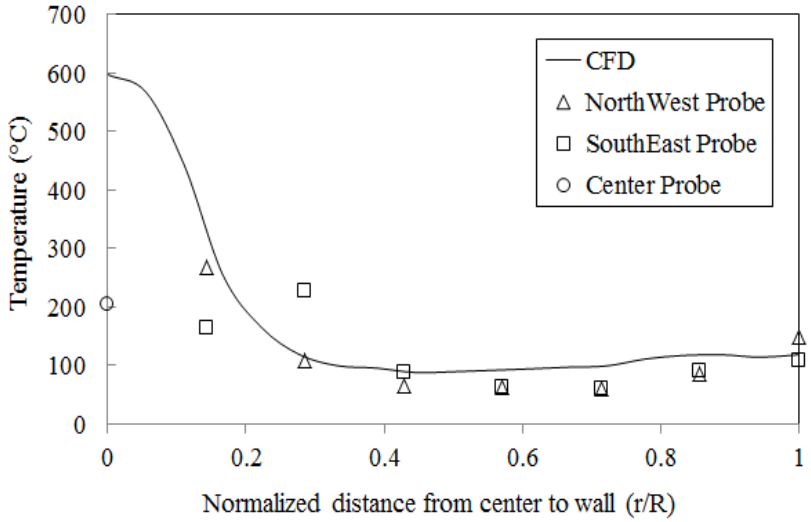

(a) August 23rd data

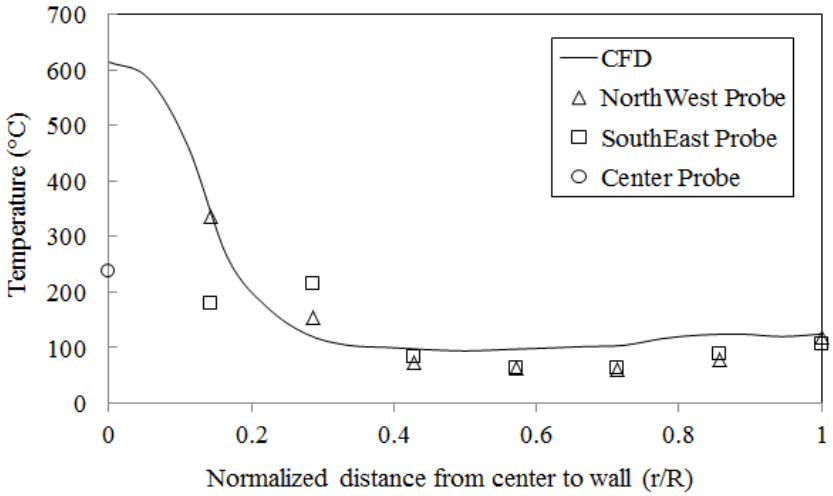

(b) August 25th data

Figure 24 Validation of the top gas temperature distribution

The averaged top gas comparison is listed in Table 8 and Table 9. As can be seen from the tables, the average top gas from CFD is approximately 35^0C higher than the measured data. The heat escaped through the furnace wall only takes into consideration the heat loss through cooling stave.

Table 8 Top gas comparison for August 23rd data

	Measurement	CFD	Absolute Error	Relative Error
Top Gas Average Temp. (ºC)	119	155	35	29.70%
CO_2 %	22.18	22.20	0.02	0.10%
CO %	23.88	24.02	0.14	0.58%
H_2 %	6.33	6.09	0.24	3.73%
N_2 %	47.62	47.70	0.07	0.16%
CO Gas Utilization	48.15	48.03	0.12	0.25%
H_2 Gas Utilization	50.40*	50.51	0.11	0.22%
Pressure Drop (Pa)	150000	153138.7	3139	2.09%
Coke Rate (lb/NTHM)	823	855	32	3.89%

Table 9 Top gas comparison for August 25th data

	Measurement	CFD	Absolute Error	Relative Error
Top Gas Average Temp. (ºC)	128	162	34	26.34%
CO_2 %	22.12	21.63	0.49	2.21%
CO %	23.65	23.49	0.16	0.68%
H_2 %	6.17	6.38	0.21	3.35%
N_2 %	48.05	48.49	0.44	0.92%
CO Gas Utilization	48.33	47.94	0.39	0.81%
H_2 Gas Utilization*	51.20*	50.19	1.01	1.97%
Pressure Drop (Pa)	132000	142176	10176	7.71%
Coke Rate (lb/NTHM)	870	840	30	3.45%

* Calculated from measured top H_2 and tuyere conditions

3.6 Applications of Burden Distribution Model

3.6.1 Convergence of the Stock-line Profile

With an assumed initial stock-line profile, an iterative procedure needs to be carried out to obtain the final stock-line profile. Figure 25 illustrates the charging history under the same ring configuration. It can be seen that the stock-line profile will reach a steady shape after about five iterations. The detailed convergence history of the stock-line profile is shown in Figure 26. It demonstrated that good convergence was achieved by the current algorithm.

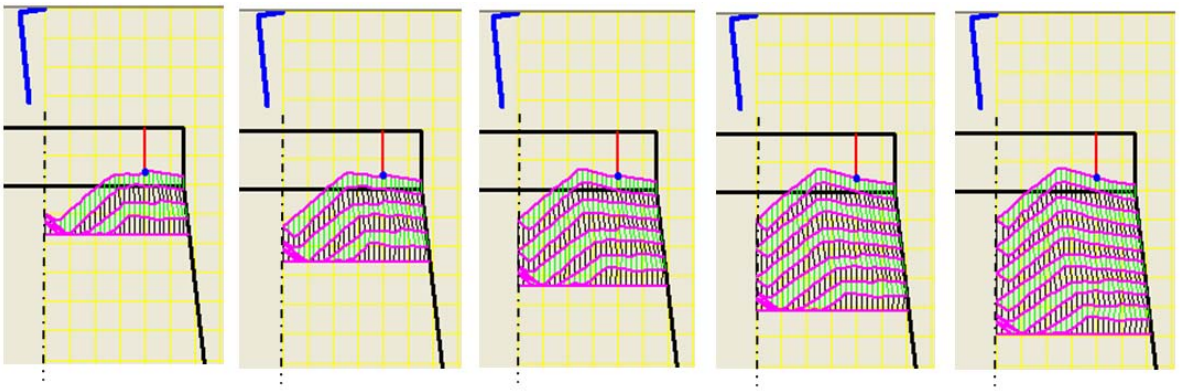

1st iteration 2nd iteration 3rd iteration 4th iteration 5th iteration

Figure 25 Evolution of stock-line profile

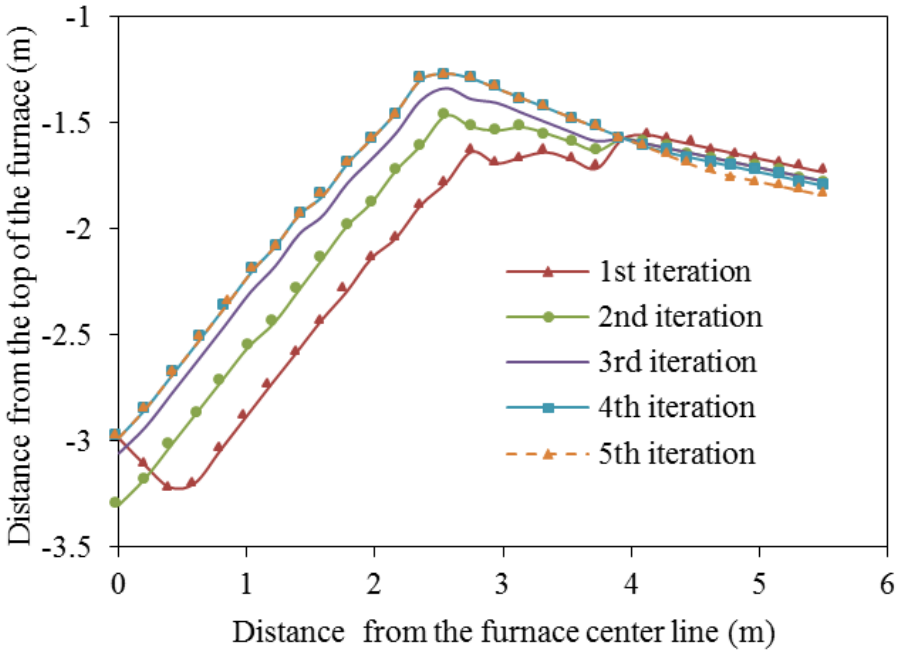

Figure 26 Detailed evolution of stock-line profile

Figure 27 shows that the final stock-line profile is independent of the initially assumed profile. Under all three different initial conditions, the stock-line profile converges within four to five iterations.

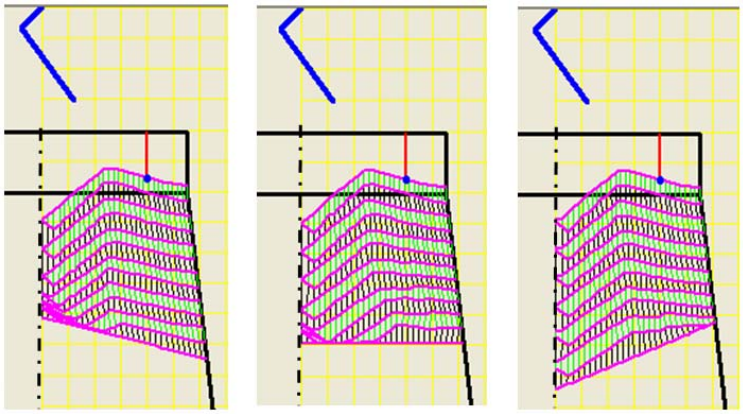

Figure 27 Converged Stock-line profiles for different initial condition

3.6.2 Parametric Study of Burden Distribution Model

The impact point at the stock-line level is essential for the burden profile. The effects of chute parameters, including chute jointing distance, chute length and chute rotational speed, on the impact point have been investigated. Figure 28 (a) shows the schematic of different chute jointing distance (S). As can be observed in Figure 28(b), the impact point moves to the center of the furnace as S increases, and the rate of such increase is independent of the chute inclination angle because the two lines are parallel to each other.

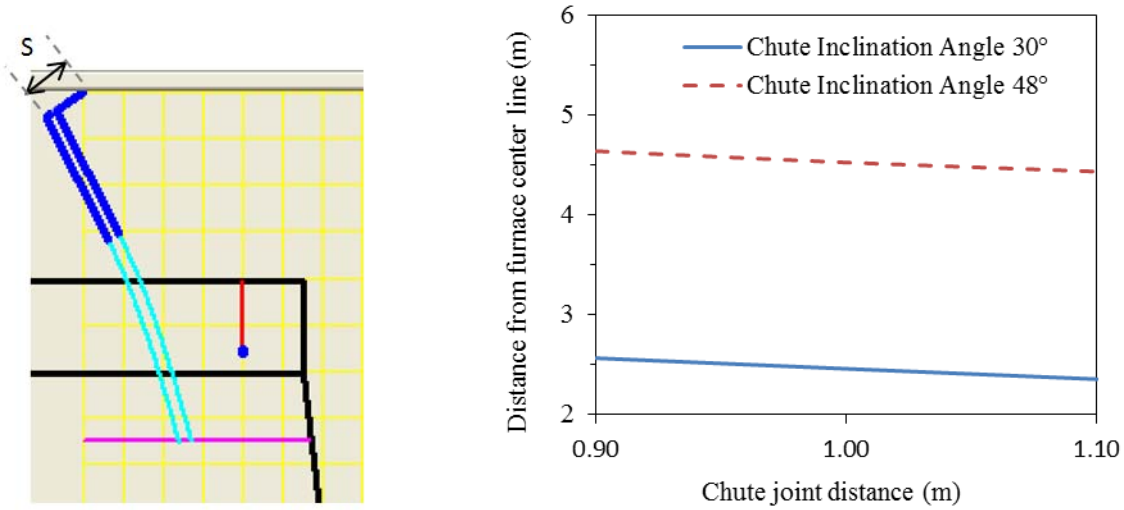

(a) (b)

Figure 28 Effects of chute joint distance on the stock-line impact location

In Figure 29(a), the effects of chute length on the impact point can be observed. For relatively small chute inclination angle (i.e. 30 °), the impact point is slightly increased by extending the

chute length. However, the effects of chute length become obvious for the bigger chute inclination angle case (i.e. 48 °).

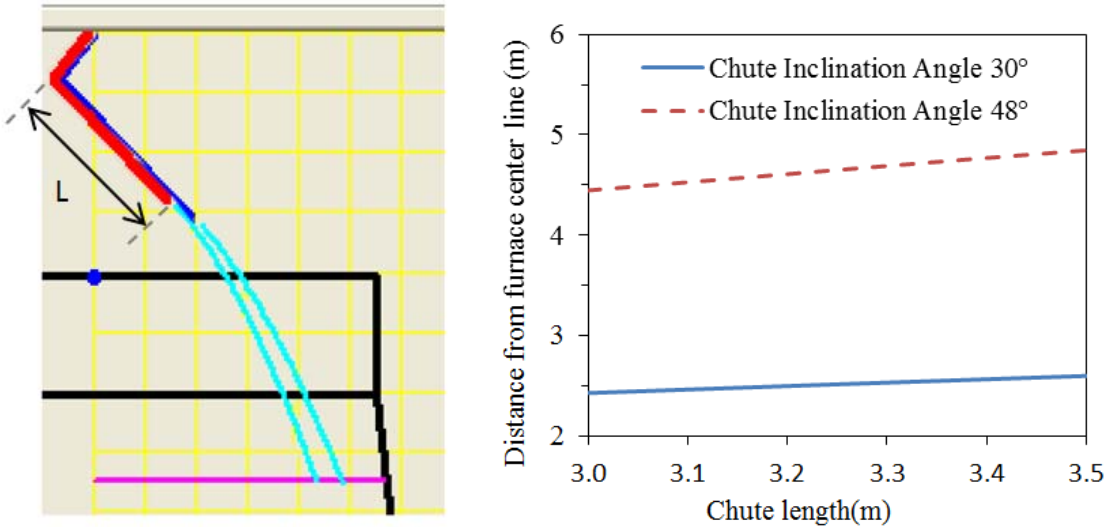

(a) (b)

Figure 29 Effects of chute length on the stock-line impact location

Figure 30 shows the effects of chute rotational speed on the impact point. The effects are appreciable only in large chute inclination angle case (i.e. 48 °) with the chute rotational speed changing from 0 to 0.2 rad. /s.

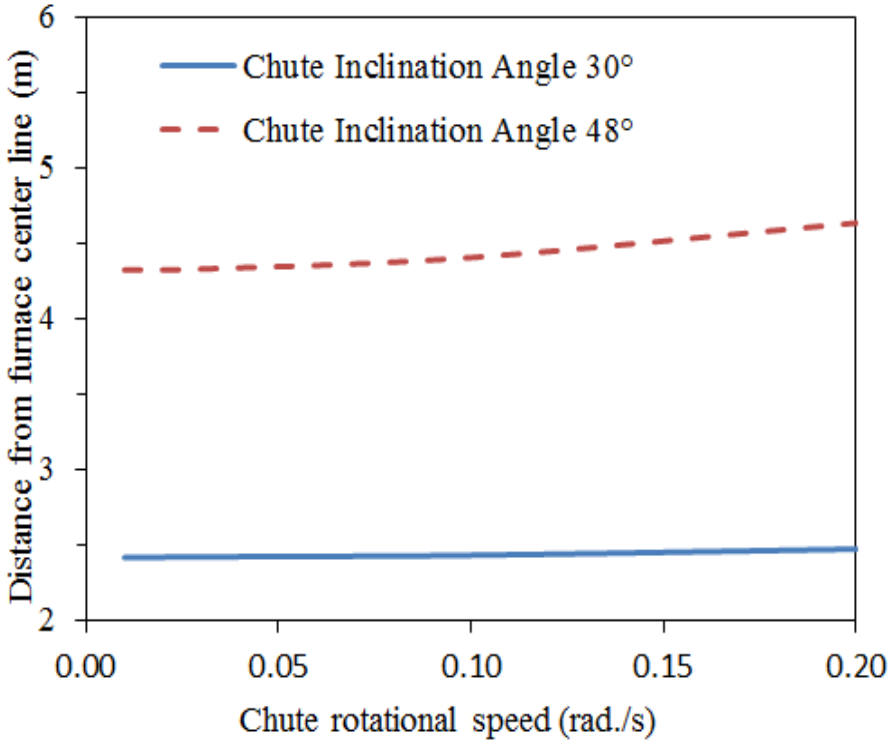

Figure 30 Effects of chute rotational speed on the stock-line impact location

The burden profile will be significantly affected by the shaft angle of the furnace. The volume of each charge is the same for the two cases in:

Figure 31 (a). The layer will be thinner as the shaft angle decreases because of the enlargement of furnace inner volume. As shown in

Figure 32 (b), both the inclination angle of each layer and the layer thickness reduce with burden descent. The rate of change of inclination angle decreases with the increase of the shaft angle.

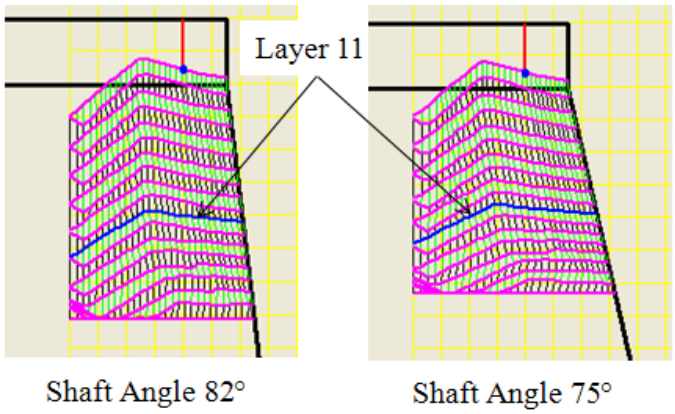

(a) Overview of geometry with different shaft angle

Figure 31 Effects of shaft angle on the burden profile

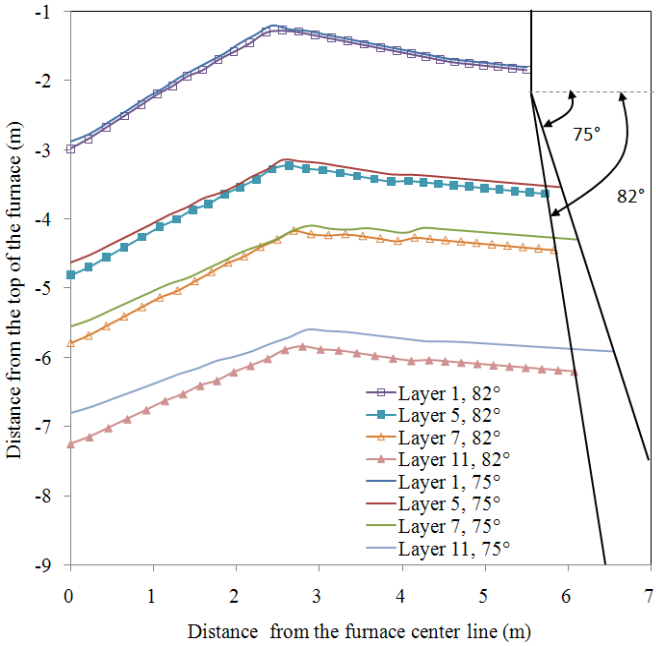

(b) Detail burden profile

Figure 32 Effects of shaft angle on the burden profile

3.7 Application of the CFD Model to Actual Blast Furnaces

3.7.1 Baseline Case

3.7.1.1 Months Averaged Operation Data

The baseline case used geometry from an industrial blast furnace. Operating data is listed in Table 10. It should be noted that the flux rate only includes the dolomite and limestone charge. Other charging items such as Basic Oxygen Furnace (BOF) slag are classified as the ore rate. The diameters of coke and iron ore are taken as the averaged value from the actual size distribution.

Table 10 Three months averaged operation data (continued next page)

Productivity(NTHM/day)	5500
Coke rate(lb/NTHM)	751
PCI rate(lb/NTHM)	207
Ore rate(lb/NTHM)	3156
Flux rate(lb/NTHM)*	162

Porosity of coke layer(-)	0.50
Porosity of ore layer(-)	0.34
Porosity of coke particles(-)	0.45
Porosity of ore particles(-)	0.20
Diameter of coke particles (mm)	50.4
Diameter of ore particles (mm)	11.8
Top absolute pressure (Pa)	2.04×10^5

*Only include dolomite and limestone

Figure 33 shows the visualization of the burden distribution applied for the baseline simulation. Figure 33 (a) is the burden structure provided by the U.S. Steel simulation model [Zhao et, al. 2010] and the O/C distribution at the stock-line is taken as an input for the burden descending model aforementioned to generate the burden in the entire shaft region. The final burden structure used in the simulation is shown in Figure 33 (a) and Figure 33 (b).

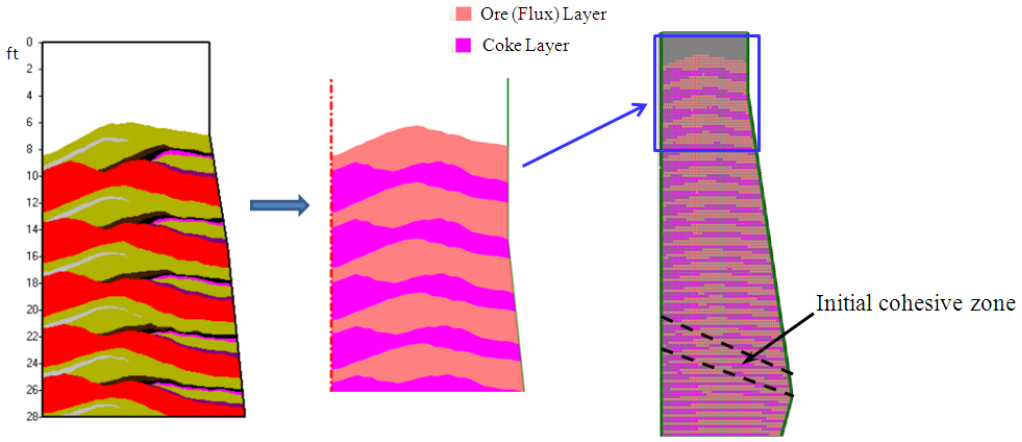

Figure 33 Burden distribution

Figure 34 shows the stock-line O/C distribution and it is used as boundary condition for the lump particles, i.e., coke, ore, and flux at the top burden surface. The stock-line ore profile is presented in Figure 34 (a) and the stock-line flux (dolomite and limestone) profile is assumed to be proportional to the ore profile as demonstrated in Figure 34 (b). As can be seen in these figures, coke was mostly charged in the central region of the blast furnace and ore in the peripheral region.

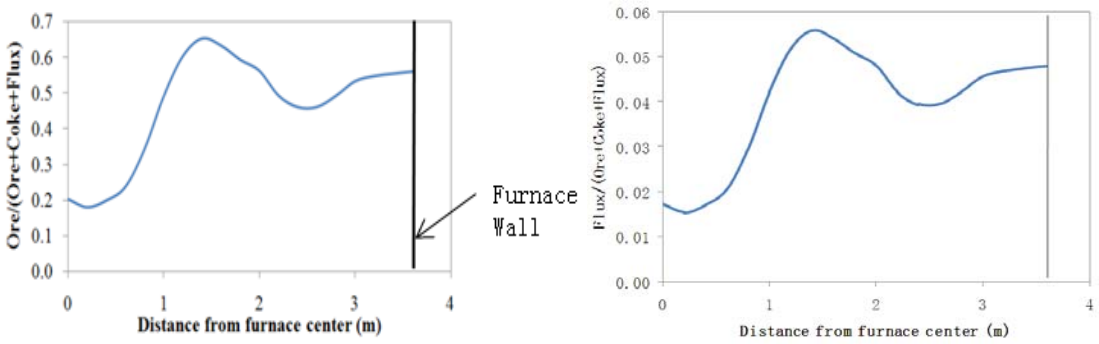

(a) (b)

Figure 34 Stock-line ore profile and flux profile

In Figure 35, the predicted burden temperature distribution and CO concentration are shown. The furnace is equipped with twenty-four tuyeres, but the computational domain with a single tuyere is used for the simulation. The results from raceway simulation were applied at the interface as the inlet condition for the shaft CFD model.

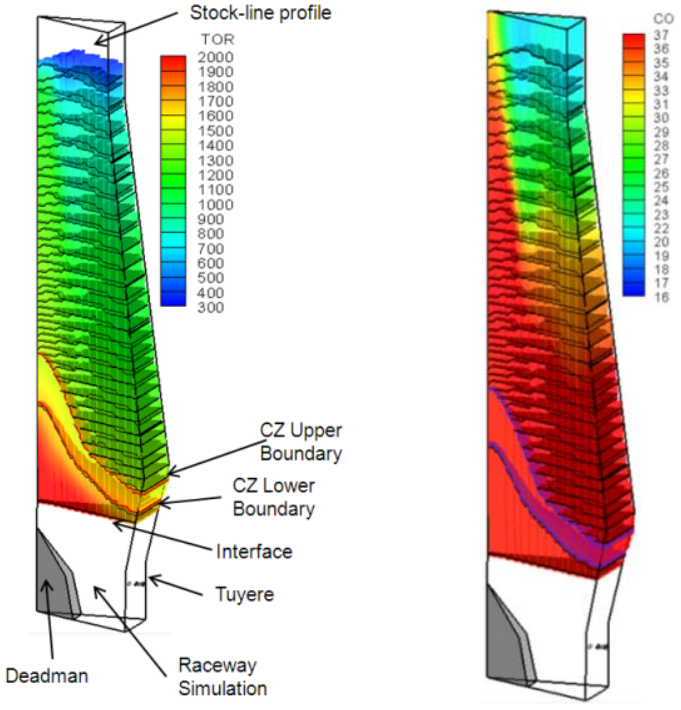

(a) Burden temperature (K) (b) Gas CO (v. %)

Figure 35 Contours of burden temperature and gas composition

The temperature field inside the furnace is shown by the isotherm surfaces of gas and burden in Figure 36. The temperature difference between gas phase and solid phase is significant in the lower part of the furnace. It is also observed that the changing of burden temperature is relatively slow in the middle section of the shaft, forming a “thermal reserve” zone (TRZ).

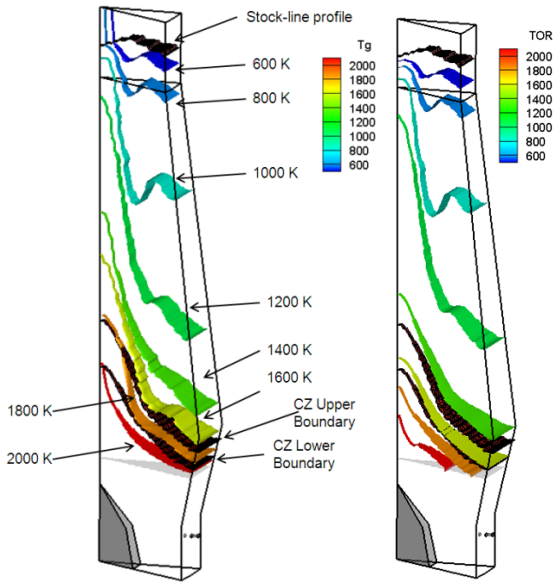

(a) Gas Temperature (K) (b) Burden Temperature (K)

Figure 36 Isotherm surfaces of gas temperature and burden temperature

The distributions of major parameters in the furnace shaft are exhibited in Figure 37 through Figure 41. The distribution of CO volume fraction in Figure 37 (a) has been combined with the raceway simulation results to present an overview of the entire furnace condition. There are eight isotherm lines ranging from 400 °C to 1100 °C with an interval of 100 °C displayed. The CZ upper boundary is defined by the 1200 °C isotherm line and the CZ lower boundary is determined by the local liquidus temperature described in the cohesive zone sub-model previously. The other contours in the paper will follow the same convention, but the raceway simulation below the interface will be omitted. The vertical axis in all the figures denotes the distance from the tuyere center line. Figure 37 (b) (c) and (d) show the distribution of CO_2 volume fraction, gas temperature and the burden temperature, respectively.

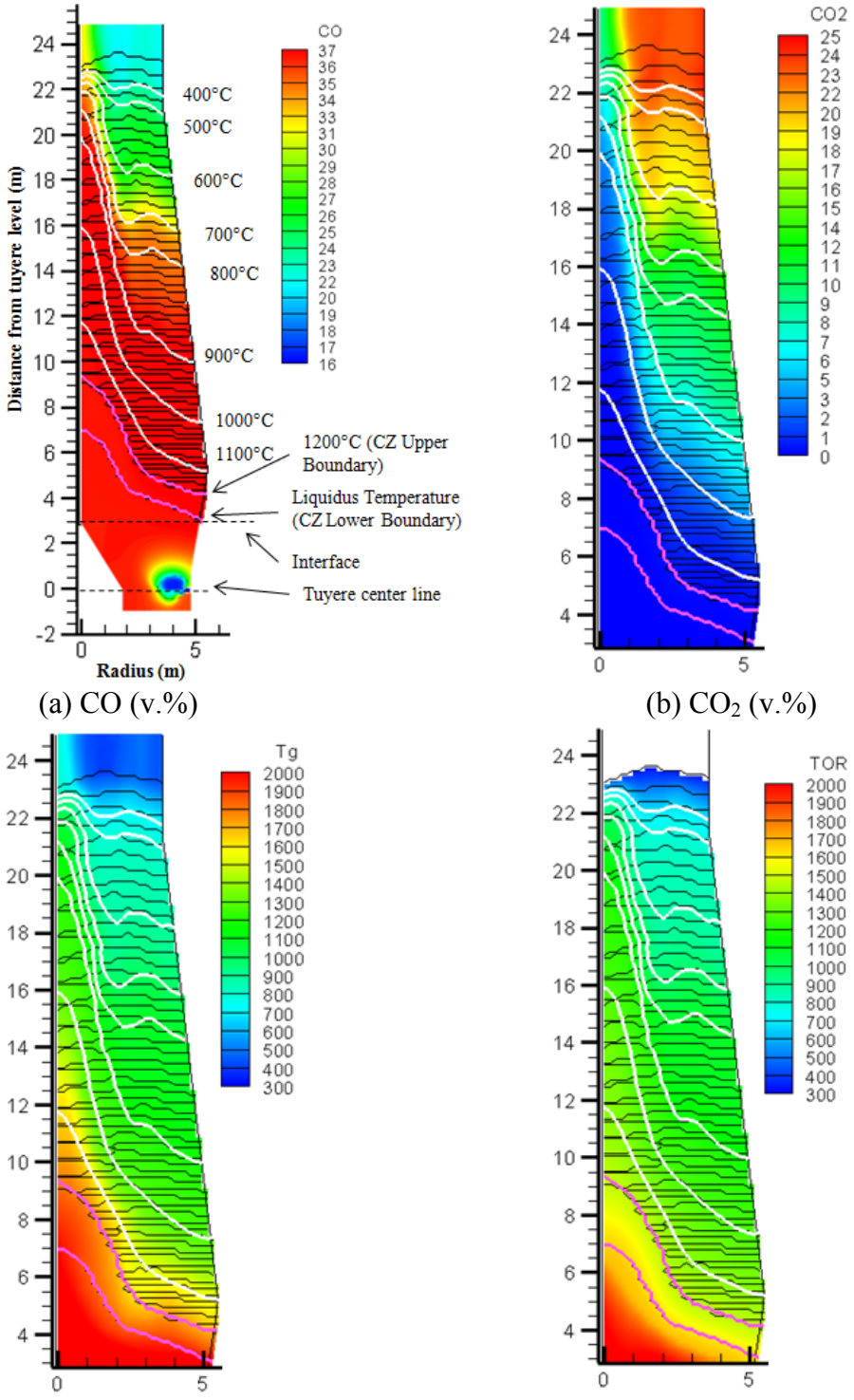

(a) CO (v.%) (b) CO_2 (v.%)

(c) Gas temperature (K) (d) Burden temperature (K)

Figure 37 Gas species and temperature distribution

Figure 39 manifests the gas flow characteristics inside the furnace. Figure 39 (a) shows the gas velocity vector colored by gas temperature. In the streamline in Figure 39 (b), which has a background colored by the porosity, the CZ possesses a much lower porosity due to the fusion of

the iron ore burden. The zigzag flow pattern is observed because of the difference in porosity of the coke and ore layer. The highest pressure drop exists in the CZ region as shown in Figure 39 (a). The distribution of mass flux in the vertical direction is shown in Figure 39 (b). Below the CZ, higher mass flux rate is concentrated in the center of the furnace since more coke is charged in the furnace center. The mass flux in the top of the furnace above the stock-line shows a strong uneven distribution in the radial direction. A low velocity zone is found in the middle radius because this is the location with the highest ore fraction based on the burden arrangement.

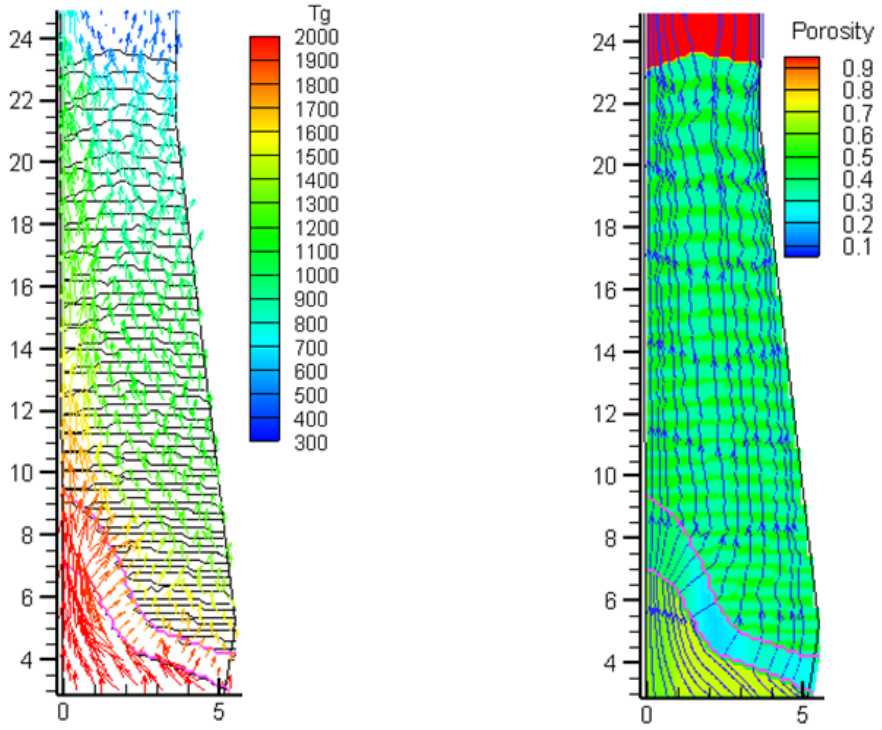

(a) Gas vector (b) Streamline

Figure 38 Gas flow characteristics

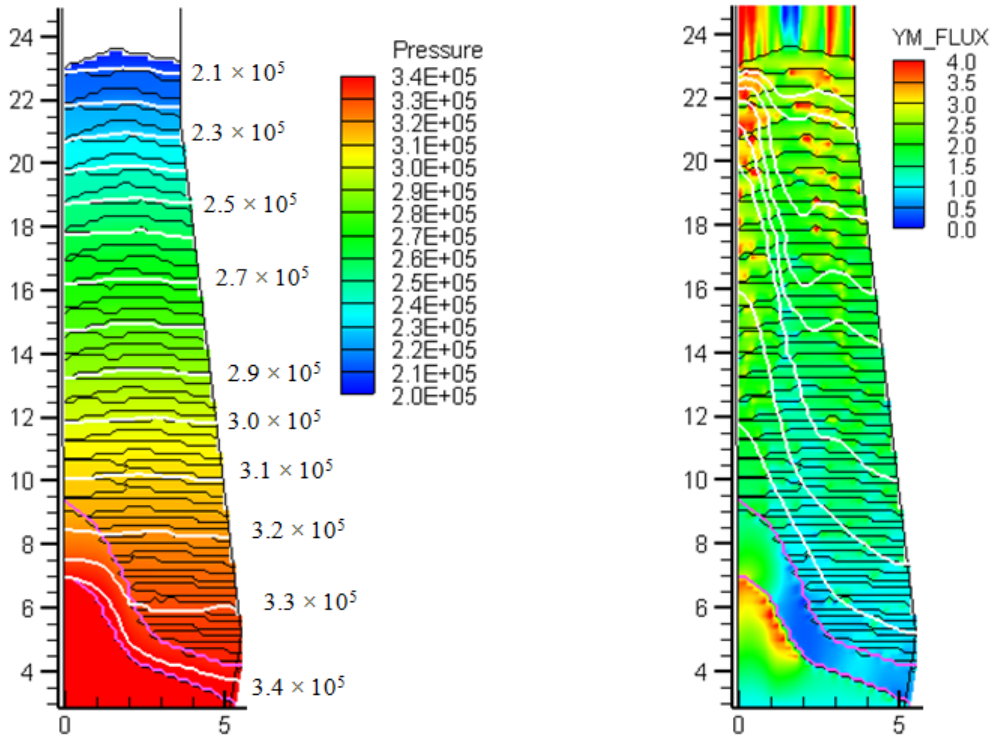

(a) Gas pressure (Pa)

(b) Gas vertical mass flux (kg/m^2)

Figure 39 Gas flow characteristics

The burden species are shown in Figure 40 and the corresponding gas-solid reaction rates are exhibited in Figure 41 for the reaction equations (2), (3), (4) and (8).

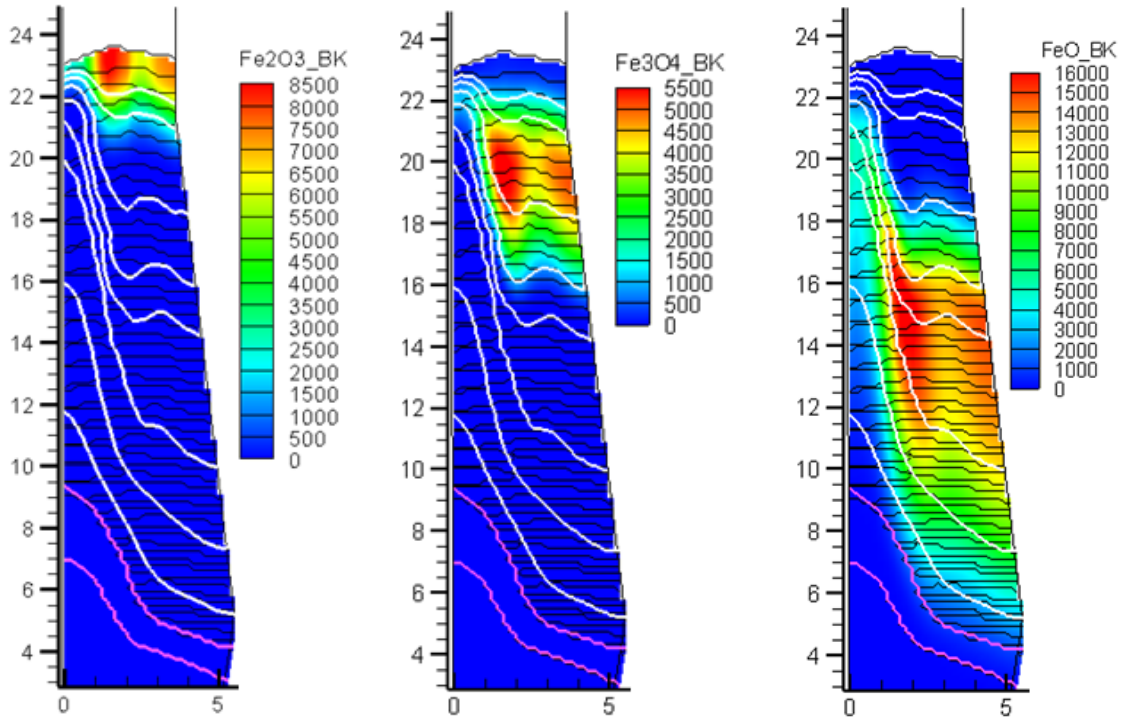

(a)Fe2O3 (mol/m^3) (b) Fe3O4 (mol/m^3) (c) FeO (mol/m^3)

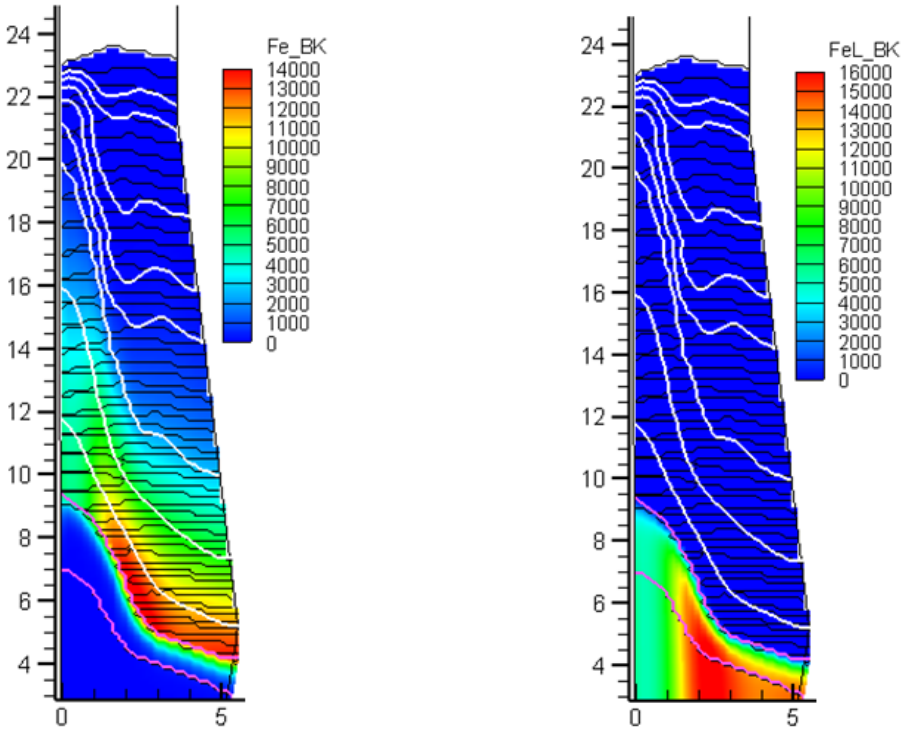

(d) Fe (mol/m^3) (e) Liquid Fe (mol/m^3)

Figure 40 Burden species distribution

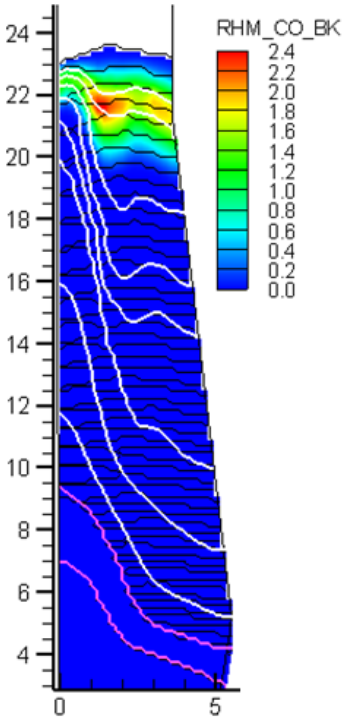

(a) H-M (mol/(s.m^3))

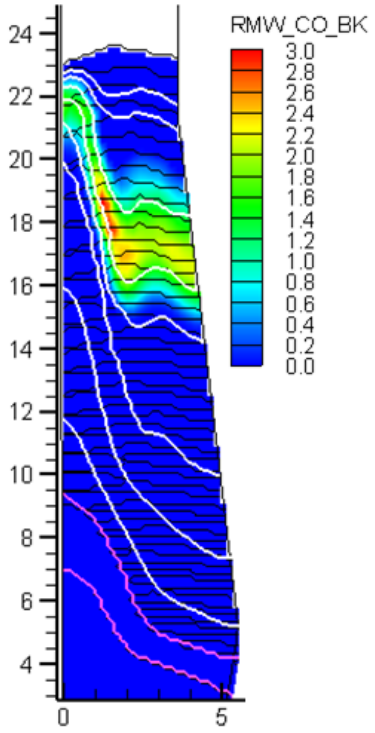

(b) M-W (mol/(s.m^3))

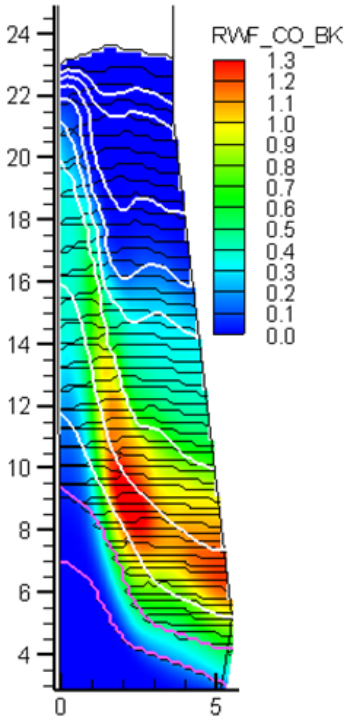

(c) W-F (mol/(s.m^3))

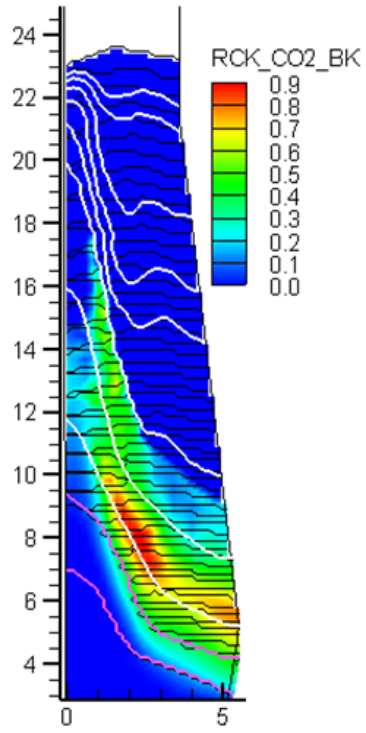

(d) Coke gasification (mol/(s.m^3))

Figure 41 Rate distribution of chemical reactions

The coke gasification by CO_2 virtually halts at elevations above the 900 °C isotherm as displayed in Figure 41 (d). All reduction above the 900 °C isotherm is carried out by CO generated below the isotherm. As the height rises, this CO sequentially reduces FeO to Fe; Fe_3O_4 to FeO, and Fe_2O_3 to Fe_3O_4. The sequence of such reactions favors the reduction of more wustite (FeO) from higher oxides than is reduced to metallic iron by the same amount of gas. It results in the creation of the chemical reserve zone in a certain height in the shaft, as shown in Figure 40 (c), from the 800 °C isotherm to 900 °C isotherm, where the iron-bearing material is virtually all wustite and a zone in which gas and solid compositions changes only slowly is present. The gas composition along the vertical direction of the shaft is plotted in Figure 42 (b) and the three locations are shown in Figure 42 (a), i.e., 0.90R is the location close to the furnace side wall and 0.04R is the center. It can be found that the gas composition has approached that for FeO/Fe equilibrium (70% CO, 30% CO_2) in the isotherm ranging from 700 °C to 900 °C in the periphery of the furnace to the middle (0.47R).However, in the center of the furnace (0.04R), the gas composition is far from FeO/Fe equilibrium because of the center coke charging.

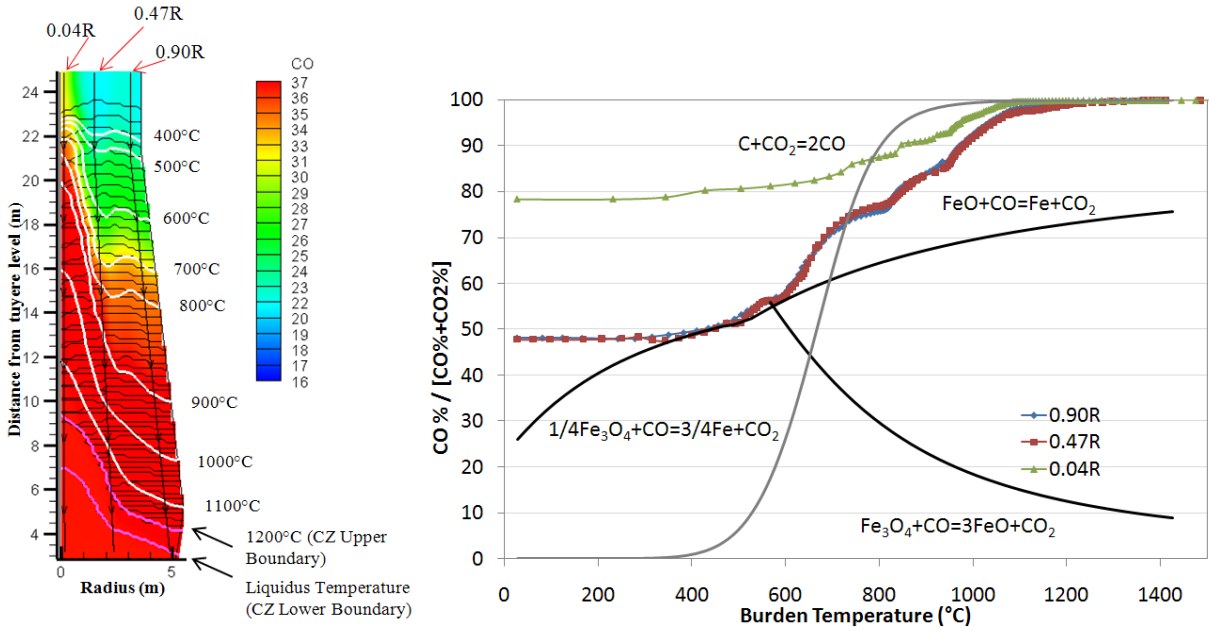

(a) Location of the vertical line (b) Gas distribution

Figure 42 Gas composition distribution along the shaft

The heat transfer characteristics can be observed in Figure 43 (a). The heat transfer between the gas and burden is intense in the lower part of the shaft. A large temperature gradient between the gas and burden is found below the 1000 °C isotherm, which is due to the highly endothermic coke gasification reaction and the high temperature bosh gas. As the gas continues its ascent above the 900 °C isotherm, the CO continues to react with wustite to form solid Fe and CO_2. The

reaction given by Eq. (4) is slightly exothermic and as a result the gases do not cool during their ascent through this region. This forms the "thermal reserve" zone of the furnace. The corresponding gas composition is also relatively constant as shown in Figure 43 (b). At the top of the furnace, the preheating zone exists due to the cold charging of the raw material and water evaporation, where the temperature difference between the burden and gas is about 100 °C.

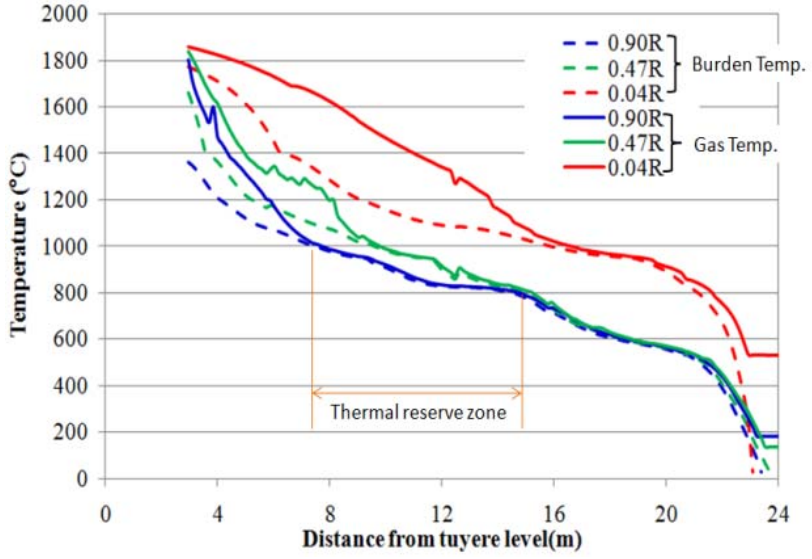

(a) Gas and burden temperature

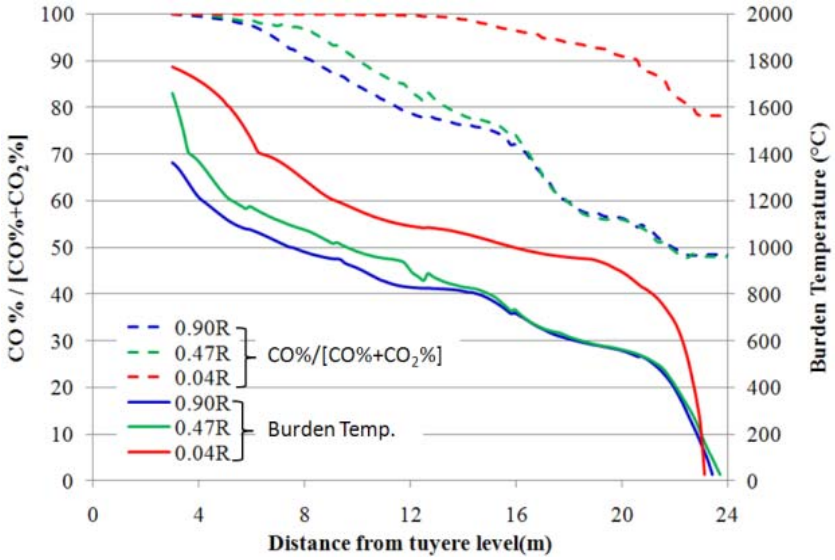

(b) Gas composition and temperature distribution

Figure 43 Gas composition and temperature distribution along the shaft

Figure 44 shows the top gas distribution including the temperature and composition. Low gas utilization and high temperature is observed in the furnace center.

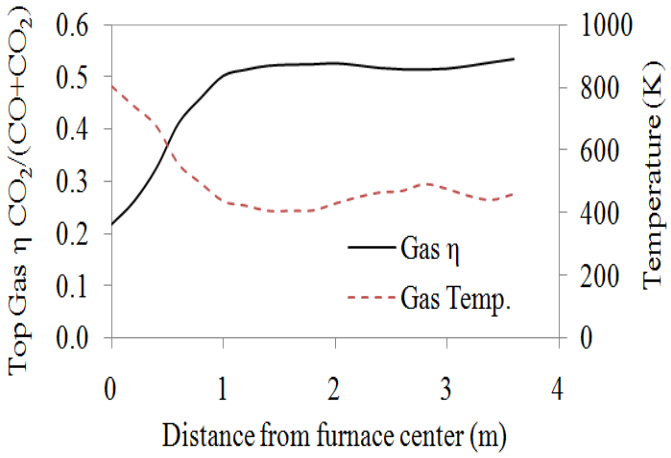

(a) Temperature and utilization

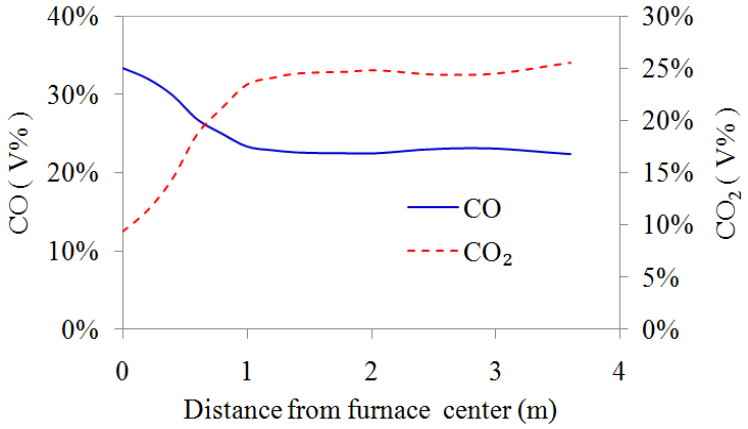

(b) Composition

Figure 44 Top gas distribution

The mass fraction of FeO is presented in Figure 45 (a). As the reduction of wustite is taking place just above the CZ, a large concentration gradient is observed in the region of the upper boundary of the CZ (1200 °C isotherm), resulting in virtually no FeO in the lower boundary of the CZ. Figure 45 (b) shows the local basicity (CaO wt. % / SiO_2 wt. %). Due to the coke gasification, the SiO_2 goes to the slag phase, decreasing the basicity. Assuming that the slag melts below the upper boundary of the CZ, the basicity above the CZ denotes the ratio of CaO to SiO2 in the solid burden.

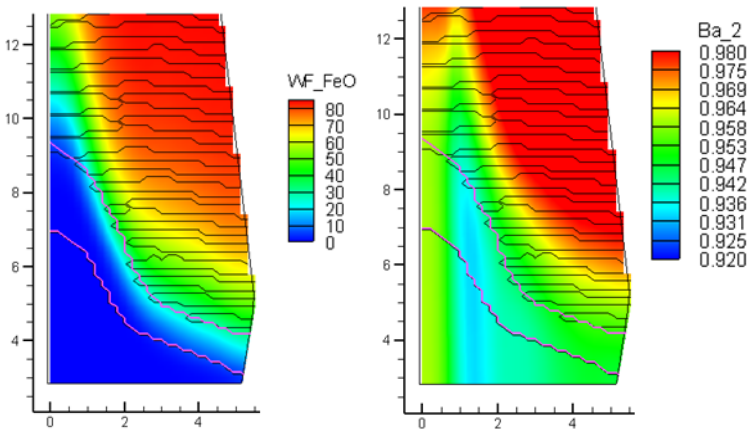

(a) FeO wt.% (b) Basicity

Figure 45 Contour of slag composition in the CZ

Figure 46 shows the weight percentage of FeO in the lower, middle and upper boundaries of the CZ. The peak point is at 0.37 radius position, which corresponds to the stock-line charging profile as shown in Figure 47. In addition, the FeO weight percentage is below 10% in the CZ lower boundary, and the high FeO region is near the furnace wall below the CZ.

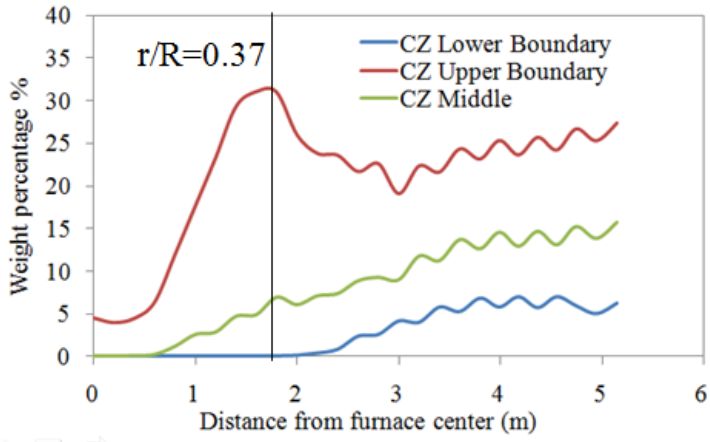

FeO wt.%

Figure 46 FeO distribution

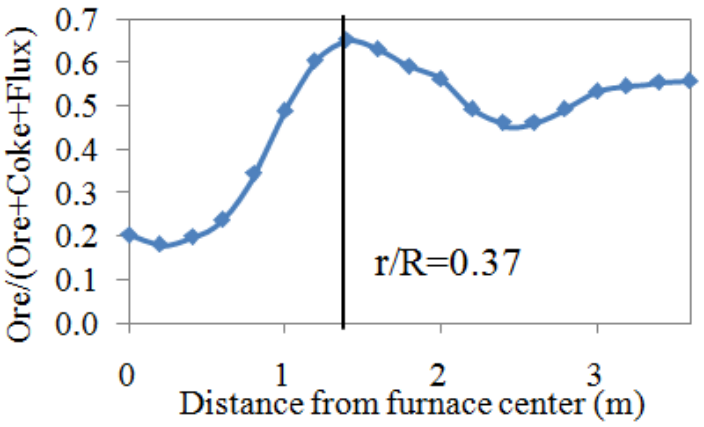

Stock-line ore volume fraction

Figure 47 FeO distribution

Figure 48 (a) shows all of the slag composition in the lower boundary of the CZ. The liquidus temperature is determined by this composition via Eq. (23) and Eq. (24). Since uneven distribution is presented in the radial direction, the lower boundary temperature is not a constant as demonstrated in Figure 48 (b).

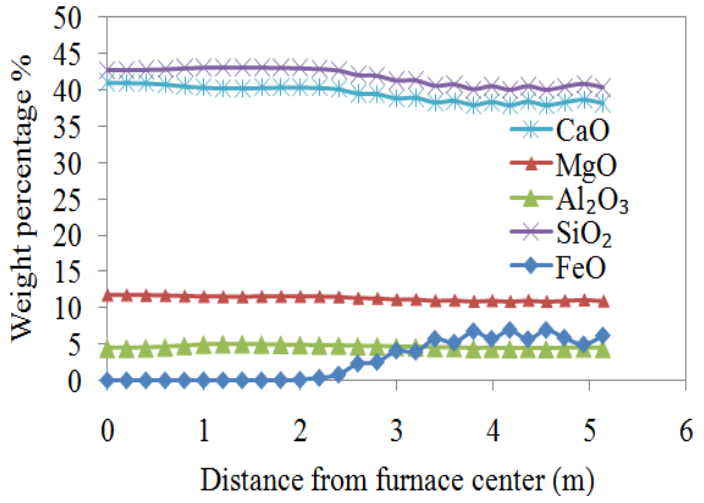

(a) Slag composition in the lower boundary of the CZ wt.%

Figure 48 Slag composition and temperature distribution of the CZ

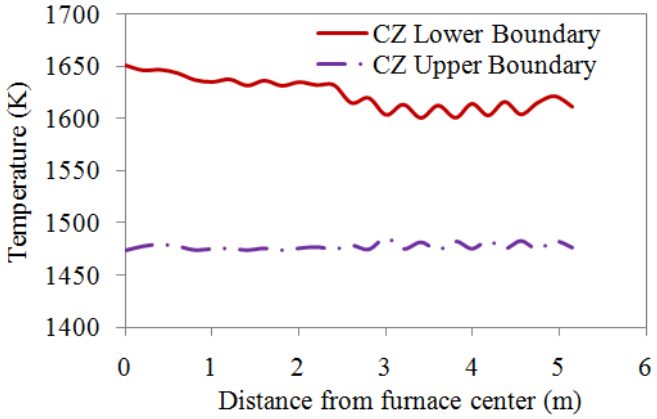

(b) Temperature distribution

Figure 48 Slag composition and temperature distribution of the CZ

3.7.1.2 Single Day Operation Data

The operation data listed in Table 11 is from an industrial blast furnaces. Two days of stable operational periods were selected to validate the shaft CFD model.

Table 11 Two days operation data

	August 23th 2010	August 25th 2010	Unit
Hot metal production rate	5505	5137	NTHM/day
Coke rate (dry)	823	870	lb/NTHM
Flux* rate (dry)	224	224	lb/NTHM
Coal injection rate	15.3	14.9	NT/hr
Natural gas injection rate	6378	6492	scfm
Ambient wind Rate	135341	131293	scfm
Oxygen enrichment rate	9404	7626	scfm
Tuyere added moisture rate	18	18	gr/scf
Furnace wall heat loss	2.41×10^5	2.41×10^5	Kcal/min
Top absolute pressure	2.04×10^5	2.04×10^5	Pa
*Flux includes limestone and dolomite			

The permeability of different types of layers in the blast furnace differs significantly. The utilized layer properties for the simulation are shown in Table 12. The permeability index defined in Eq. (66) is an indicator for the relative resistance to gas flow at different bed condition. Table 13 listed the corresponding permeability index in the simulation. It can be seen that the coke layer is almost 8 times more permeable than the ore layer. The melted iron ore layer in the CZ has extremely low permeability.

$$K = \frac{\rho v^2}{\Delta P/L} = 0.57(\frac{\emptyset d \varepsilon^3}{1-\varepsilon}) \quad 66$$

Table 12 Layer properties

Porosity of coke layer(-)	0.45
Porosity of ore layer(-)	0.38
Porosity of ore layer in CZ (-)	0.10
Porosity in dripping zone (-)	0.35
Coke shape factor (-)	0.8
Ore shape factor (-)	0.8
Diameter of coke particles (mm)	50.4
Diameter of ore particles (mm)	11.8

Table 13 Permeability index

	Porosity, ε	Permeability Index,K (mm)
Coke layer	0.45	3.81
Ore layer	0.38	0.48
Ore layer in CZ	0.10	0.01
Dripping zone	0.35	1.52

Figure 49 shows the top profile used for simulation for both days. A center coke chimney is formed for this specific charge condition.

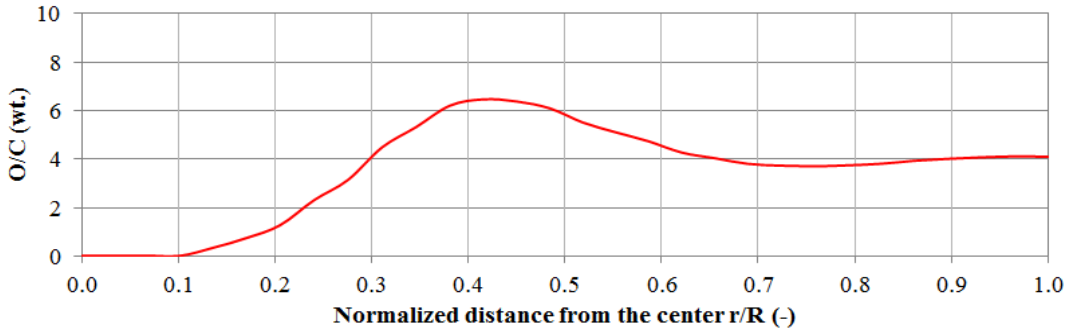

Figure 49 Top burden layer O/C ratio

Since the two days operation is similar, only the results of August 23rd are presented in this section. The total grid number for the simulation is 162,816 as partially shown in Figure 50 (a). A quarter of the furnace is simulated. The coke burden structure colored by burden temperature is shown in Figure 50 (b) while the ore layer has been made transparent except the melted ore inside CZ. The stock line profile is revolved to form a surface. The 3-D CZ shape with the vertical velocity distribution on several cross-sections is shown in Figure 50 (c). The center gas velocity is high due to the center coke chimney.

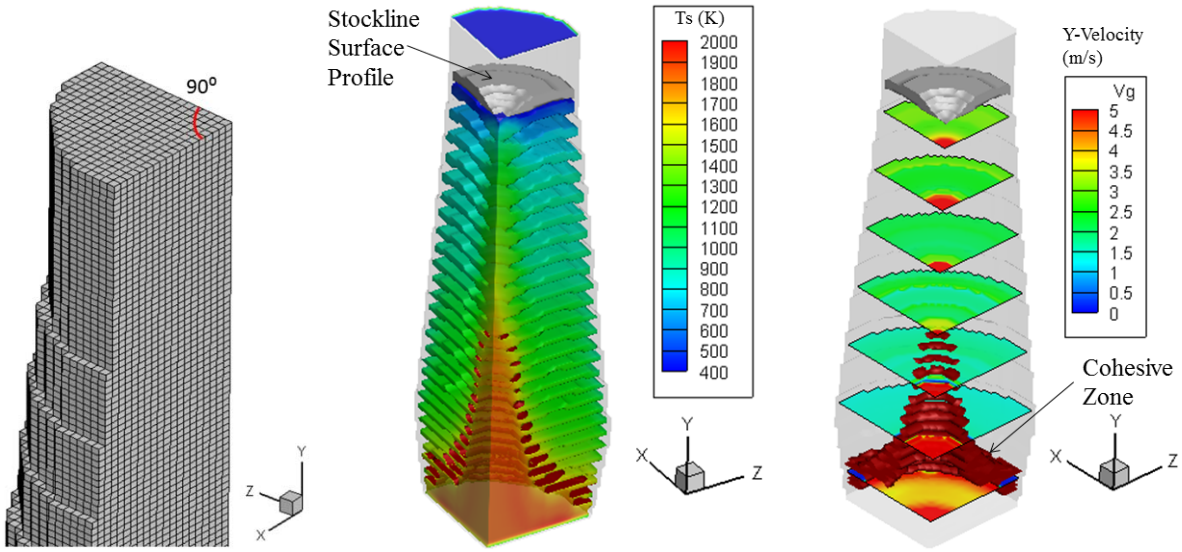

(a) Computational grid (b) 3D Burden (c) Gas vertical superficial velocity

Figure 50 3-D shaft simulation

The CZ has significant effects on the gas flow. For the specific operation, there are approximately 10 ore layers inside the CZ as shown in Figure 51 (a). The corresponding porosity distribution is exhibited in Figure 51 (b). The melted ore has a porosity of 0.1 and it is observed that the ore layers become virtually impermeable within the CZ thus forcing the ascending gas to pass through the coke slits present between the ore-layers.

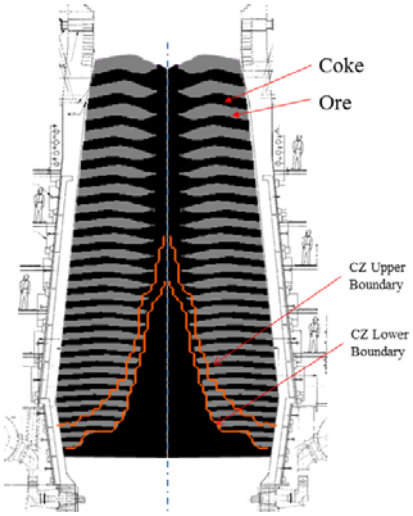

(a) CZ structure

Figure 51

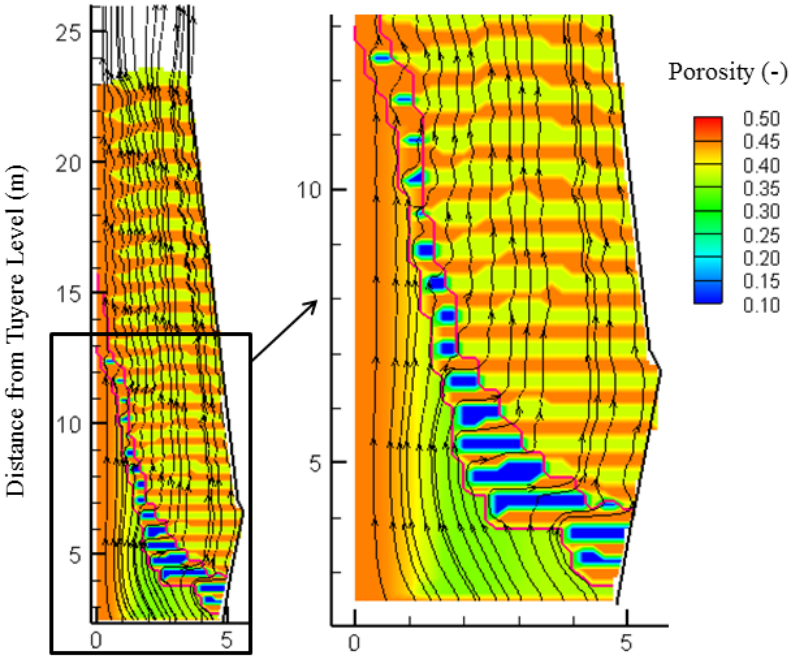

(b) Porosity distribution

Figure 51 Cohesive Zone

Due to the circular symmetry of the results, the cross-sectional view is presented to show the distribution. The gas superficial velocity distribution in the whole shaft is shown in Figure 52 (a). The vertical movement of predominates in the shaft as displayed in Figure 52 (b). However, Figure 52 (c) shows that inside the CZ, the horizontal gas flow is obvious and it is important to maintain good permeability in the coke layer since it is the only path for the reducing gas to support the reaction which takes place above the CZ. Figure 52 (d) shows the pressure distribution and large pressure drop is observed in the dripping zone and across the CZ.

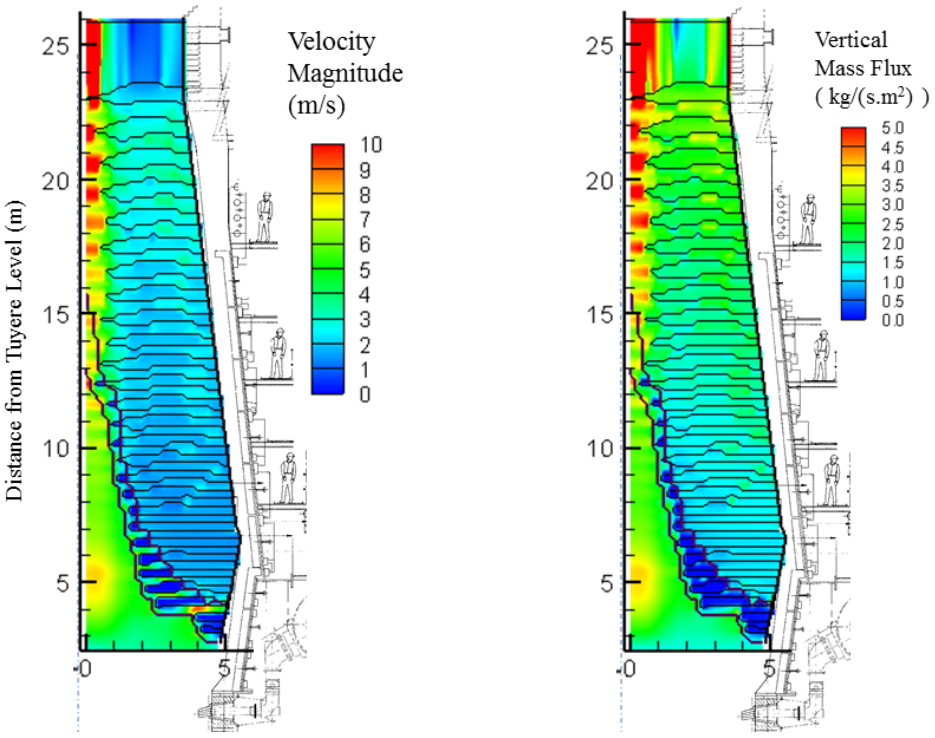

(a) Gas velocity (b) Vertical Flux

Figure 52 Gas flow characteristics

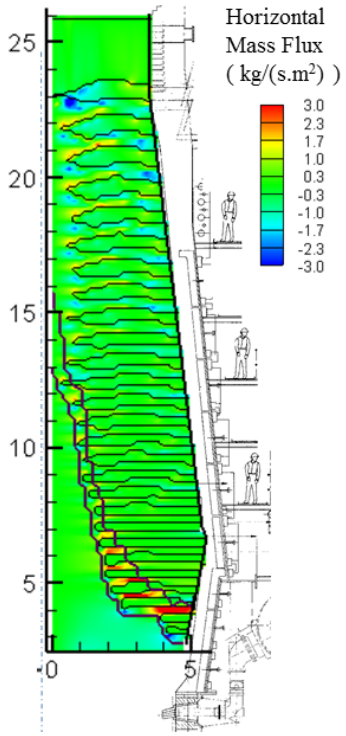

(c) Horizontal Flux

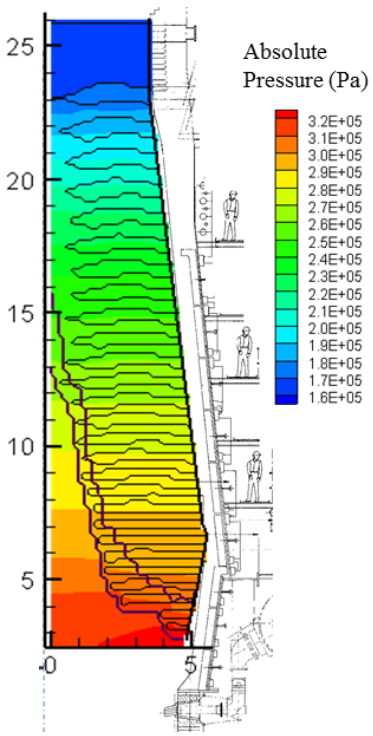

(d) Pressure

Figure 52 Gas flow characteristics

Figure 53 shows the stepwise reduction process of the iron oxides to hot metal. The isothermal line of the burden temperature presented ranges from 400 ^{0}C to 1200 ^{0}C (CZ upper boundary) with an interval of 100 ^{0}C. The CZ lower boundary liquidus temperature is found to be approximately the value of 1350 ^{0}C. The reduction of hematite (Fe_2O_3) took place at the upper part of the BF and it is completely transformed into magnetite (Fe_3O_4) above 500 ^{0}C. The wustite (FeO) is starting to generate at 600 ^{0}C and it is not reduced until the 1200 ^{0}C iso-thermal line. Below the CZ, all the wustite has been converted to melted iron.

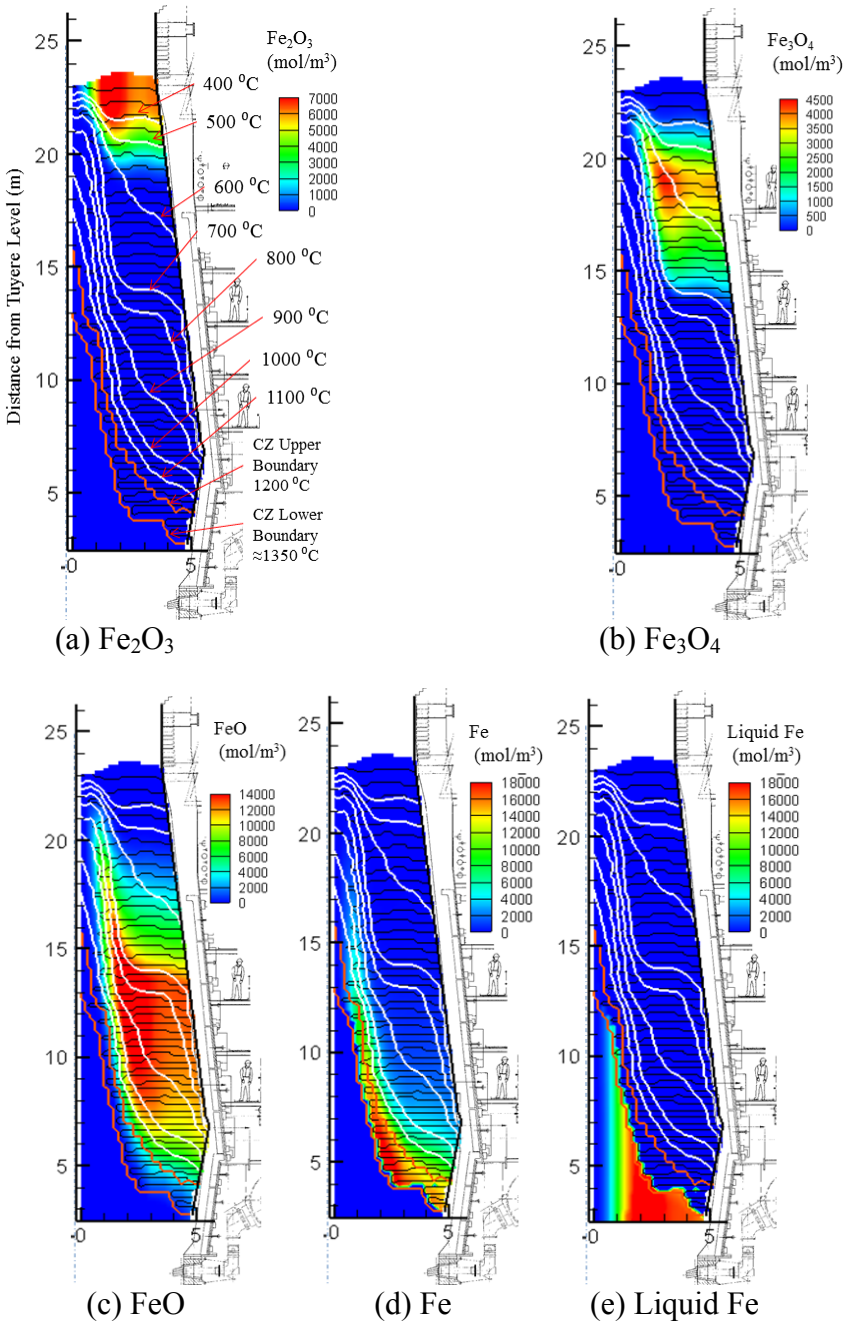

Figure 53 Distributions of burden concentration

The burden temperature iso-lines are shown in Figure 54 (a). The low temperature thermal reserve zone (TRZ) is observed from 600 ^{0}C to 800 ^{0}C and a high temperature TRZ is found to be between 800 ^{0}C to 1000 ^{0}C. The reduction degree increased dramatically from 0.5 to 1.0 beginning at 1100 ^{0}C, and it is associated with significant temperature changes due the endothermic direct reduction. Figure 54 (b) shows the gas temperature and CO volume fraction.

The chemical reserve zone, i.e., the CO volume fraction changes from 30 to 32, corresponds to the high temperature TRZ.

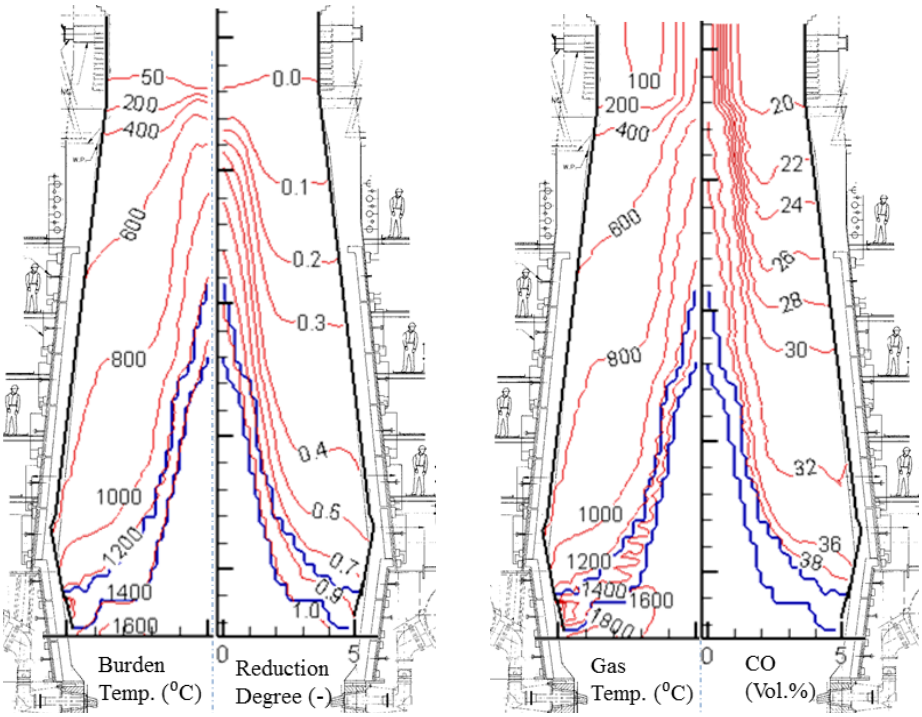

Figure 54 Iso-lines of burden and gas distribution

The plots of the average temperature and gas composition at each cross-section along height of the BF are provided in Figure 55 and Figure 56. The overall CO gas utilization increases rapidly in the temperature range of 1200 ^{0}C to 1000 ^{0}C. Then a zone with relatively constant gas utilization is followed within the temperature range of 1000 ^{0}C to 800 ^{0}C, and it is known as the chemical reserve zone. As shown in Figure 57, radial distribution of CO gas utilization is proportional to the O/C ratio at stock line since more CO_2 is generated at the region where more ore is charged.

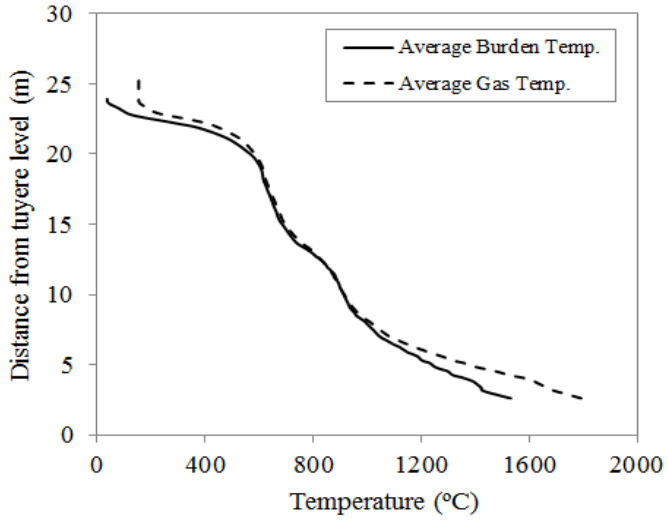

Figure 55 Average gas and burden temperature

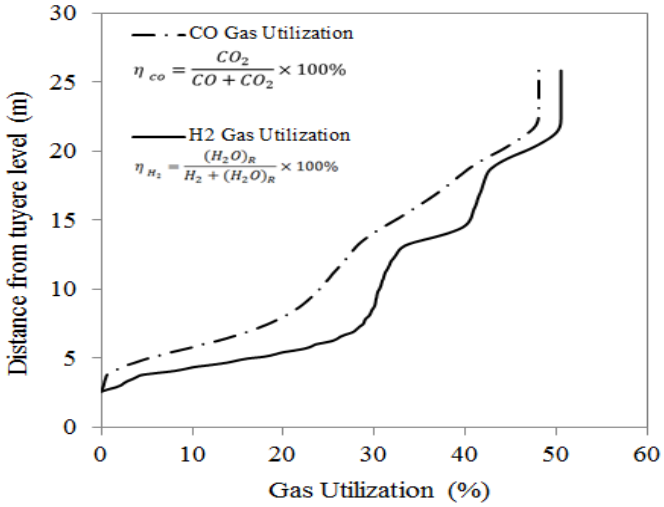

Figure 56 Average gas utilization

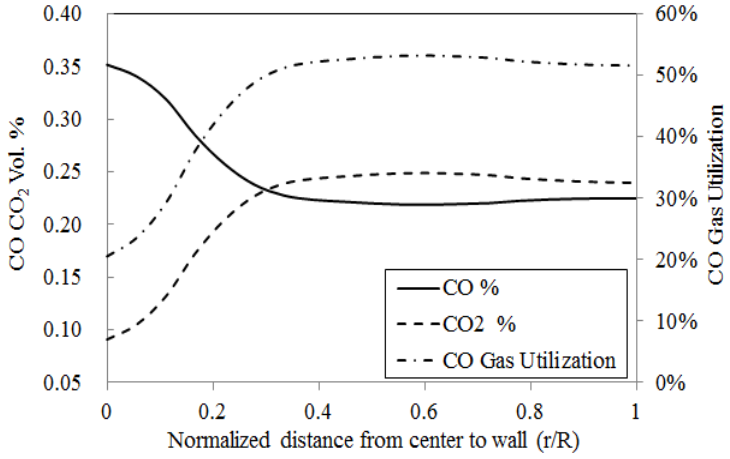

Figure 57 Top gas radial distribution Vertical and radial distribution

3.7.2 Effects of Flux Profile

Since the liquidus temperature of the burden is a function of the slag composition, three cases with different flux profiles are presented. The inlet condition for all three cases maintains the same amount of flux (dolomite and limestone) charged but the radial distribution differs for each case, as shown in Figure 58 (a). The computed CZ shape and CO distribution are provided in Figure 58 (b). It is found that the high flux lowers the CZ due to the increase in basicity.

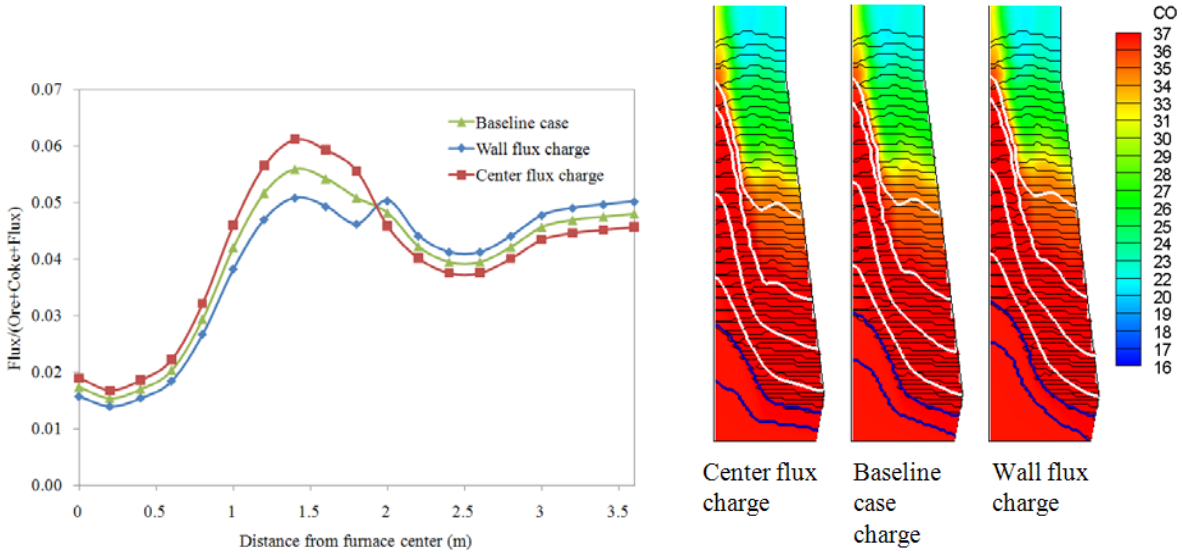

(a) Flux profile at stock-line (b) CZ shape

Figure 58 Effect of flux profile on CZ shape

3.7.3 Effects of Burden Distribution

The inverted "V" shape CZ was observed in the baseline case as shown in Figure 35 and Figure 36. It is due to the center coke charge scheme referred as "center working" furnace in Figure 59. Another "wall working" furnace condition is assumed and the corresponding stock-line ore profile is shown as the red line in Figure 59 where more coke is charged into the wall region of the furnace. All furnace parameters except burden distribution are held constant for the two cases.

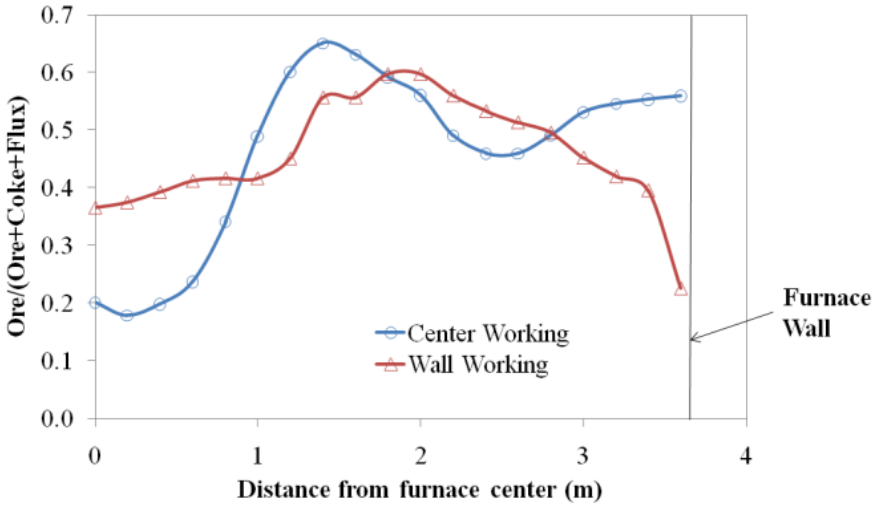

Figure 59 Stock-line ore profiles

Figure 60 shows the distribution of carbon monoxide on the mid-plane of the 3-D domain. The vertical axis of all the figures denotes the distance from the tuyere center line. There are eight isotherm lines of the burden temperature ranging from 400 °C to 1100 °C with an interval of 100 °C displayed. The CZ upper boundary is defined by the 1200 °C isotherm line and the CZ lower boundary is determined by the local liquidus temperature described in the cohesive zone sub-mode. The other contours in the report will follow the same convention.

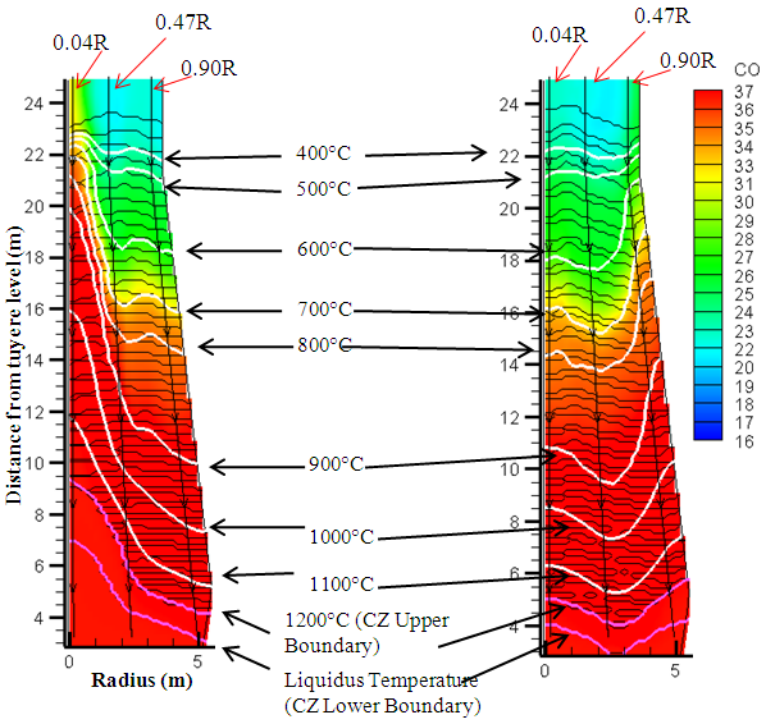

(a) Center working (b) Wall working

Figure 60 Effects of burden distribution on CO volume fraction (v. %)

The gas utilization ($CO_2/(CO+CO_2)$) is a key parameter to evaluate furnace performance. The enhanced central flow in the center working furnace presents an inefficient utilization while the wall working furnace has relatively uniform gas utilization in the radial direction. The gas utilization in both cases corresponds to the local burden temperature which is essential for the chemical reactions as shown in Figure 61.

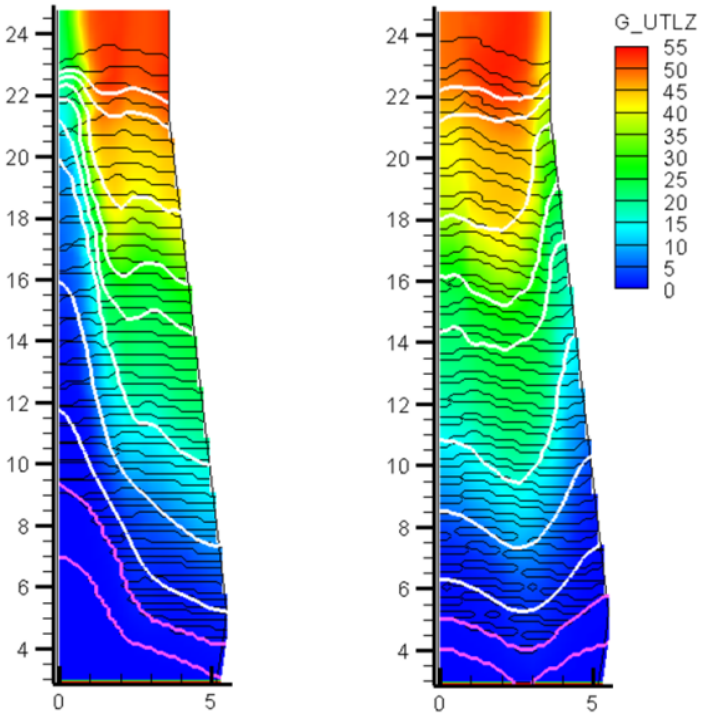

(a) Center working (b) Wall working

Figure 61 Effects of burden distribution on gas utilization (%)

The gas composition along the vertical direction of the shaft is plotted in Figure 62 and the three locations are shown in Figure 60, i.e., 0.90R is the location close to the furnace side wall and 0.04R is the center. In the center working furnace, it can be found in Figure 62 (a) that the gas composition has approached that for FeO/Fe equilibrium (70% CO, 30% CO_2) in the isotherm ranging from 700 °C to 900°C in periphery of the furnace to the middle (0.47R).However, in the center of the furnace (0.04R), the gas composition is far from FeO/Fe equilibrium because of the center coke charging. In the wall working furnace, the difference of the gas composition in three locations is relatively small in the lower shaft region where the burden temperature is high as shown in Figure 62 (b). In the upper shaft region with a lower burden temperature, there is more CO in the peripheral region than the center in the wall working furnace. In addition, the "W" shape CZ presents the lowest CO volume fraction in the mid-radial location (0.47R). By comparing the two cases, the gas composition held approximately the same relationship with the burden temperature except in the center of the center working furnace. It also shows that below the isotherm 600 °C and above 1200 °C, the gas composition is irrelevant to the burden temperature. However, the gas composition is a strong function of the burden temperature between 600 °C and 1200 °C.

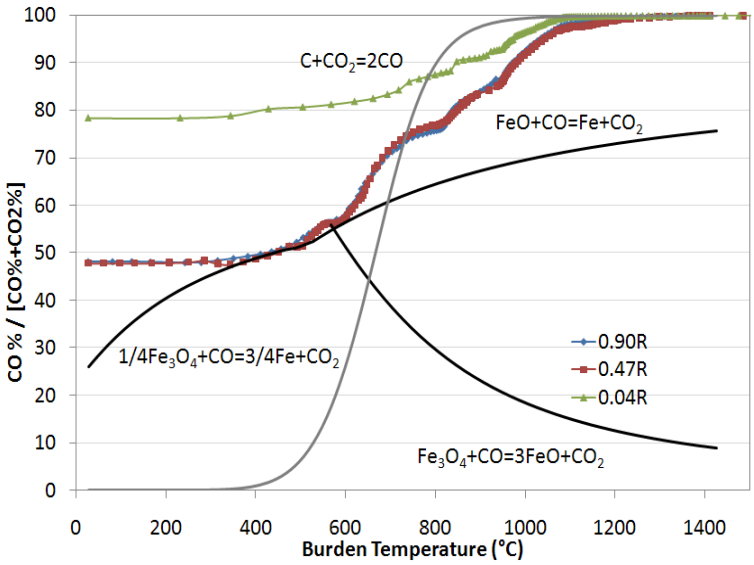

(a) Center working

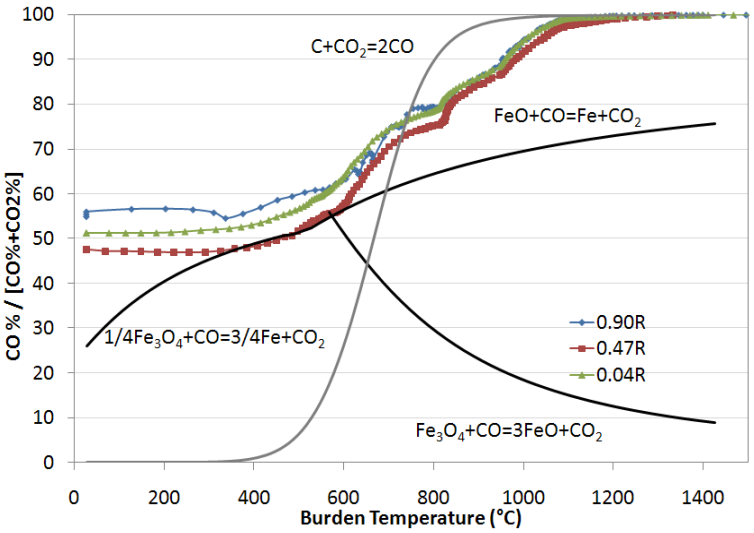

(b)Wall working

Figure 62 Vertical plot of gas composition and burden temperature

In Figure 63, the gas temperature is also determined by the CZ shape and position and shows the same pattern as the burden temperature.

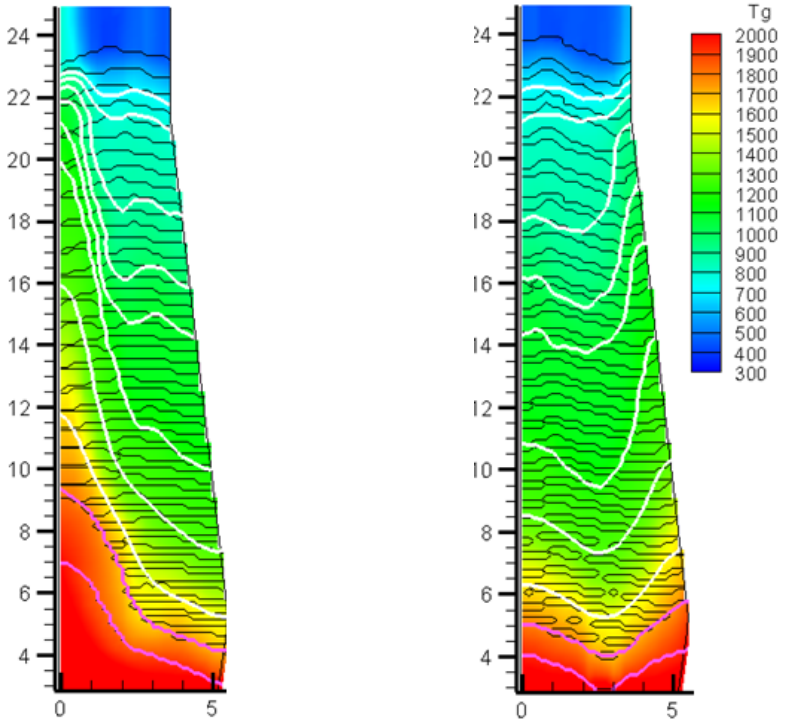

(a) Center working (b) Wall working

Figure 63 Effects of burden distribution on gas temperature (K)

The CZ represents a resistance to the flow of ascending gas and is also a gas flow distributor to the upper regions. It is thus interesting to examine the influence of the shape of the CZ on the gas flow. The inverted “V” CZ shows higher gas velocities towards the furnace center. The “W” CZ manifests a relatively higher gas velocity near the wall, the mid-radial location and the center of the furnace as shown in Figure 64. The color in Figure 64 shows the gas temperature and it is observed that the gas temperature is higher in the regions where a higher gas velocity exists.

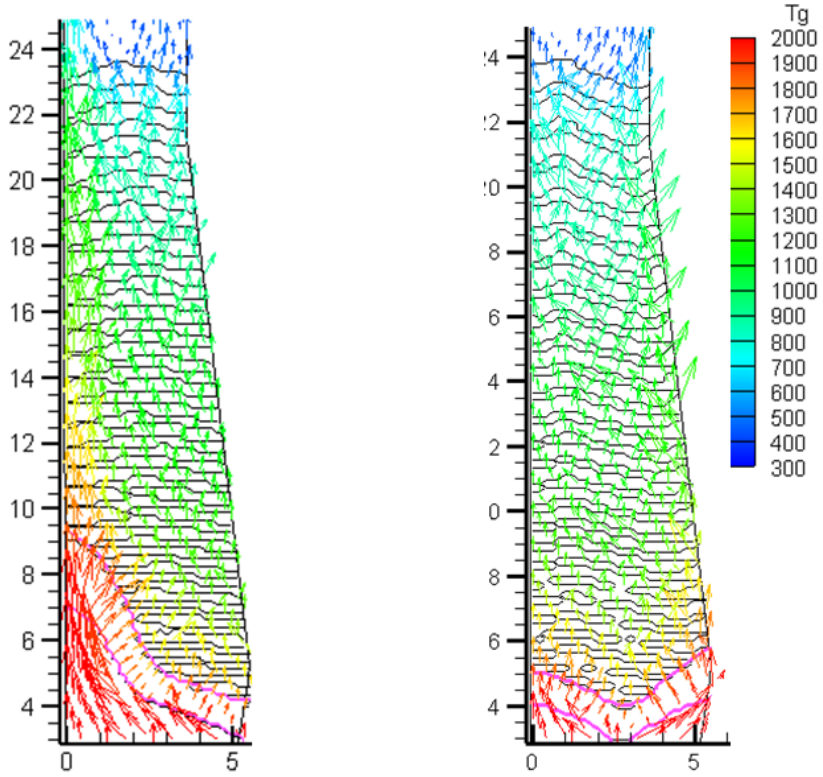

(a) Center working (b) Wall working

Figure 64 Effects of burden distribution on gas vector

The distribution of mass flux in the vertical direction is shown in Figure 65. In the center working furnace, higher mass flux rate is concentrated in the center of the furnace since more coke is charged in the furnace center below the CZ. The mass flux in the top of the furnace above the stock-line shows a strong uneven distribution in the radial direction for both cases due to the stock-line profile.

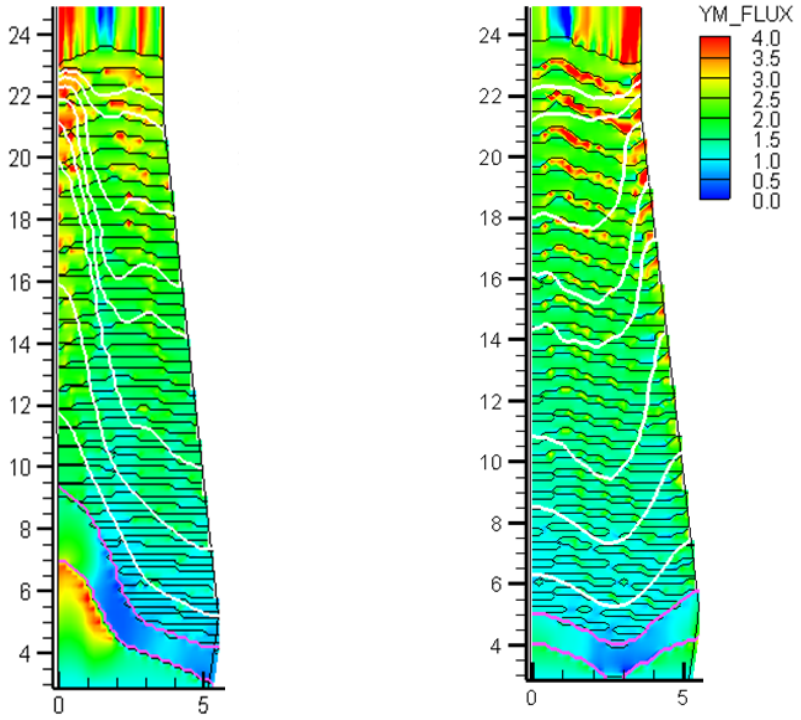

(a) Center working (b) Wall working

Figure 65 Effects of burden distribution on gas vertical mass flux (kg/m2)

Since blast flow and tuyere conditions are identical for both cases, changes in burden distribution lead to different pressure drops because the burden permeability is associated with the burden arrangements. In Figure 66, the wall working furnace shows about 15% more pressure drop across the burden than the center working furnace.

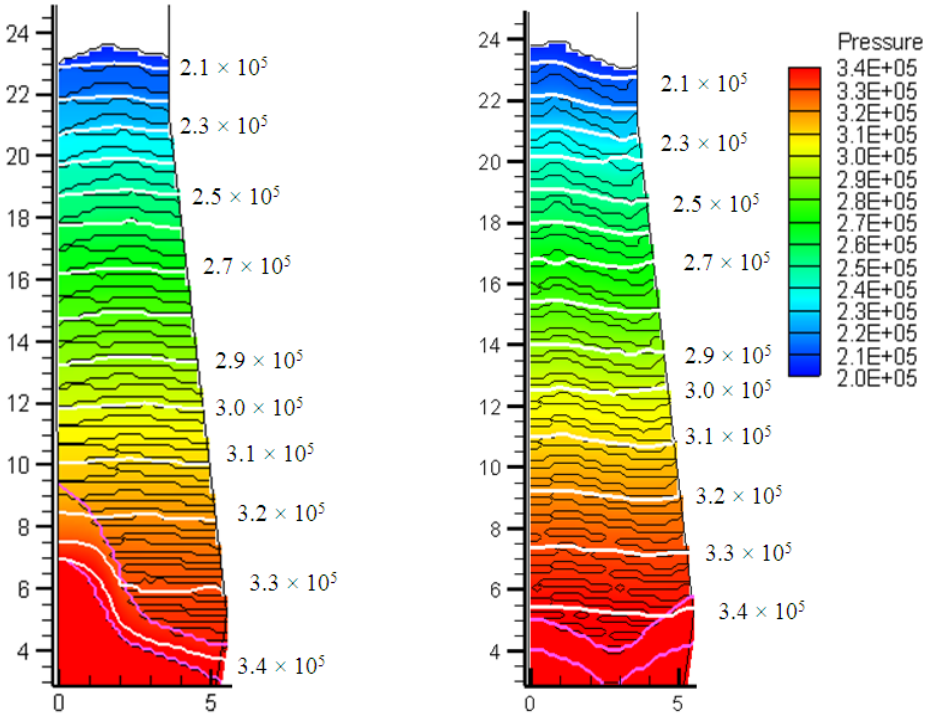

(a) Center working (b) Wall working

Figure 66 Effects of burden distribution on gas pressure (Pa)

The heat transfer characteristics can be observed in Figures 67 - 68. The heat transfer between the gas and burden is intense in the lower part of the shaft. A large temperature gradient between the gas and burden is found below the 1000 °C isotherm, which is due to the highly endothermic coke gasification reaction and the high temperature bosh gas.

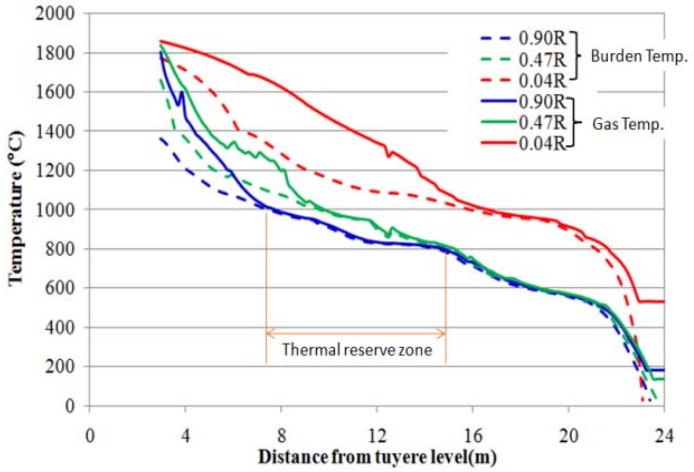

Center working

Figure 67 Gas and burden temperature distribution along the shaft

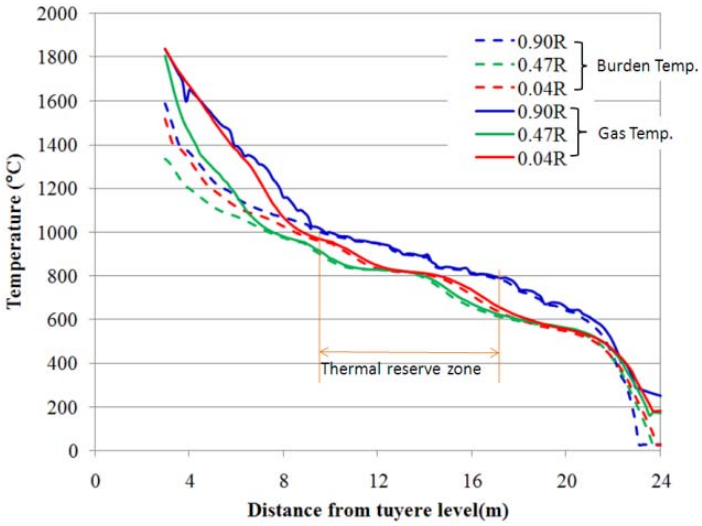

Wall working

Figure 68 Gas and burden temperature distribution along the shaft

As the gas continues its ascent above the 900 °C isotherm, the CO continues to react with wustite (FeO) to form solid Fe and CO_2. The reaction given by reaction $FeO(s) + CO(g) \rightarrow Fe(s) + CO_2(g)$ is slightly exothermic and as a result the gases do not cool down during their ascent

through this region. This forms the TRZ of the furnace. It is noticed that the length of the TRZ is shortened in the region of low gas utilization, i.e. the center and peripheral region of the center working furnace and the wall working furnace. The TRZ also indicates the regions where there are small changes of gas temperature and composition as can been seen from Figure 70.

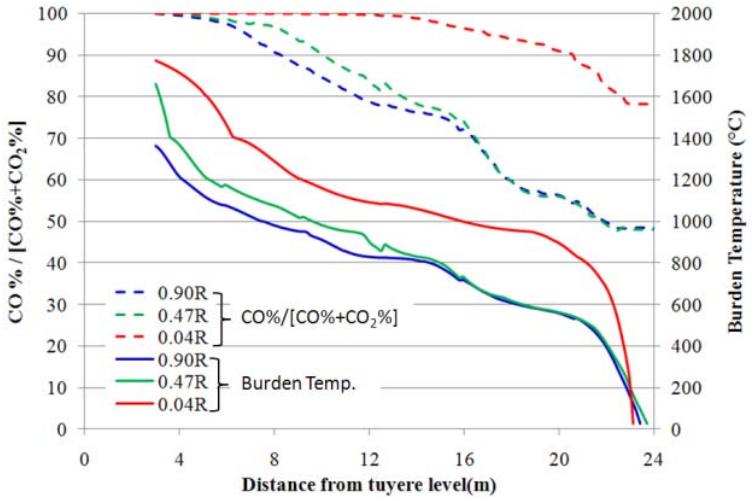

Center working

Figure 69 Gas composition and burden temperature distribution along the shaft

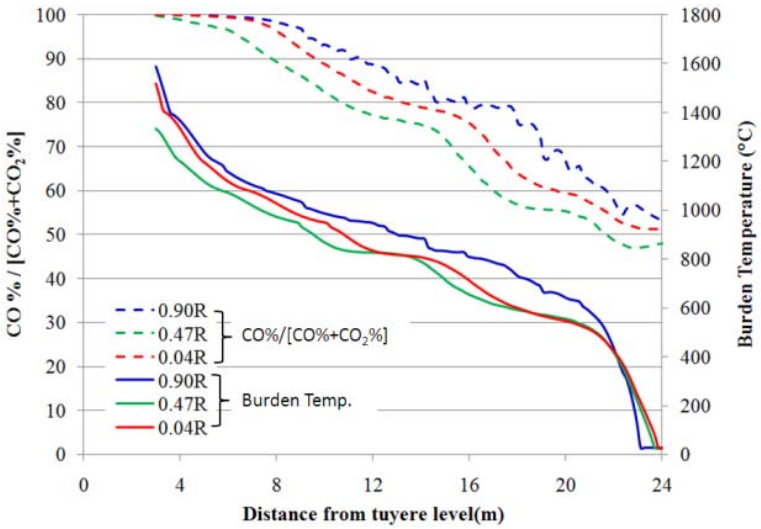

Wall working

Figure 70 Gas composition and burden temperature distribution along the shaft

Figure 71 shows the CO sequentially reduces Fe_2O_3 to Fe_3O_4; Fe_3O_4 to FeO, and FeO to Fe from the top to bottom of the furnace.

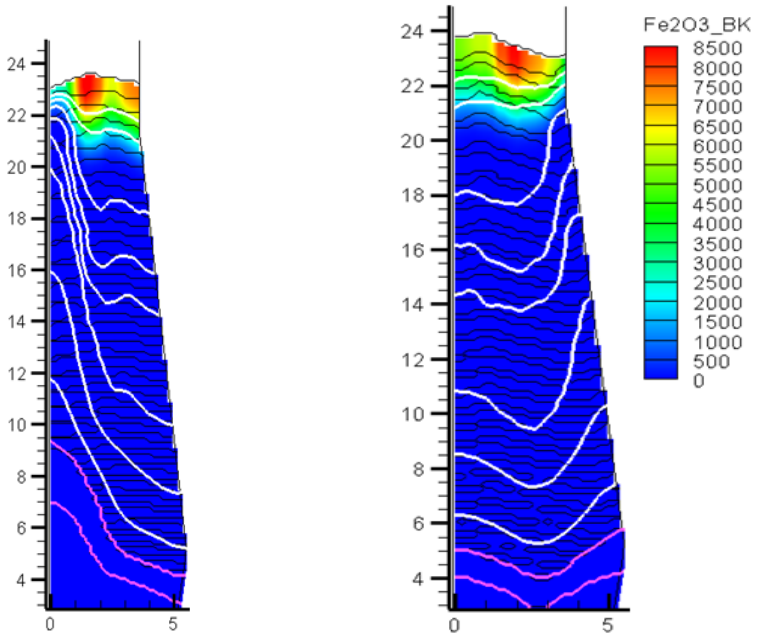

(a) Fe2O3

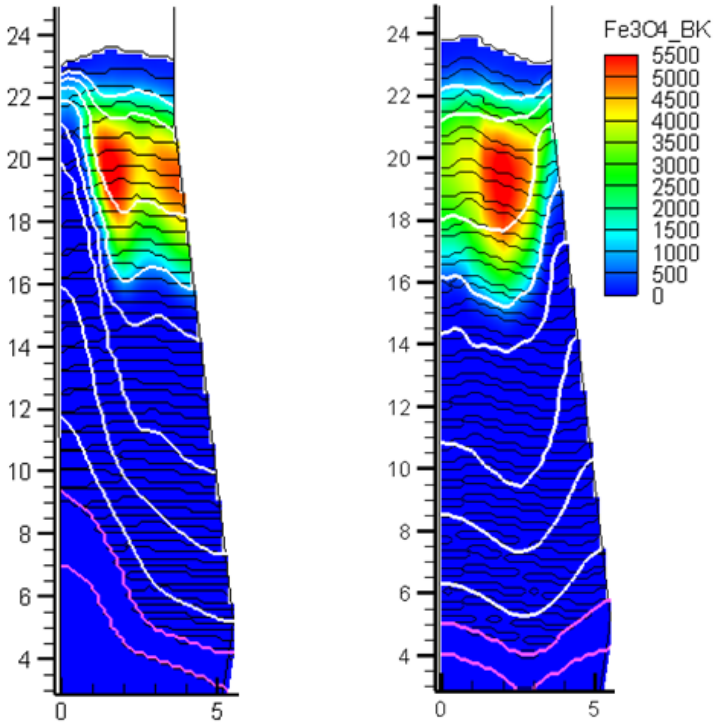

(b) Fe3O4

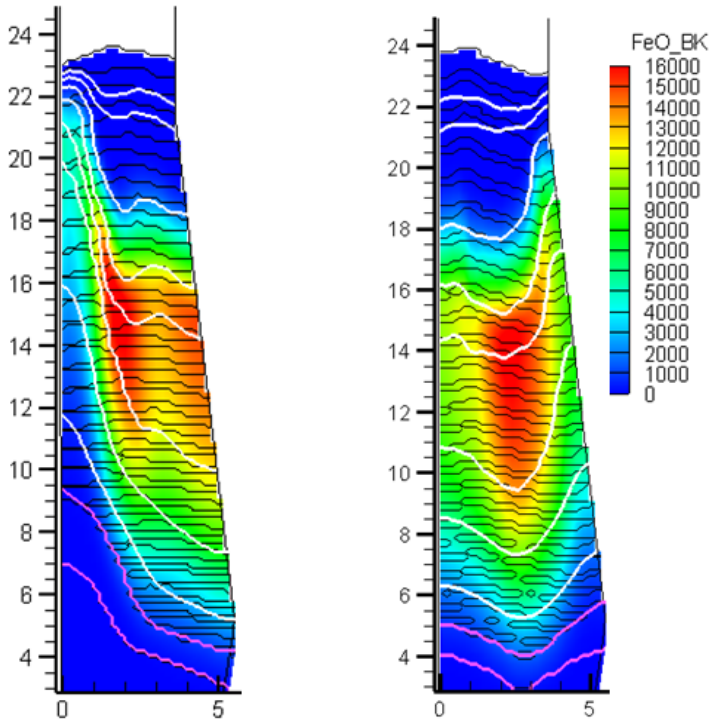

(c) FeO

Figure 71 Effects of burden distribution on burden composition (mol/m3)

By comparing the distribution of burden composition for both cases in Figure 71, the step-wise reduction reaction is evident. Therefore, the assumption of the single interface in the shrinking core model is appropriate.

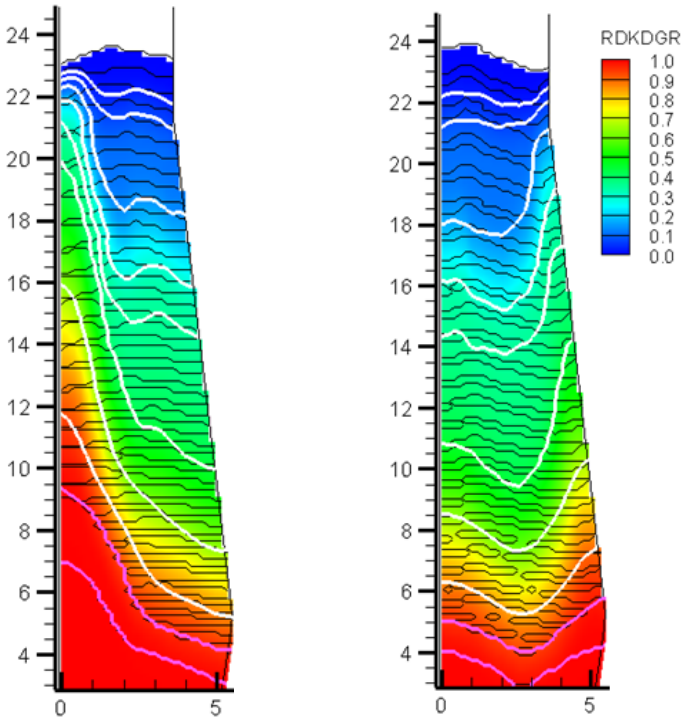

(a) Center working (b) Wall working

Figure 72 Effects of burden distribution on degree of reduction (-)

The degree of reduction shown in Figure 72 indicates the highest reduction rate takes place in the temperature range of 1000°C to 1100 °C where both the reduction of wustite and coke gasification are promoted.

The CO and CO_2 distribution at the furnace top for the two cases are shown in Figure 73. The gas distribution is corresponding to the temperature distribution shown in Figure 73 (a). The volume fraction of the CO is higher in the high gas temperature area. It indicates that high temperature CO is exiting the furnace in case of center working blast furnace.

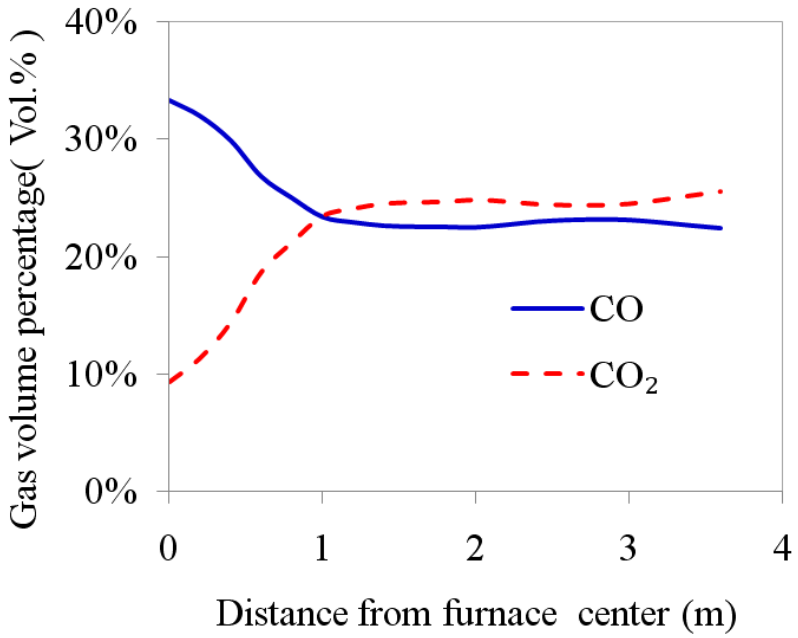

(a) Center working

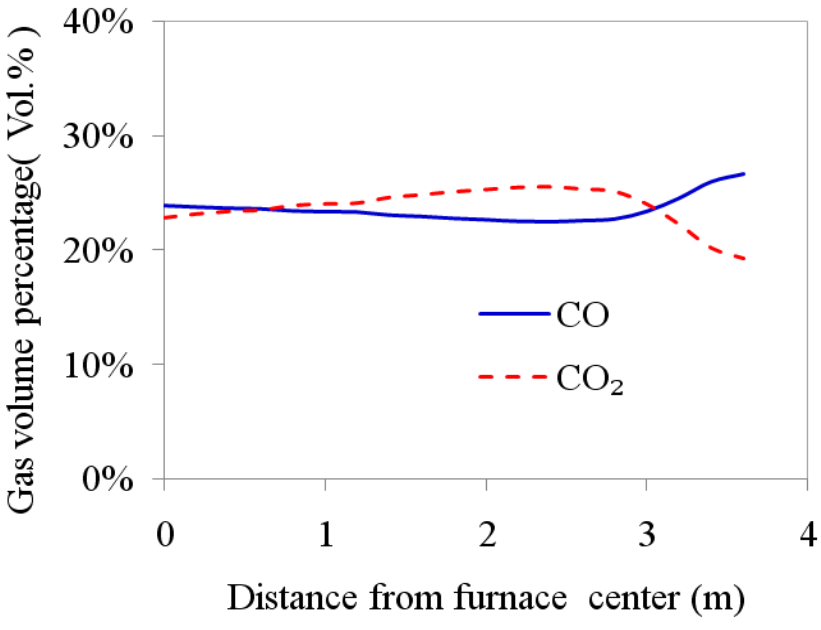

(b) Wall working

Figure 73 Effects of burden distribution on top gas CO and CO_2

The temperature distributions at the furnace top for the two cases are shown in Figure 74 (a). It shows high gas temperature is predicted in the furnace center, with a relatively uniform distribution starting from about 1 meter away from the center. The temperature for the wall working furnace is slightly higher in the periphery region. The comparison of the top gas utilization is provided in Figure 74 (b). The gas utilization ($CO_2/(CO+CO_2)$) is a key parameter in evaluating furnace performance. The enhanced central flow in the center working furnace leads to an inefficient utilization while the wall working furnace has relatively uniform gas utilization in the radius direction. Higher gas utilization is found in the wall working furnace case.

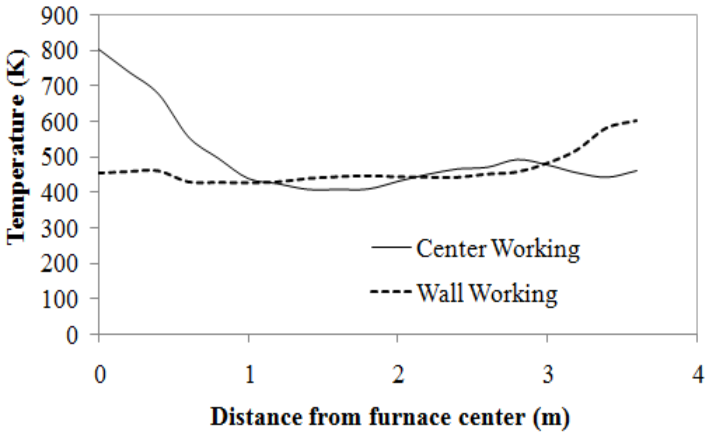

(a) Top gas temperature

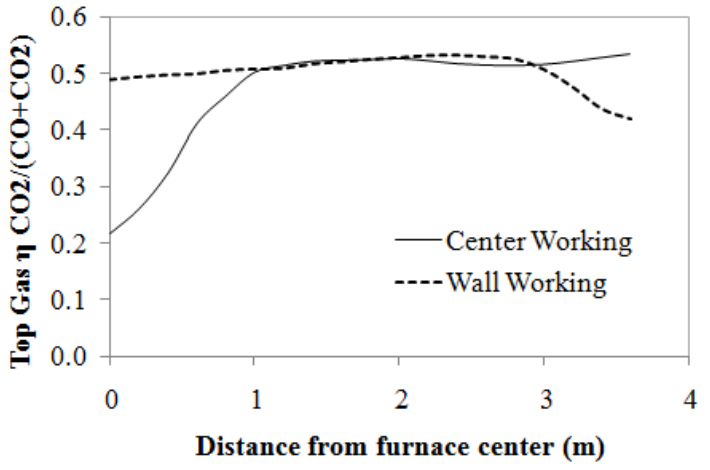

(b) Top gas utilization

Figure 74 Effects of burden distribution on top gas distribution

The averaged value for the top gas is summarized in Table 14. The gas utilization is about 2 percent higher in the wall working case compare to the center working case.

Table 14 Effects of burden distribution on top gas

Case	Top gas temp. (°C)	Top gas Vol.%				
		CO	CO_2	H_2	N_2	$CO_2/(CO+CO_2)$
Center Working	246	25.1	21.7	7.1	46.2	46.4%
Wall Working	232	24.3	22.6	6.9	46.2	48.1%

3.7.4 Effects of Tuyere Operations

The effects of tuyere operation on blast furnace shaft are investigated. Operating conditions for the all the cases are summarized in Table 15. The cases were chosen so that the calculated Raceway Adiabatic Flame Temperature (RAFT) was kept approximately constant.

Table 15 Case list for different tuyere operations

Case	Ambient Wind Rate, 10^3 SCFM	Blast Temp., ^{0}F	Oxygen Added Through Blast, 10^3 SCFM	Lance Oxygen Rate, 10^3 SCFM	Total Oxygen added, 10^3 SCFM	Moisture Added, Grain/SCFM	PCI Rate, NT/hr	PCI Carrier Gas Rate, 10^3 SCFM	Natural Gas Rate, 10^3 SCFM
1	135.8 0	2010	12.99	4.20	17.19	6.0	29.3	2.50	14.20
2	135.80	2010	12.99	4.20	17.19	6.0	29.3	2.00	14.20
3	135.80	2010	10.90	4.20	15.10	9.0	29.3	2.50	11.50
4	135.80	2010	8.80	4.20	13.00	12.0	29.3	2.50	9.00
5	135.80	1800	12.99	4.20	17.19	7.0	29.3	2.50	11.3
6	135.80	2010	12.99	2.81	15.80	6.0	29.3	2.50	14.20

Due to the different tuyere parameters, the corresponding average bosh gas volume and composition changes are listed in Table 16.

Table 16 Bosh gas volume and composition

	Case1	Case2	Case3	Case4	Case5	Case6
Bosh Gas, N_2, SCF/NTHM	25081	25007	25091	25049	25137	25081
Bosh Gas, CO, SCF/NTHM	23068	23087	22438	21709	23258	22484
Bosh Gas, H_2, SCF/NTHM	10042	10048	9108	8247	8865	10042
Total Bosh Gas, SCF/NTHM	58191	58143	56637	55006	57260	57618
Bosh CO+H_2, SCF/NTHM	33110	33135	31546	29957	32123	32529
Bosh Gas, N_2, Vol.%	43.10%	43.01%	44.30%	45.54%	43.90%	43.54%
Bosh Gas, CO, Vol.%	39.64%	39.71%	39.62%	39.47%	40.62%	39.02%
Bosh Gas, H_2, Vol.%	17.26%	17.28%	16.08%	14.99%	15.48%	17.43%

The CO distributions for all the cases are shown in Figure 75. The white lines are isothermal lines ranging from 400 ºC to 1100 ºC from top to bottom. Table 17 shows that the effects of carrier gas flow rate on the efficiency of blast furnace is negligible.

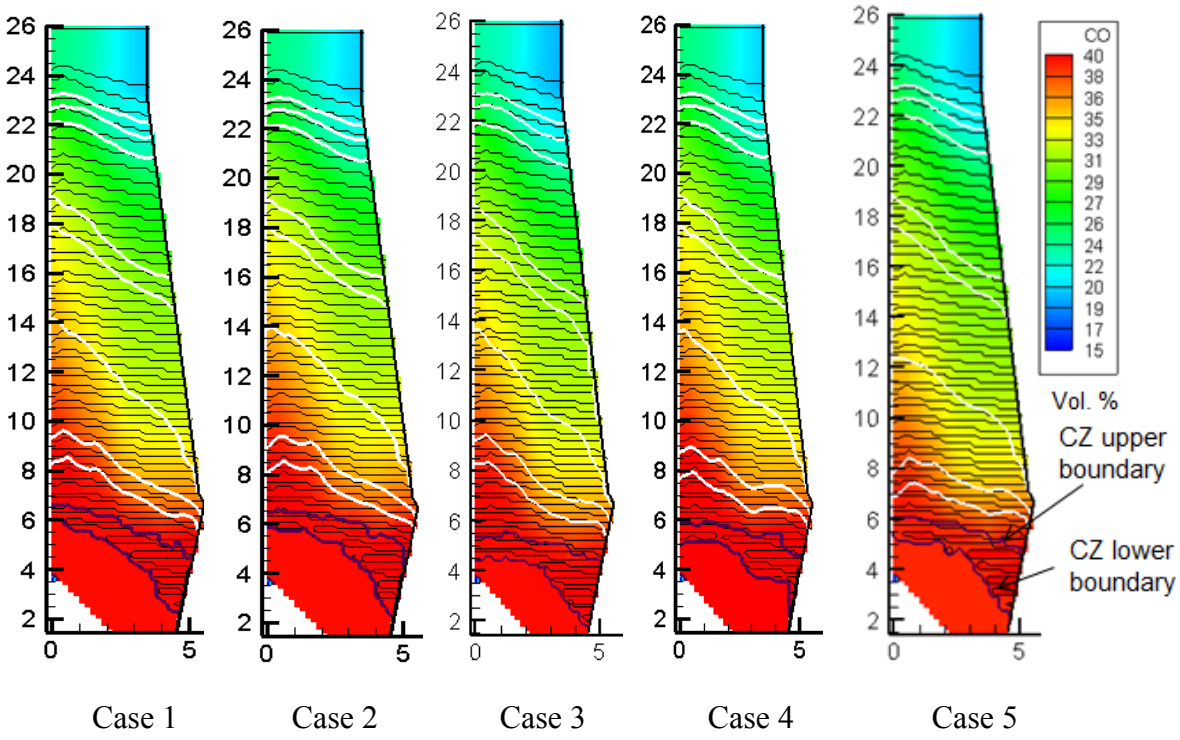

Figure 75 Effect of tuyere operation on CZ shape and CO distribution

Table 17 Effects of carrier gas flow on blast furnace performance (continued next page)

	Case 1 Carrier Gas 2500 scfm	Case 2 Carrier Gas 2000 scfm	Difference =Case2-Case1
Top Gas Average Temp. (^{0}C)	152	152	0
% CO_2	23.38	23.39	0.01
% CO	24.40	24.46	0.05
% H_2	8.66	8.66	-0.01
% N_2	43.55	43.50	-0.05
CO Gas Utilization	48.93%	48.88%	-0.05%
H_2 Gas Utilization	50.31%	50.47%	0.16%

Coke Rate (lb Coke/NTHM)	666.8	665.6	-1
Solution Loss (lb C/NTHM)	100.5	101.1	1
Carbon For Combustion (lb C/NTHM)	646.9	645.2	-2
Carbon from PCI (lb C/NTHM)	160.6	160.6	0
Carbon from NG (lb C/NTHM)	93.3	93.3	0
Carbon from Coke(lb C/NTHM)	591.5	590.4	-1
Total Carbon Rate (lb C/NTHM)	845.4	844.4	-1

Natural gas injection into the blast furnace can reduce coke consumption. Injecting natural gas also reduces NOx and SOx emissions compared to other supplemental fuel such as coal or coke oven gas. The natural gas provides not only the carbon for CO generation in the raceway, but also the hydrogen in the bosh gas which is a powerful reduction agent. The distribution of the reduction degree in the blast furnace shaft for different natural gas injection rates is shown in Figure 76. The red line is the iso-value line for reduction degree while the blue line indicates the shape and location of the CZ. It is found that as the natural gas injection rate increases, the CZ location is higher and reduction of the iron oxides is accelerated.

Figure 77 shows the coke reaction rate for the two cases. In case 1 with higher natural gas injection rate, the coke reaction with CO_2 and H_2O is decreased. The quantitative total amounts of both reactions are available in Table 18. The combination of reaction $C(s) + CO_2 (g) \rightarrow 2CO (g)$ and $FeO(s) + CO(g) \rightarrow Fe(s) + CO_2 (g)$ is $FeO(s) + C \rightarrow Fe(s) + CO_2 (g)$, and the combination of reaction $C(s) + H_2O(g) \rightarrow CO + H_2 (g)$ and $FeO(s) + H_2 (g) \rightarrow Fe(s) + H_2O (g)$ are combined into the solution loss reaction $FeO(s) + C \rightarrow Fe(s) + CO_2 (g)$. Therefore, decresing the rate of coke reaction with CO_2 and H_2O indicates a lower amount of solution loss in the furnace. It is consistent with the industry practice as shown in Figure 78. The top gas temperature and CO utilization distributions are shown in Figures 79 and 80. The Case 1,3 and 4 in the following figures are the CFD results for the cases listed in Table 16.

The top gas temperature increases as natural gas injection rate increases. However, the CO gas utilization is lower if the natural gas rate is high due to the presents of more hydrogen. It is also found that increasing the natural gas injection rate reduces the coke rate but the total carbon rate per unit ton hot metal increases as shown in Table 18.

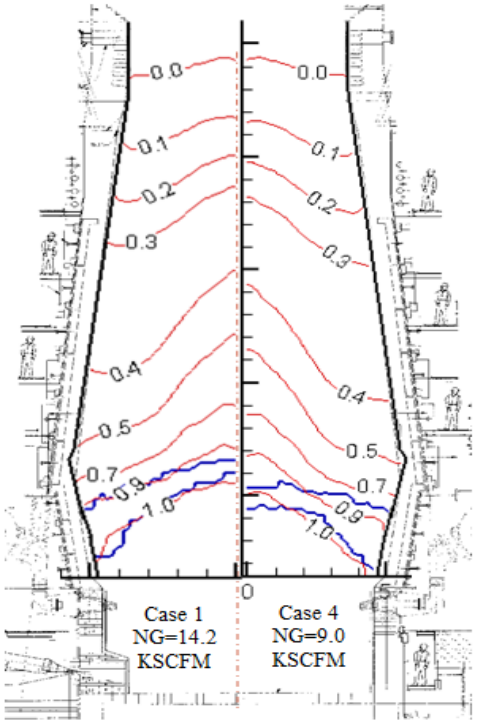

Figure 76 Effect of natural gas injection rate on CZ shape and reduction degree

Reaction rate of C(s) + CO_2 (g) → 2CO (g) Reaction rate of C(s) + H_2O (g) → CO (g) + H_2 (g)

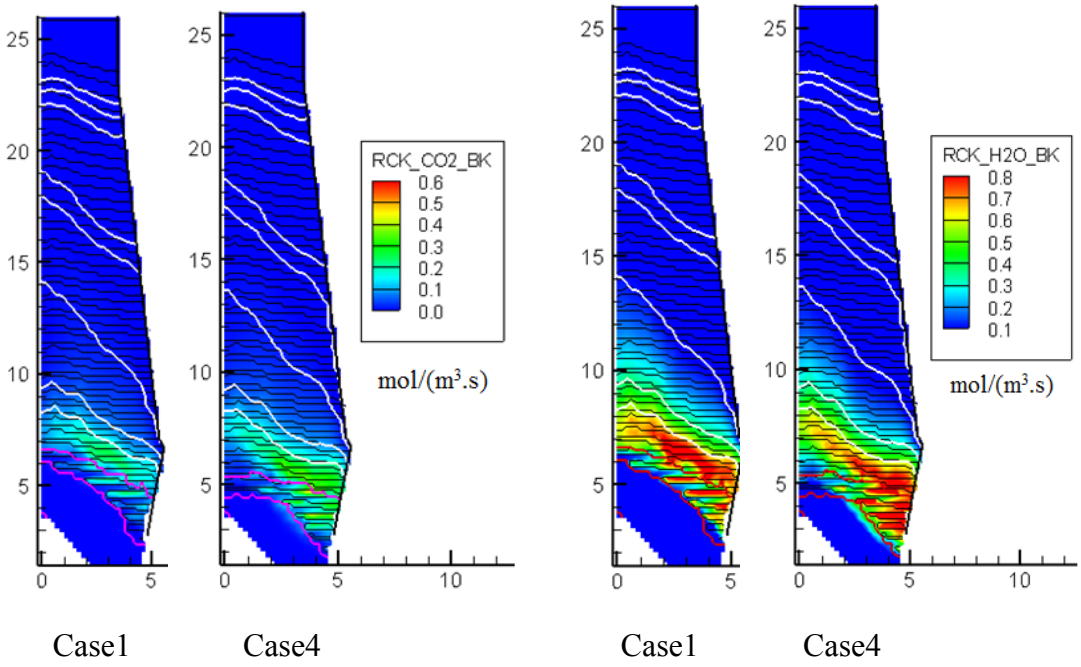

Figure 77 Effect of natural gas injection rate on coke reaction

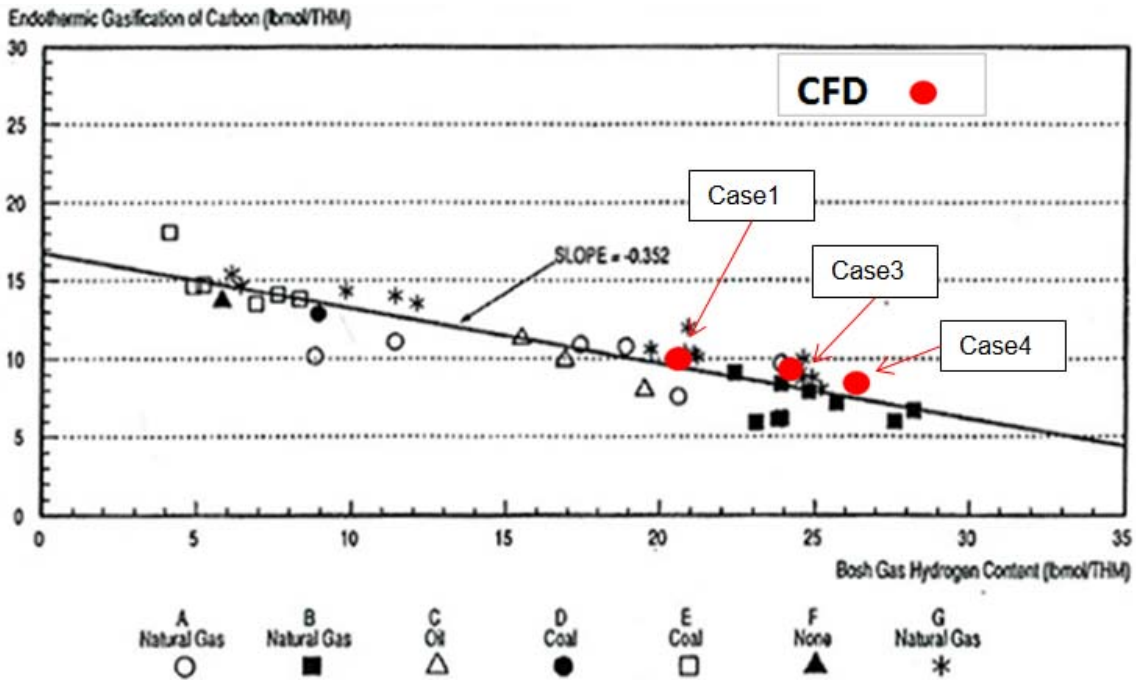

Figure 78 Endothermic gasification of carbon versus bosh hydrogen for several operating commercial blast furnaces. [Agarwal et al. 1992]

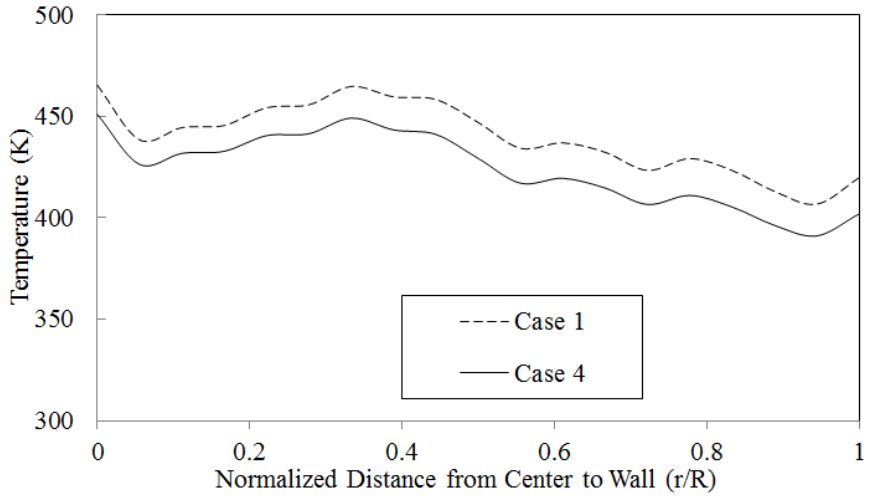

Figure 79 Effects of natural gas injection rate on top gas distribution

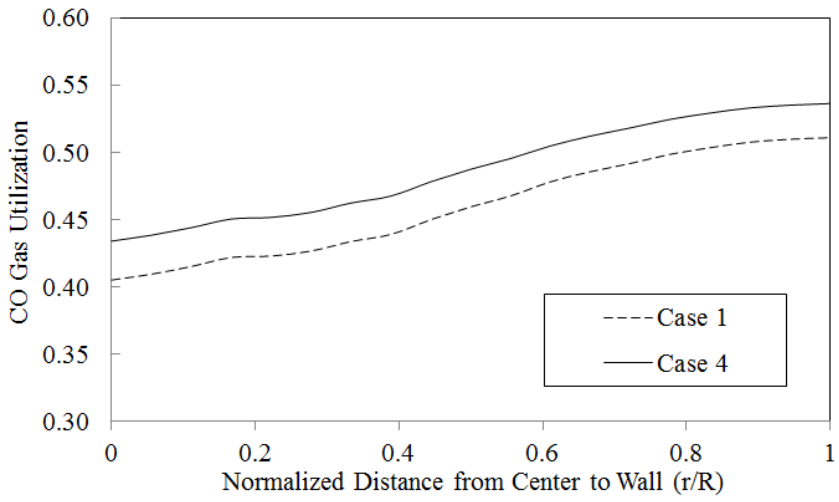

Figure 80 Effects of natural gas injection rate on top gas distribution

Table 18 Effects of natural gas flow rate on blast furnace performance (continued next page)

	Case 1 NG=14.2 KSCFM	Case 3 NG=11.5 KSCFM	Case 4 NG=9.0 KSCFM	Difference =Case 4-Case 1
Top Gas Average Temp. (^{0}C)	152	140	136	-16
% CO_2	23.38	24.09	24.57	1.19
% CO	24.40	23.64	23.22	-1.19
% H_2	8.66	8.04	7.33	-1.34
% N_2	43.55	44.22	44.88	1.33
CO Gas Utilization	48.93%	50.47%	51.41%	2.48%
H_2 Gas Utilization	50.31%	49.97%	50.35%	0.04%
Coke Rate (lb Coke/NTHM)	666.8	673.0	680.5	14
Solution Loss (lb C/NTHM)	100.5	108.2	118.4	18
$C+CO_2=2CO$ (lb C/NTHM)	15.4	20.0	24.9	10

$C+H_2O=H_2+CO$ (lb C/NTHM)	84.9	87.3	87.7	3
Carbon For Combustion (lb C/NTHM)	646.9	627.0	607.0	-40
Carbon from PCI(lb C/NTHM)	160.6	160.6	160.6	0
Carbon from NG(lb C/NTHM)	93.3	75.5	59.1	-34
Carbon from Coke(lb C/NTHM)	591.5	597.0	603.7	12
Total Carbon Rate (lb C/NTHM)	845.4	833.2	823.4	-22

The effects of blast temperature on blast furnace performance are shown in Table 19. Increasing the blast temperature provides heat for supplying the reduction and melting of the burden of the shaft. Both the coke rate and carbon rate decrease as the blast temperature is higher.

Table 19 Effects of blast temperature on blast furnace performance (continued on next page)

	Case 1 Blast Temp 2010 ^{0}F	Case 5 Blast Temp 1800 ^{0}F	Difference =Case 5- Case1
Top Gas Average Temp. (^{0}C)	152	148	-4
% CO_2	23.38	24.12	0.74
% CO	24.40	24.43	0.03
% H_2	8.66	7.57	-1.09
% N_2	43.55	43.88	0.32
CO Gas Utilization	48.93%	49.68%	0.75%
H_2 Gas Utilization	50.31%	51.18%	0.86%
Coke Rate (lb Coke/NTHM)	666.8	696.1	29
Solution Loss (lb C/NTHM)	100.5	105.2	5
Carbon For Combustion (lb C/NTHM)	646.9	649.3	2

Carbon from PCI(lb C/NTHM)	160.6	160.6	0
Carbon from NG(lb C/NTHM)	93.3	74.4	-19
Carbon from Coke(lb C/NTHM)	591.5	617.5	26
Total Carbon Rate (lb C/NTHM)	845.4	852.5	7

The effects of oxygen enrichment on blast furnace performance are provided in Table 20, increasing the oxygen enrichment results in more fuel being consumed but it is helpful for enhancement of the burnout of the pulverized coal.

Table 20 Effects of oxygen enrichment on blast furnace performance

	Case 1 Oxygen. 10%	Case 6 Oxygen. 9%	Difference =Case 6- Case 1
Top Gas Average Temp. (^{0}C)	152	146	-6
% CO_2	23.38	23.52	0.14
% CO	24.40	23.71	-0.69
% H_2	8.66	8.84	0.17
% N_2	43.55	43.93	0.38
CO Gas Utilization	48.93%	49.79%	0.86%
H_2 Gas Utilization	50.31%	49.79%	-0.52%
Coke Rate (lb Coke/NTHM)	666.8	648.9	-18
Solution Loss (lb C/NTHM)	100.5	103.1	3
Carbon For Combustion (lb C/NTHM)	646.9	628.4	-18
Carbon from PCI(lb C/NTHM)	160.6	160.6	0
Carbon from NG(lb C/NTHM)	93.3	93.3	0
Carbon from Coke(lb C/NTHM)	591.5	575.6	-16
Total Carbon Rate (lb C/NTHM)	845.4	829.6	-16

3.8 Virtual Blast Furnace

With the application of VR to blast furnace CFD simulation, a virtual blast furnace has been developed on an immersive system at the Purdue University Calumet's CIVS. The virtual blast furnace includes: charging process, burden descending and gas distribution, coke and coal combustion, and bottom hearth inner profile. These four parts will be discussed further. In this application, advanced CFD simulation provides detailed flow characteristics while VR visualization offers a powerful way to present complex CFD data in an immersive 3D environment. This enabled researchers and collaborators to observe the facility in operation in a virtual world from a first-person perspective. It significantly reduced the time and effort needed for the evaluation, troubleshooting and optimization processes.

3.8.1 Top Charging and Burden Redistribution

The blast furnace process is a counter-current moving bed chemical reactor to reduce iron oxides to iron, which involves complex transport phenomena and chemical reactions. The iron-bearing burden consisting of sinter or pellets, is charged with coke in alternate layers from the top of furnace. The charging process had been simulated using CFD. The data then was converted to a VR system in which the other components had been introduced to animate the rotational charging process. Figure 81 (a) shows the overview of the charging system while (b) shows several layers of charged materials. The orange layer represents the iron ore while the black represents the coke. These two materials alternate as they are charged into the blast furnace. Figure 81 (c) and (d) present the charging operation at a different time.

(a) Charging system

(b) Charging process

(a) Coke charging

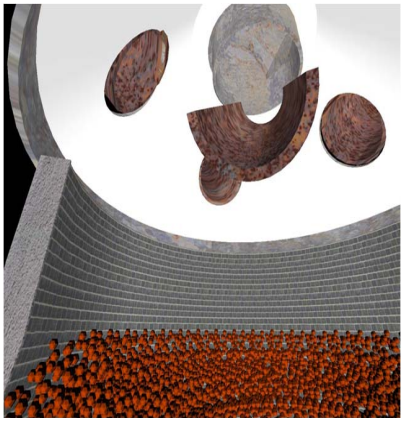

(b) Iron ore charging

Figure 81 Virtual charging system and its operation

After being charged into the blast furnace, the burden is redistributed during the burden descent due to the effects of shaft angle that increases the shaft area along its depth and the burden shrinkage during reduction and gasification. The burden shrinkage mainly is caused by a reduction and deformation of the iron ores and in the gasification of the coke. The burden redistribution will change the top profile of the burden and consequently influence the burden distribution. Figure 82 (a) and (b) show the burden distribution under a specific operating condition. The burden distribution data from the CFD calculation has been successfully presented as a part of the virtual blast furnace. Figure 82 (a) shows the overview of the furnace inner structure including the cohesive zone, combustion, and hearth that are discussed in the

following section. The focused burden distribution is shown in Figure 82 (b). In addition to the alternating layers of coke and iron ore, the cohesive zone and the center coke distribution have been included in this virtual model.

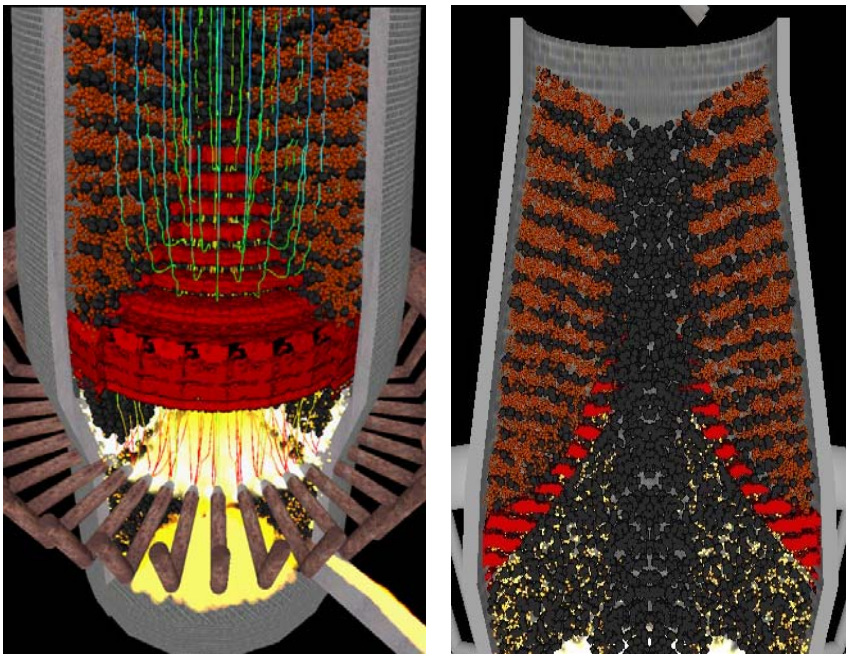

(a) Burden distribution (b) Detailed inner structure

Figure 82 Visualization of burden descending phenomenon in shaft

3.8.2 Gas Distribution

In this application, the CFD simulation of the burden descending inside the blast furnace was converted to a VR system as part of the virtual blast furnace. This module can be used to analyze the effects of charging operation, shaft angle, burden shrinkage, burden redistribution, burden top profile on the burden distributions.

Inside an operating blast furnace, the areas where the ore starts to soften and finally melts is called the cohesive zone. In the cohesive zone, ore layers become virtually impermeable thus forcing the ascending gas to pass through the coke slits present between the ore-layers. The shape and location of the cohesive zone is controlled by the distribution of burden and gas flow and impacted by the softening and melting properties of the burden materials. The cohesive zone in turn, has a great effect on the gas distribution. Therefore, it is important to estimate the characteristics of the gas flow in a blast furnace. Gas distribution being the result of numerous interacting phenomena, a mathematical model has been developed to better understand the gas flow inside the blast furnace.

The numerical data from the gas distribution model had been exported and post-processed to the VR system. This allows direct observation of all the simulation results in detail. It also provides a very intuitive way to fully understand the gas distribution during operation. Figure 83 (a) shows

an overview picture of the gas distribution while Figure 83 (b) focuses on a view showing the gas flow through the cohesive zone. Several detailed views of flow patterns are shown in Figure 84. Figure 84 (a) shows the gas flowing out of the tuyeres and (b) shows the gas flowing up through cohesive zone and alternate layers of coke and iron ore. Figure 85 (a) and (b) present the gas distribution inside the virtual blast furnace form side view and top view. The streamline describes very detailed flow pattern from different perspectives.

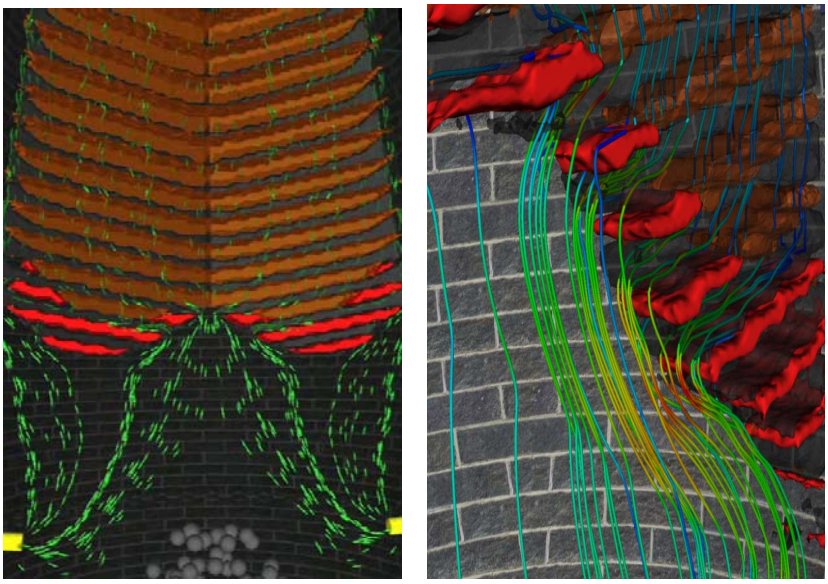

(a) Overview of gas distribution (b) Flowing through cohesive zone

Figure 83 Gas distribution through the burden materials

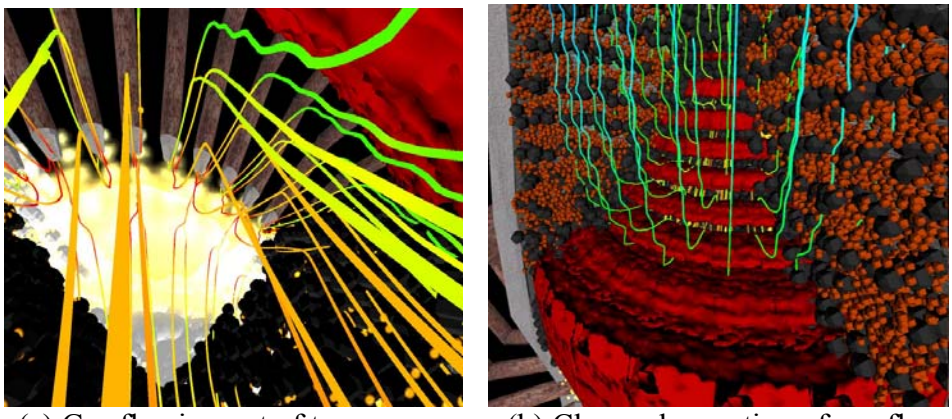

(a) Gas flowing out of tuyeres (b) Closer observation of gas flow

Figure 84 Detailed gas distribution inside blast furnace shaft

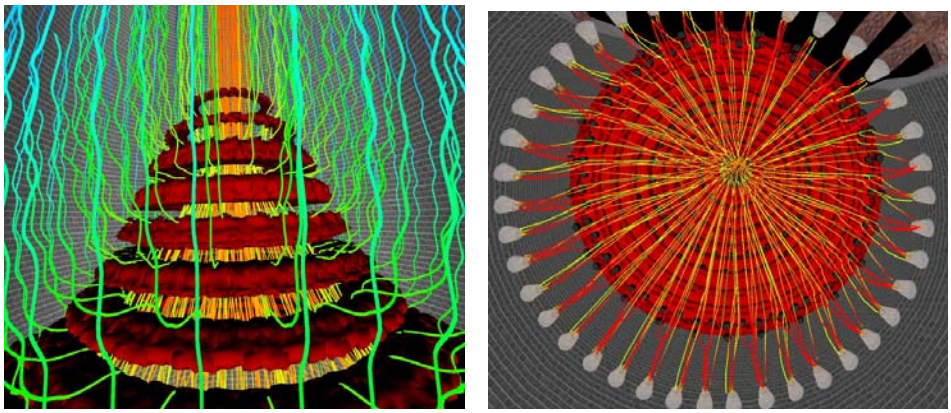

(a) Interaction of flow and cohesive zone (b) Top view of combustion gas

Figure 85 Detailed gas distribution inside blast furnace shaft

In this application, the VR model of a blast furnace gas distribution has been constructed and integrated to the virtual blast furnace model. The 3-D effects of the raceway, raceway combustion and burden distribution have also been taken into account.

3.8.3 Raceway and PCI Combustion

High rate pulverized coal injection (PCI) into a blast furnace is an attractive technology in the iron-making process. The purpose of high rate PCI is to reduce the hot metal cost and energy consumption and environmental emissions. However, increasing the amount of coal injected into a blast furnace is currently limited by the lack of knowledge of some issues related to the process. It is therefore important to understand the complex physical and chemical phenomena in the PCI process. A comprehensive CFD model had been developed to help understand the complex PCI process. A VR model has been created to visualize the detailed CFD data of gas velocity, temperature and species distributions, particle number density and unburned char distributions, raceway formation, as well as combustion efficiency. Figure 86 (a) shows the visualization of the single raceway combustion while Figure 86 (b) presents a top view of the raceway combustion from the entire tuyere system.

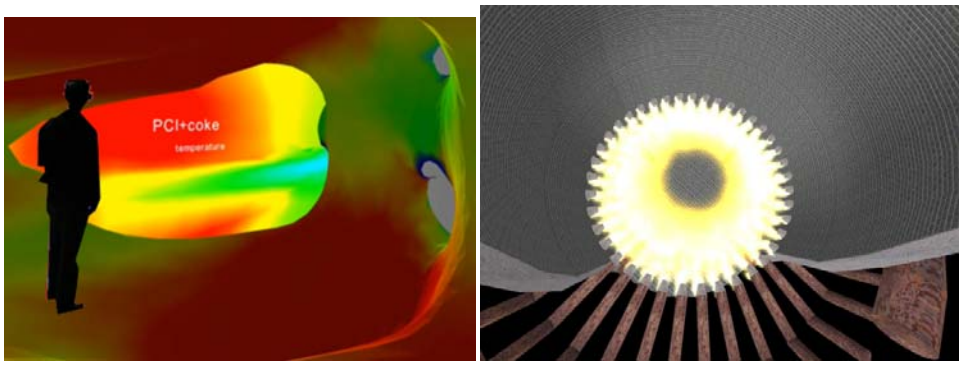

(a) Combustion inside raceway (b) Coal and coke combustion (Top view)

Figure 86 Virtual combustion process in a blast furnace

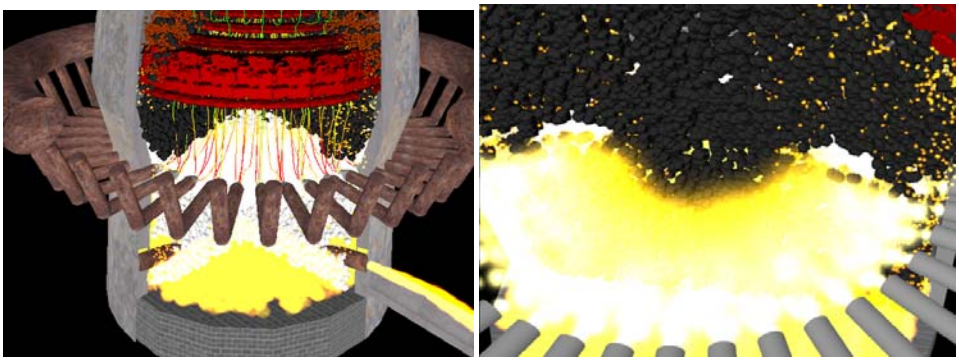

(a) Detailed combustion (b) Close observation of combustion

Figure 87 Combustion visualization in an immersive system

The combustion phenomenon has been visualized using the VR system. As shown in Figure 87 (a) and (b), the flame from the coke combustion can be observed together with the inner burden structure and cohesive zone. This virtual model allows the users to literally fly into the flame to observe the detailed combustion and it provides an intuitive environment that is very informative for both training and research.

3.8.4 Hearth Inner Profile

The importance of blast furnace in iron-producing and the costs in building, relining and repairs have made it critical to know the erosion condition in the hearth and adjust the operating parameters accordingly. Accurate and efficient prediction of the erosion profile in a blast furnace hearth is a necessary precondition to a real-time monitoring system. Considerable efforts have been made to predict the inner erosion profile using CFD. A comprehensive CFD model had been developed using measurement temperatures as a boundary condition. A VR model has been created based on the simulation results. Figure 88 (a) shows an example of the hearth

visualization which can present the inner structure materials clearly. In Figure 88 (b), the distribution of fire brick and skull can be observed to evaluate the degree of inner erosion.

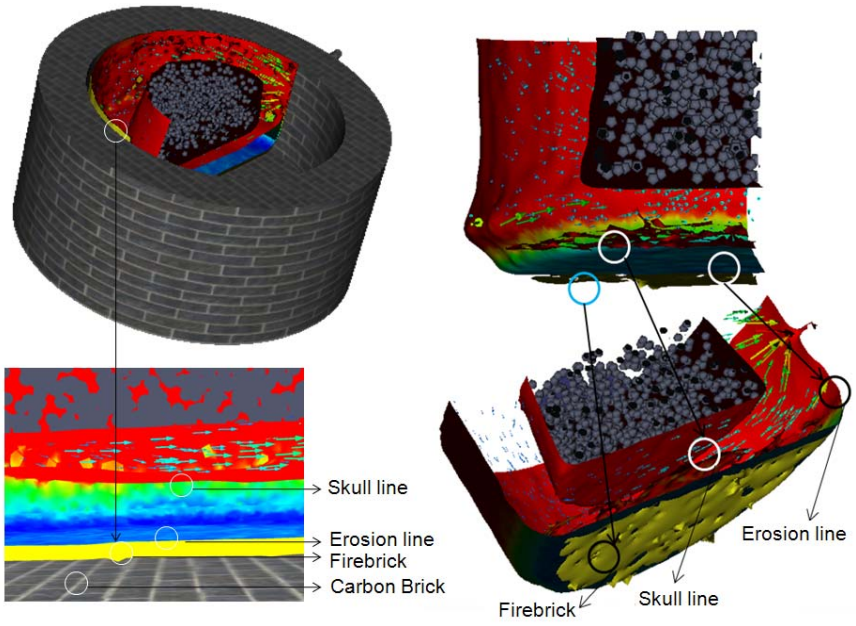

(a) Overview of the hearth (b) Detailed inner profile

Figure 88 Virtual blast furnace hearth model

Due to erosion on the walls, the inner profile of the blast furnace hearth changes constantly. This affects liquid iron flow pattern inside the hearth. The flow distribution calculated from the CFD model has been integrated into the hearth erosion model. Detailed flow patterns can be observed in Figure 89(a) and (b). It can be seen that the liquid iron flows into the tap hole inside the furnace hearth.

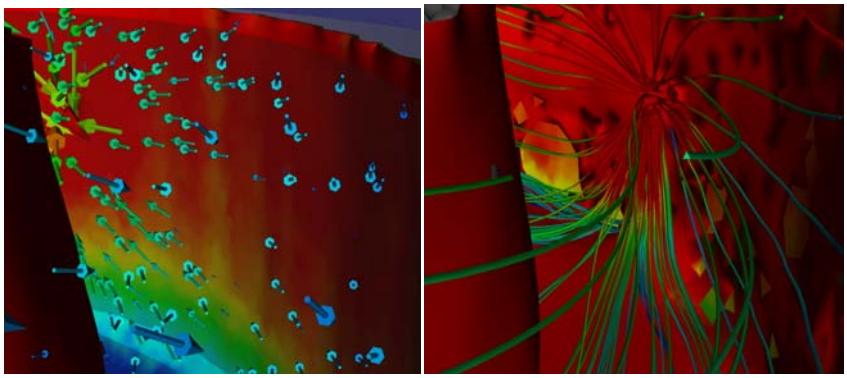

(a) Flow vector pattern at taphole (b) Streamline pattern at taphole

Figure 89 Detailed flow distribution inside blast furnace hearth

As part of the entire virtual blast furnace, the numerical results from the erosion model have been converted to a VR system for direct observation of the hearth inner profile and flow pattern. Detailed transient wall structure and flow characteristics are presented in a 3-D immersive environment. This model can be employed to visualize the flow, temperature and wear pattern inside the hearth, facilitate further understanding of interaction between flow conditions, deadman state, erosion profile and buildup formation. It can also be used to study the impact of changes in operating parameters on erosion conditions as well as investigate the mechanical and thermal mechanism of blast furnace hearth erosion.

4 BENEFITS ASSESSMENT

4.1 Carbon Consumption of Blast Furnaces and CO_2 Emission

The carbon is introduced into a BF through the fuels such as coke, pulverized coal, natural gas and hydrocarbon oil. As shown in Figure 90, the carbon is formed as the metallurgical inevitable as top gas is released from the BF. A portion of the top gas is used to heat up the cold blast in the hot stoves, while the remaining is utilized in other energy demand facilities. The dissolved carbon in the hot metal will be refined in the basic oxygen furnace to a very low level by forming CO. The CO obtained will also be recovered and used as an energy supplier. At the end, all the carbon is eventually converted to CO_2 and emitted [Schmole et al. 2005]. Reducing the CO_2 is essentially decreasing the carbon rate of the BF.

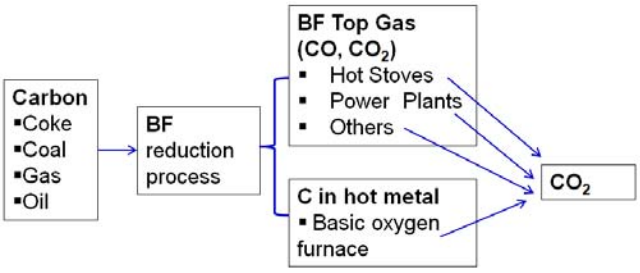

Figure 90 Carbon consumption in the BF and CO_2 emission

From a thermodynamic point of view, the carbon rate of the BF is determined by two requirements, namely the energy balance and mass balance. First, the heat released from the combustion of carbon must satisfy the energy requirements, i.e., direct reduction of Wustite (FeO), melting of hot metal and slag and heating up the solid burden. And second, the CO generated from combustion and direct reduction must be sufficient for the indirect reduction of FeO, magnetite (Fe_3O_4) and hematite (Fe_2O_3). Those two requirements are graphically illustrated in Figure 91. The K_{AB} is determining the carbon consumption due to the direct reduction, i.e. FeO+C=Fe+CO and the heat for the endothermic reaction. The line K_{CD} is determining the carbon consumption due to the indirect reductions, i.e., the reduction of FeO+CO=Fe+CO_2 only, based on the thermal dynamic equilibrium at 900 ºC. The intersection O_1 is the theoretical minimum or ideal carbon rate for a specific operation condition. However, the intersection O_1 is changing with the operation condition [Na 2005, Song 2005].

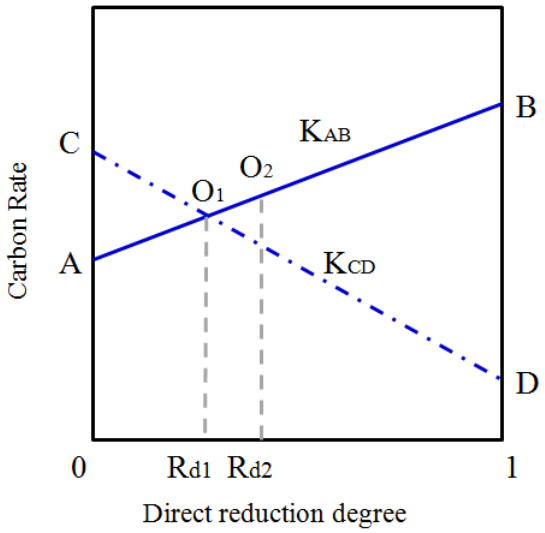

Figure 91 Carbon rate of the blast furnace

In reality, due to the necessary potential required by the chemical equilibrium, the blast furnace would not be able to reach the minimum carbon rate but only to get closer to this point, as shown in the point O_2 in Figure 91.

4.2 Application of the CFD Model to Reduce CO2 Emission

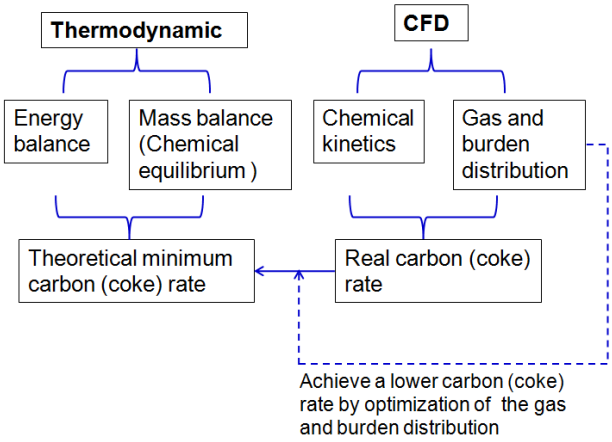

Figure 92 Methodology of the CFD model for reducing carbon rate

As shown in Figure 92, the purpose of the CFD model is to adjust the burden and gas distribution to lower the carbon rate. The CFD model will consider the compressible gas flow through the burden column along with the major reactions between the gas flow and burden materials, which will be determined by the chemical kinetics. Using this model, a series of parametric studies may guide the burden distributions to the proper pattern for reaching the lowest and achievable fuel rate.

The target of this project is to reach 1.75 GJ/MTHM in energy savings for blast furnace ironmaking, which is 80% of the maximum potential energy saving (2.19 GJ/MTHM) and corresponds to 13.9% energy saving in comparison to the actual energy consumption of BF ironmaking of good practices in USA. These calculations are based on the AISI Steel Energy Tool with assumptions of 2% of market impacted, 2.5% of annual growth rate, 2 year of introduction, and 10 year market saturation. Based on inputs using the AISI Steel Energy Tool, this technology (when fully implemented in the US) is projected to have the following impacts:

Total estimated energy savings of up to 4.965 trillion Btu.

Potential reductions in emissions as follows:

Carbon (MMTCE/yr)	0.12413
Nitrogen Oxides (NOx)	2,775,623 lbs
Carbon Monoxide (CO)	124,133 lbs
Volatile Organic Compounds (VOCS)	9,931 lbs
Particulates	129,099 lbs

5 ACCOMPLISHMENTS

The development of a Blast Furnace Shaft Simulator (BFSS) model, including the 3-D CFD solver, burden simulator, and the GUI for pre-processing and post-processing, and the virtual reality visualization has successfully been completed.

Validations of CFD sub-models have been conducted using experimental data from literature, laboratory, and on-site measurements. The model has been used to simulate an industry blast furnace based on real operational data and was validated by comparing the results with plant measurements.

A two day workshop was held in PUC on June 19 and June 20 2012. Seven attendees from steel companies and two attendees from AISI participated in the events. The participants provided positive feedback confirming the BFSS software package has great potential to provide guidance for optimizing furnace operations.

Graduate Students Thesis

Chen, Y, 2012, "Numerical Simulation for a Blast Furnace", Masters Thesis, Purdue University Calumet

Award

Rahman, Md.T., Fu, D., Chen, Y., 2012, "Development and Application of Burden Distribution Model and Shaft Simulation Model for Blast Furnace", 1st place in AISTech 2012 Graduate Student Poster Competition, Atlanta, Georgia, USA.

6 CONCLUSIONS

In this project, a novel CFD model has been developed to optimize burden and gas distributions for minimizing fuel rate in blast furnaces. The novel CFD model includes major physical and chemical processes in the blast furnace such as gas-solid reductions, gas-liquid/solid heat exchange that includes the effects of reaction heat and phase changes, cohesive zone, and furnace permeability. The highlights of the development of the project are summarized below.

1. Burden distribution is a critical input for operation and simulation as well. A comprehensive burden distribution model has been developed to simulate the falling curve, stock profile, and a burden descending which is used to calculate the redistribution of the descending burden layer.
2. A methodology has been developed to determine the location and shape of the CZ, based on the burden temperature distribution and composition. In addition, an under-relaxation scheme has been developed to obtain layered CZ shape which explicitly considered the layer structure inside the CZ.
3. A coke rate sub-model has been implemented to the comprehensive 3-D BF shaft CFD model to iteratively determine the coke rate at fixed tuyere condition and given production rate.
4. The BFSS software package has been developed to integrate the BURDEN SIMULATOR, PRE-PROCESSOR and BLAST FURNACE SHAFT CFD SOLVER for simulation of blast furnace shaft process. Improvements have been made to the functionality and the ease of use of the graphic interface. The BFSS software package offers a powerful tool for the improvement of blast furnace performance.

Validations of the sub-models and the comprehensive model have been carried out. Validation of the comprehensive model was achieved by comparing CFD results with plant measurements.

CFD simulations for the shaft process of actual blast furnaces have been conducted. The CFD results show the influence of charging conditions on the shape and position of the CZ, which can affect gas utilization and fuel efficiency. The parametric study revealed that:

1. The CZ shape and location is determined by stock-line profile. The CZ shape is significantly affected by the burden composition, i.e., higher basicity results higher liquidus temperature, thus lowers the CZ shape.
2. The step-wise reduction procedure of the iron ore, i.e. $Fe_2O_3 \rightarrow Fe_3O_4 \rightarrow FeO \rightarrow Fe$, is evident in the blast furnace shaft.
3. Below the isotherm 600 °C and above 1200 °C, the gas composition is irrelevant to the burden temperature. The length of the TRZ is shortened in the region of low gas utilization. However, the gas composition held approximately the same relationship with the burden temperature between 600 °C and 1200 °C regardless of the radial location. One expectation is the region in the center of the center working furnace where the gas utilization is very low.

4. The gas distribution and utilization are compared for the center working furnace and wall working furnace. It has been found that in this particular condition, the gas utilization is about two percent higher in the wall working furnace. Therefore, the carbon consumption per unit hot metal will be lower. From the viewpoint of the CO_2 emission control, lower the carbon rate will be beneficial. It is also observed that the state of FeO-Fe-CO-CO_2 system is always in equilibrium in the two cases. The potential for further reducing the carbon rate may be still possible.
5. As the natural gas injection rate increase, the CZ location is higher and reduction of the iron oxides is accelerated.

NOMENCLATURE

SYMBOL	UNIT	DESCRIPTION
A	-	Coefficient for gas thermal conductivity
B	-	Coefficient for gas thermal conductivity
C	-	Coefficient for gas thermal conductivity
$C_{p,g}$	J/(kg.K)	Gas heat capacity
$C_{g,i}$	mol/m^3	Gas species concentration
$C_{b,i}$	mol/m^3	Burden species concentration
C_A	mol/m^3	Reactant gas concentration
C_B	mol/m^3	Product gas concentration
C_1	-	Constant in k-ε turbulence model
C_2	-	Constant in k-ε turbulence model
C_2	1/m	inertial resistance factor
C_μ	-	Constant in k-ε turbulence model
C_{CO}	mol/m^3	Concentrate of CO inside the pellet
$C_{\mathrm{CO_2}}$	mol/m^3	Concentrate of CO_2 inside the pellet
D	m	Chute receiving pipe diameter
D_0	m	Blast furnace throat diameter
D_{belly}	m	Blast furnace belly diameter
D^e_{CO}	m^2/s	Effectively diffusivity of CO
D_i	m^2/s	Molecular diffusivity
D_e	m^2/s	Effectively diffusivity of the product layer
$D_{eff,i}$	m^2/s	Effective diffusivity inside pellet
D'_e	cm^2/s	Effective diffusive coefficient of CO

D_{ij}	m^2/s	Molecular binary diffusivity
$D_{i,eff}$	m^2/s	Effective diffusivity in packed bed
d_p	m	Coke or ore particle diameter
d_{upper_layer}	m	Coke or ore particle diameter in upper layer
d_{lower_layer}	m	Coke or ore particle diameter in upper layer
e	-	Chute dimension
e	-	Porosity
g	m/s^2	Gravitational acceleration
G		Production term of the k-ε turbulence model
h	$W/(m^2.K)$	Heat transfer coefficient
h_0	m	Vertical distance from chute tip
h_b	J/kg	enthalpy of burden
h_g	J/kg	enthalpy of gas
$K_{e(r-s)}$	-	Equilibrium constant
$K_{\mathrm{p}i}$	-	Equilibrium constant
K_{g}	W/(m·K)	Thermal conductivity of the gas mixture
K_{gj}	W/(m·K)	Thermal conductivity of each gas component
l_β	m	Effective chute length
l_0	m	Total chute length
L	m	Vertical length
L_1	m	Vertical length
L_3	m	Vertical length
Lx	m	Radial distance
Ly	m	Radial distance

$\dot{m}$	kg/s-m^3	Gas mass increase
M_{mix}	g/mol	Gas molecular weight
M_i	g/mol	Gas molecular weight
M_j	g/mol	Gas molecular weight
Nu	-	Nusselt number
p	Pa	Gas pressure
Pr	-	Prandtl number
P_t	Pa	Total pressure
r	m	Horizontal path of a particle
r_0	m	pellet radius
r_0	cm	mean value of fine grain size
R	8.314 J/(K.mol)	Gas constant
R	-	Mixing factor
$R_{(r-s)}$	mol/(m^3.s)	Reaction rate
R_1	m	Radial distance
Re_p	-	Reynolds number
S_b	kg/(m^3.s)	Source term for burden velocity potential
$S_{b,h}$	J/(m^3.s)	Source term for burden enthalpy
$S_{b,c}$	mol/(m^3.s)	Source term for burden species
S_0	cm^2/cm^3	specific surface area
$S_{g,h}$	J/(m^3.s)	Source term for gas enthalpy
S_{M_j}	kg/(m^2.s^2)	Source term for gas momentum
$S_{g,c}$	mol/(m^3.s)	Source term for gas species
S_g	kg/(m^3.s)	Source term for gas continuity

S_{Mx}	kg/(m^2.s^2)	source term in gas x-momentum equation
S_{My}	kg/(m^2.s^2)	source term in gas y-momentum equation
S_{Mz}	kg/(m^2.s^2)	source term in gas z-momentum equation
Sc_i	-	Schmitt number
Sh_i	-	Sherwood number
t	s	dropping time
T	K	Gas temperature
T_s	K	Pellet temperature
u_b	m/s	Burden velocity in x-direction
u_g	m/s	Gas velocity in x-direction
U_j	m/s	Gas velocity in j direction
v	m/s	Gas velocity magnitude
v_1	m/s	Velocity of the particle
v_2	m/s	Velocity after impacting on chute
v_3	m/s	Velocity of the particle at the chute tip
v_4	m/s	Velocity of the particle at the chute tip
v_x	m/s	Velocity at chute tip in x-direction
v_y	m/s	Velocity at chute tip in y-direction
v_z	m/s	Velocity at chute tip in z- direction
$\bar{v}_i$	-	Diffusion volume
$\bar{v}_j$	-	Diffusion volume
v_0	mol/ (cm^3.s)	reduction rate
v_b	m/s	Burden velocity in y-direction
v_g	m/s	Gas velocity in y-direction

V_{charge}	m^3	Charging volume
w_b	m/s	Burden velocity in w-direction
w_g	m/s	Gas velocity in z-direction
X_0	-	Local un-reacted degree
a_p	-	Coefficient for variable at cell
a_E	-	Coefficient for variable at cell east
a_W	-	Coefficient for variable at cell west
a_N	-	Coefficient for variable at cell north
a_S	-	Coefficient for variable at cell south
a_B	-	Coefficient for variable at cell bottom
a_T	-	Coefficient for variable at cell top
b	-	Constant source term
α	deg.	Raw material angle of repose,14
α	deg.	Shaft angle from the vertical
α	-	Viscous loss coefficient
α	-	Shape factor of the concentrate
β	deg.	Complementary angle of Chute angle
β	deg.	Interior angles of the triangle on the impact
β	-	Micro-structure of the fine pellet
β_A	m^2/s	Gas film resistance
γ	-	Fracture factor
γ	-	Scaling factor
δ	m	Equivalent thickness of the reacted product
ε	m^2/s^3	Turbulent dissipation rate

ε	-	Porosity
k	-	Rolling coefficient
k	m^2/s^2	Turbulent kinetic energy
$k_{(r-s)}$	m^2/s	Chemical reaction resistance
k_i	cm/s	reaction constant
k_{eff}	W/m-K	Effective thermal conductivity
μ	-	Friction coefficient
μ	kg/(s·m)	Viscosity
μ_{eff}	kg/(s·m)	Gas effective viscosity
ρ_g	m^3/s	Gas density
ρ_b	m^3/s	Burden density
σ_k	-	Constant of the k-ε turbulence model
σ_ε	-	Constant of the k-ε turbulence model
τ	-	Labyrinth factor
ψ	- ,	Shape factor
ϕ_b	m^2/s	Burden potential
ω	rad/s	Angular velocity
Ω	-	Energy dispassion coefficient

REFERENCES

Akiyama, T., Takahashi, R. and Yagi, J., "Measurements of heat transfer coefficients between gas and particles for a single sphere and for moving beds", ISIJ Int, 1993, 33, pp. 703–710.

Austin, P.R., Nogami,H., and Yagi, J., “A Mathematical Model of Four Phase Motion and Heat Transfer in the Blast Furnace”, ISIJ Int., 1997, vol. 37, pp. 458–467.

Austin, P.R., Nogami,H., and Yagi, J., “Mathematical Model for Blast Furnace Reaction Analysis. Based on the Four Fluid Model”, ISIJ Int., 1996, vol. 37, pp. 748-755.

Agarwal, J. C., Brown, F C., Chin, D L., Frydenlun, A R., Jessiman, N S., Lingras A P., and Sikirica, S J., “The Role of Oxygen-plus-fuel Injection inIncreasing the Productivity of the Blast Furnace” Ironmaking Conference Proceedings , 1992, pp 139-147

Burke P. D. and J. M. Burgess, (1989), “A coupled gas and solid flow, heat transfer and chemical reaction rate model for the ironmaking blast furnace”, Proc. Ironmaking Conf., 48, 773-781.

Burke, P. D., Burgess, J. M., “A Coupled gas and solid flow heat transfer and chemical reaction rate model for the ironmaking blast furnace”, Ironmaking conference proceedings, 1989, 773.

Danloy, G., Mignon, J., Munnix, R., Dauwels, G., Bonte, L., “A Blast Furnace Model to Optimize the Burden Distribution” [C], 60th Ironmaking Conference Proceedings, 2001: 37.

de Castro, Jose Adilson, Hiroshi Nogami and Jun-ichiro Yagi, “Three-dimensional Multiphase Mathematical Modeling of the Blast Furnace Based on the Multifluid Model”, ISIJ International, Vol. 42 (2002), No. 1, pp. 44–52

Dong, X. F., Pinson, D., Zhang, S. J., Yu, A. B., and Zulli, P., 2003 “Gas-Powder Flow In Blast Furnace with Different Shapes of Cohesive Zone,” Third International Conference on CFD in the Minerals and Process Industries, Melbourne, Australia

Dong, X. F., Yu, A. B. Yagi,J. Zulli, P. “Modelling of multiphase flow in a blast furnace: recent developments and future work”, ISIJ Int. 2007 47 pp.1553-1570

Dong, X. F., Yu, A. B., Chew, SJ, Zulli, P., “Modeling of blast furnace with layered cohesive zone.” 2010, Metall Mater Trans B Proc Metall Mater Proc Sci 41:330–349

Donskoi, E., and McElwai, D.L.S, "Estimation and Modeling of Parameters for Direct Reduction in Iron Ore/Coal Composites: Part 1. Physical Parameters", Metallurgical and Materials Transactions B - Process Metallurgy and Materials Processing Science, 2003, 34B, pp. 93-102.

Fruehan, R. J. O. Fortini, H. W. Paxton, and R. Brindle, “Theoretical Minimum Energies to Produce Steel for selected Conditions”, March 2000, Carnegie Mellon University, Pittsburgh, PA, P III.

Fu, S., Zhang, L., Du, Y., “Investigation of gas-flow in the furnace shaft”, Iron and steel, 1981, 16.

Fuller, E. N., Schettler, P. D., and Giddings, J. C. "A new method for prediction of binary gas-phase diffusion coefficients", Ind. Eng. Chem., 1966, 58, 19–27.

Gu, M., Z. Chen, D. Huang, P. Chaubal and C.Q. Zhou, “Heat Transfer, Devolatilization and Combustion of Injected Coal before Entering Raceways”, presented at the AIST 2006, May 2006.

Hatano, M., and Kurita, K., "A mathematical model of blast furnace considering radial distribution of gas flow, heat transfer and reactions considered". ISIJ, 1982, vol. 22, pp. 448–456.

Hockings K. L., J. M. Burgess, J. Monaghan, L. Jelenich, P. Zulli and W. B. U. Tanzil, (1988), “Application of ”RABIT” burden distribution model to BHP blast furnaces”, Proc. Ironmaking Conf., 47, 289-296.

Huang F. Comprehensive Falling Curve Model. Internal technical communication, 2009, ArcelorMittal Global R&D-East Chicago.

Huang, D., Yang, X., Yang, X., Kong L. “Kinetics and mathematical model for reduction process of iron ore briquette containing carbon”, ACTA METALLURGICA SINICA (Chinese edition), 1996 32(6), pp. 629-636.

Huang, F. Comprehensive Falling Curve Model, “Internal technical communication”, 2009, ArcelorMittal Global R&D-East Chicago.

Huang, X., “Principle of steel and iron metallurgy, metallurgy industry Press”, 2008, Beijing. pp.239 , 275.

Ichida M., Nishihara K., Tamura K., Sugata M., Ono H., Influence of Ore/CokeDistribution on Descending and Melting Behavior of Burden in Blast Furnace [J]. ISIJ International, 1991, 3(5): 505.

Ichida M., Takao M., Kunitomo K., Matsuzaki S., Deno T., Influence of Ore/CokeDistribution on Descending and Melting Behavior of Burden in Blast Furnace [J]. ISIJ International, 1991, 3(5): 493.

Ichida, M., Takao, M., Kunitomo, K., Matsuzaktl, S., And Nishihara, K., “Radial Distribution of Burden Descent Velocity near Burden Surface in Blast Furnace”, ISIJ International, 1996, Vol. 36, No. 5, pp.493-502.

ISO 4695:2007 Iron ores for blast furnace feedstocks -- Determination of the reducibility by the rate of reduction index

Jiménez J., Mochón J., Ayala J. S. Mathematical Model of Gas Flow Distribution in a Scale Model of a Blast Furnace Shaft [J]. ISIJ International, 2004, 44(3): 518.

Jiménez J., Mochón J., Formoso A., et al. Burden Distribution Analysis by Digital Image Processing in a Scale Model of a Blast Furnace Shaft [J]. ISIJ International, 2000, 40(2): 114.

Jin, H. and Choi, S. "Numerical analysis of isothermal flow in lower part of blast furnace considering effect of cohesive zone", Ironmaking Steelmaking, 2010, 37, 89.

Kajiwara Y., Inada T., and Tanaka T., Two Dimensional Analysis on the Formation Process of Burden Distribution at Blast Furnace Top [J], Trans. ISIJ, 1988, 28: 916.

Kajiwara Y., T. Jimbo and T. Sakai, (1983), "Development of a simulation model for burden distribution at blast furnace top", Trans. Iron Steel Inst. Jpn., 23, 1045-52

Kajiwara, Y., T. Inada, T. Tanaka and T. Jimbo: Sumitorno Sea,'c/7, 44 (1990), December, 249.

Kondoh M., Okabe K., Kurihara J., Okumura K., Tomita S., ISIJ, 1977, 63(11): S446 (in Japanese)..

Kumar S. P., Ram K M., Mathematical Modeling of Burden Distribution in the Bell-less Top Blast Furnace [C], AISTech, 2006: 273.

Liang D., Yu Y. W., Bai C. G., et al. Effect of Burden Material Size on Blast Furnace Stockline Profile of Bell-Less Blast Furnace [J]. Ironmaking & Steelmaking, 2009, 36(3): 217.

Liu Y. C., Charging rules of blast furnace [M]. 2nd ed. Beijing: Metallurgical Industry Press, 2005 (in Chinese).

Liu, Y. C., "Charging rules of blast furnace" [M], 2nd ed. Beijing: Metallurgical Industry Press, 2005 (in Chinese).

Matsuzaki S., Estimation of Stack Profile of Burden at Peripheral Zone of Blast Furnace Top [J]. ISIJ International, 2003, 43(5): 620.

McCarthy M. J., P. L. Mayfield, P. Zulli, A. J. Rex and W. B. U. Tanzil, (1993), "Studies of the charging stream trajectories and burden distribution in the blast furnace", Proc. Ironmaking Conf., 52, 505-515.

Mills, Anthony F., "Mass Transfer", Prentice Hall, 2001, pp.87.

Nag S., and Korann V. M., Development of Material Trajectory Simulation Model for Blast Furnace Compact Bell-Less Top [J]. Ironmaking & Steelmaking, 2009, 36(5): 371.

Nan, S. "Ironmaing calculation", Metallurgy Industry Press, 2005, Beijing. (In Chinese) pp. 181

Narita, K., S. Inaba, M. Shimizu, AYamaguchi, I. Kobayashi and K. Okimoto: T,'ans. Iron Stee/ Insl. Jpn., 21 (1981), 405.

Narita, S. Inaba, I. Kobayashi, K. Okimoto, M. Shimizu, T. Yabata and S, Tamada:T,'ans. Iron Steel Inst. Jpn., 19 (1979), 667. Dfu: Falling curve, Burden distribution and O/C

Nikus, M., "A Set of Models for On-Line Estimation of Burden and Gas Distribution in the Blast Furnace", Ph.D. Thesis, 2001

Nishio N., Ariyama T., Analysis on Formation Processes of Burden Distribution in Blast Furnace [J]. ISIJ, 1982, 68(15): 2330 (in Japanese).

Ohno, J., H. Yashiro, Y. Shirakawa, A. Tsuda, S. Watanabe, T. Hirata, M. Higuchi and M. Nakagome, (1986), "Microwave burden sensor for blast furnaces", IFACConf. on Automation in Mining, Mineral and Metal Processing, Tokyo, Japan, 353-358.

Omori, Y., "Blast Furnace Phenomena and Modeling", Elsevier Applied Science, London, 1987.

Osborn, E. F., Devries, R. C., Gee, K. H., and Kraner, H. M.: Journal of Metals, January 1954, pp. 33-45.

Park J., Baek U., Jang K., Oh H., Han J., Development of the Burden Distribution and Gas Flow Model in the Blast Furnace Shaft [J]. ISIJ International, 2011, 51 (10):1617

Park, J., Baek, U., Jang, K., Oh H., Han J., "Development of the Burden Distribution and Gas Flow Model in the Blast Furnace Shaft" [J], ISIJ International, 2011, 51 (10):1617

Patankar, S. V., "Numerical Heat Transfer and Fluid Flow," Hemisphere, Washington, D, 1980.

Poos A., G. Danloy and R. Franssen, (1981), "The Spiroterm system for the gas distribution control on blast furnaces", Proc. Ironmaking Conf., 40, 98-104.

Poveromo, J.J. and J. W. Hlinka: Proc. of 3rd Process Technology Conf. Pittsburgh, (1982), 166.

Rosner, D., "Transport Processes in Chemically Reacting Flow Systems", Butterworth and Co., Boston MA, 1986, pp. 113-16.

Sahajwalla, V., S.K. Gupta, Y. Al-Omari, N. Saha-Chaudhury, F. Rorick, G. Hegedus, P. Chaubal, J. Burgo, M. Best and F. Hyle, "Combustion Characteristics of Pulverized Coals and Char Released in Blast Furnace Off-Gas", ISSTech 2003 Conference Proceedings, pp775-785, 2003.

Sawa Y., Takeda, K., Taguchi S., Mathematical modeling of blast furnace characterized by the precise layer structure in stock column [C]. Ironmaking Confernce Proceeding,1991: 417

Sawa, Y., Takeda, K., Taguchi, S., Mathematical modeling of blast furnace characterized by the precise layer structure in stock column [C]. Ironmaking Confernce Proceeding, 1991: 417.

Strassburger, J.H. (Ed.), "Blast Furnace Theory and Practice", Gordon and Breach Science Publishers 1969, Vol. 2.

Strassburger, J.H. (Ed.), "Blast Furnace Theory and Practice", Gordon and Breach Science Publishers, 1969, Vol. 2, pp. 874, pp. 696.

Stubbles, J., "Energy Use in the U.S. Steel Industry: An Historical Perspective and Future Opportunities", report to U.S. Department of Energy, September 2000

Schmole, P., and Lindenberg, H., "Hot metal production in the blast furnace - potentials to reduce CO2 emissions", 2004, presented at the 1st Chinese-German Seminar.

Song, J. "Blast furnace ironmaking, theory and practice", Metallurgy industry press, 2005, Beijing, pp. 30

Takatani, K., T. Inada and Y. Ujisawa: ISIJ Int. 39 (1999), 15.

Tanzil W. B. U., D. G. Mellor and J. M. Burgess, (1990), "Application of a two dimensional flow, heat transfer and chemical reaction model for process guidance and gas distribution control on Port Kembla no. 5 blast furnace", Proc. Sixth international iron and steel congress, 6, 355-363.

Valipour , M.S. and Saboohi, Y., "Modeling of multiple noncatalytic gas–solid reactions in a moving bed of porous pellets based on finite volume method", Heat and Mass Transfer, 2007, 43 (9), pp. 881–894.

Valipour, M.S. and Saboohi, Y., "Modeling of Multiple Noncatalytic Gas-Solid. Reactions in a Moving Bed of Porous Pellets Based on Finite Volume Method", Heat and Mass Transfer, 43, 881-894, 2007.

Versteeg, H.K. and Malalasekera, W., "An Introduction to Computational Fluid Dynamics", Prentice Hall, 1995.

Wang P., Mathematical Imitation of Trajectory of Burden Flow for Bellless Top BF [J]. Journal of Iron and Steel Research, International, 2006, 18(5): 5 (in Chinese).

Wang P., Measurement and Analysis of Burden Flow Trajectory and Width in Bell-Less Top with Two Concentric Vertical Hoppers [J]. Iron and Steel, 2003, 38(3): 8 (in Chinese).

Wright B., Zulli P., Zhou Z.Y., Yu A.B., "Gas–solid flow in an ironmaking blast furnace. Part I: experimental studies" [J], Powder Technology, 2011, 208:86.

Xie, Y. and Qin, M., "A mathematical model for reduction of iron ore in moving bed", Acta Metallurgica Sinica, Series B, 1984, vol. 20, pp. 249-260.

Yan., F., Zhou, C.Q. Huang, D. Chaubal, P. and Zhao, Y. "3-D Computational Modeling of a Blast Furnace Hearth", Iron and Steel technology, Vol. 2, No.1, pp. 48-58, 2005

Yang K., Choi S., Chung J., Yagi J., Numerical Modeling of Reaction and Flow Characteristics in a Blast Furnace with Consideration of Layered Burden [J]. ISIJ International, 2010 (7), 50:972

Yang, K., Choi, S., Chung, J., Yagi, J., "Numerical Modeling of Reaction and Flow Characteristics in a Blast Furnace with Consideration of Layered Burden" [J], ISIJ International, 2010 (7), 50:972

Yu Y. W., Bai C. G., Zhang Z. R., et al. Theoretical Calculation and Validation of Burden Trajectory in Bell-Less Top Blast Furnace [J]. Ironmaking & Steelmaking, 2009, 36(7): 505.

Yuji, I., Kouji, T., "Mathematical Model Analysis for Oxidation of Coke at High Temperature", ISIJ International, 1989, Vol. 29, No, l, pp 43 48.

Zaimi, S. A., Akiyama T., Guillot J. B., Yagi J., Validation of ablast furnace solid flow model using reliable 3-D experimental results [J]. ISIJ International, 2000, 40 (4): 332.

Zhang, S. J., Yu A. B., Zull P., Wright B., Austin P., Numerical Simulation of Solid Flow in a Blast Furnace [C], Second International Conference on CFD in the Minerals and Process Industries, 1999: 411.

Zhang, S.J., Yu, A.B., Zulli, P., Wright, B. and Austin, P., Numerical simulation of solids flow in a blast furnace [J], Applied Mathematical Modelling,2002, 26: 141.

Zhao, Y., "Using Neural Network Technology for Blast Furnace Slag Viscosity and Liquidus Temperature Calculation", AISTech 2004.

Zhao, Y., Capo, J.C., McKnight, S.J., D'Alessio, J., Ferron, K.J., Badgley, P.F., Gao, Z. and Gao, T., " Development of Burden Distribution Technology at. U. S. Steel Canada's Hamilton Works 'E' Blast Furnace. ", AISTech 2010

Zhou, C.Q., D. (Frank) Huang, Zumao Chen, Naresh K Selvarasu, Mingyan Gu, Yongfu Zhao, and Pinakin Chaubal, "Simulations of Raceway Conditions in A Blast Furnace", Submitted to the 4th International Congress on the Science and technology of Ironmaking", Japan, November, 2006

List of publications related to this research

Fu, D., Wu, B., Moreland, J., Chen, G., Ren S., and Zhou, C. Q., 2009, “Virtual Reality Visualization of Typical Processes in Blast Furnace”, 2009 AISTech - Iron and Steel Technology Conference Proceedings, St. Louis, Mo., USA, Vol. 1, pp. 307-314.

Fu, D., Tian, F., Sotiroglou, K., and Zhou, C. Q., 2009, “The Numerical Analysis of Flow Behavior Inside the Blast Furnace”, Proceedings of 2009 ASME Summer Heat Transfer Conference, San Francisco, California, USA, HT2009-88254.

Fu, D., Huang, F., Tian, F., Zhou C. Q., 2010, “Burden Descending and Redistribution in a Blast Furnace”, AIST2010, Pittsburgh, PA, USA, Vol. 1, pp. 693-700.

Zhou, C. Q., 2011 “State-of-the-Art Blast Furnace Model for CO2 Reduction”, Proceedings of Cleantech 2011, Budapest, Hungary.

Fu, D., Zhou, C. Q., Zhao, Y., D'Alessio, J., Ferron, K. J., 2011, "Numerical Simulation of Blast Furnace Shaft Process", METEC InSteelCon2011 STEELSIM2011, Dusseldorf, Germany.

Vehec, J., and Zhou, C. Q., 2011, "State-of-the-Art Blast Furnace Model for Minimization of Fuel Rates," METEC InSteelCon2011 STEELSIM2011, Dusseldorf, Germany.

Fu, D., Chen, Y., Rahman, M. T., Zhou, C. Q., D'Alessio, J., Ferron, K. J., and Zhao, Y. F., 2011, "Prediction of the Cohesive Zone in a Blast Furnace,", Indianapolis, IN.

Fu, D., Wu, B., Chen, G., Moreland, J., Tian, F., Hu, Y., and Zhou, C. Q., 2009 "Virtual Reality Visualization of CFD Simulation For Iron/ Steelmaking Processes", Proceedings of ASME 2010 International Heat Transfer Conference, Washington D.C., USA, ASME IHTC2010-23180, pp. 761-768, Paper no. IHTC14-23180, doi:10.1115/IHTC14-23180

Fu, D., Chen, Y., Rahman, Md.T., Zhao, Y., D'Alessio, J., Ferron, K. J., and Zhou, C. Q., 2012, “Validation of the numerical model for blast furnace shaft process”, Atlanta, Georgia, USA.